PHOTOPHYSICS OF TRANSITION METAL DICHALCOGENIDES OBTAINED FROM LIQUID PHASE EXFOLIATION

Víctor Vega Mayoral

Doctoral Dissertation
Jožef Stefan International Postgraduate School
Ljubljana, Slovenia

Supervisor: Prof. Dr. Christoph Gadermaier, Complex Matter Department, Jožef Stefan Institute, Ljubljana, Slovenia

Evaluation Board:
Prof. Dr. Maja Remškar, Chair, Condensed Matter Physics Department, Jožef Stefan Institute, Ljubljana, Slovenia
Asst. Prof. Dr. Tomaž Mertelj, Member, Complex Matter Department, Jožef Stefan Institute, Ljubljana, Slovenia
Prof. Dr Jonathan Nesbit Coleman, Member, School of Physics, Trinity College Dublin, Dublin, Ireland

MEDNARODNA PODIPLOMSKA ŠOLA JOŽEFA STEFANA
JOŽEF STEFAN INTERNATIONAL POSTGRADUATE SCHOOL



Víctor Vega Mayoral

PHOTOPHYSICS OF TRANSITION METAL DICHALCOGENIDES OBTAINED FROM LIQUID PHASE EXFOLIATION

Doctoral Dissertation

FOTOFIZIKA DIHALKOGENIDOV PREHODNIH KOVIN PRIDOBLJENIH PREKO EKSFOLIACIJE V TEKOČI FAZI

Doktorska disertacija

Supervisor: Prof. Dr. Christoph Gadermaier

Ljubljana, Slovenia, October 2016

Per aspera ad astra

Acknowledgements

This work would not have been possible if nobody had given me a chance. I would like to start by thanking my supervisor professor Christoph Gadermaier. He gave me the opportunity to start my career in science in an amazing field. After that starting point he supported and guided me. When I arrived to Slovenia I met a working team that welcomed me with open arms. I thank my colleagues Tetiana Borzda, Peter Topolovsek and Matej Prijatelj. I would like to thank my friend Daniele Vella for all the things we learned together. I am grateful to Jure Strle, who helped me with the revision of the manuscript. I would like to thank everyone in the Department for Complex Matter, for three years of efforts and results.

I would like to thank the European Commission for financial support via the Marie Curie program (Initial training project MoWSeS). I want to acknowledge the public education system of Spain that gave me the tools and knowledge to start my career in science.

For some time I was lost. In Ireland I found myself again and I rediscovered why science research is so addictive. I would like to thank professor Jonathan N. Coleman, his group and Dr. Claudia Backes for their dedication and further collaboration. During three months I was surrounded by amazing people that accepted me as if I were one of them.

Thanks to Matthias Marx. Because he hosted me as a friend.

I thank professor Giulio Cerullo. He opened me the doors of his lab each time I needed it. Iacopo Tempra and Eva A. A. Pogna helped me during Milano's sweltering summers.

I express my deepest gratitude to my family, my mother Paula, because even in the distance we managed to feel close to each other, my brother Marco made me feel as if 2000 km were nothing, and he made some cool pictures for me. My deepest gratitude to Enar, because she walked the full path beside me.

Finally, I would like to thank to the members of the evaluation board. Their comments and corrections helped me to improve the scientific quality of this thesis.

A todos vosotros gracias. ¡Muchas gracias!

Abstract

This thesis is dedicated to the study of semiconducting bidimensional transition metal dichalcogenides (TMDCs). Two research lines are presented in this document. The first one is focused on exfoliating WS_2 via liquid phase exfoliation and the use of some basic, commonly available and fast characterization techniques. The second research line focuses on a deeper characterization of the photoexcited states dynamics of few-layer MoS_2 and WS_2 where we have used spectrally-resolved femtosecond pump–probe spectroscopy.

Exfoliation in water/polymer dispersions has been studied. Poly(vynil alcohol) (PVA) is proposed as a model polymeric stabilizer. Effects of polymer concentration and centrifugation size-selection protocol on concentration, thickness and lateral size are reported. Extinction, Raman and photoluminescence spectroscopy were used for a fast and semiquantitative characterization supported by the more conventional TEM and AFM microscopy. All dispersed flakes contribute to the Raman signal, while just monolayers contribute to photoluminescence (PL). Therefore the PL/Raman spectrum is proposed as a way to track the monolayer content in the sample.

The spectrum of emitted light broadens as the WS_2/PVA/Water dispersion dryes, suggesting a different doping level between flakes in dispersion and in dry state. Two WS_2–PVA composites were produced that exhibit different optical properties and that can be used for different applications. As example, composite prepared at 50 ºC revealing low scattering would be available for optical applications as saturable absorber, while in the composite produced by freeze light emission is preserved.

Photoexcited states dynamics in few-layer WS_2 have beeen studied using femtosecond pump-probe spectroscopy. Using a cascade model I obtained an exciton dissociation lifetime of 1.3 ps. After excitons dissociation the geminated charges diffuse till they are trapped in defects such as grain boundaries or sulphur vacancies. There is a longer relaxation process that lasts hundreds of picoseconds assigned to charge recombination.

Povzetek

Pričujoče doktorsko delo je posvečeno študiji polprevodnih dvodimenzionalnih dihalkogenidov prehodnih kovin (*ang.* transition metal dichalcogenides – TMDC). V disertaciji sta predstavljeni dve veji raziskovanja. Pri prvi smo se osredotočili na eksfoliacijo WS_2 iz tekoče faze in uporabo nekaterih osnovnih, razširjenih in hitrih spektroskopskih tehnik karakterizacije. Pri drugi veji pa smo podrobneje karakterizirali dinamiko fotovzbujenih stanj nekajplastnih MoS_2 in WS_2. Pri eksfoliaciji TMDC v vodnih/polimernih disperzijah smo kot polimerni stabilizator uporabili polivinil alkohol (*ang.* poly(vynil alchohol) – PVA).

Poročamo o vplivih koncentracije polimera in centrifugacije na koncentracijo, debelino in prečno velikost lusk TMDC. Kot hitro in semi-kvantitativno karakterizacijo smo uporabili ekstincijsko, Ramanovo in fotoluminiscenčno (*ang.* photoluminescence – PL) spektroskopijo, ki so bile podprte s konvencionalnejšima tehnikama, presevno elektronsko mikroskopijo (*ang.* transmission electron microscopy – TEM) in mikroskopijo na atomsko silo (*ang.* atomic force microscopy – AFM). Ker vse dispergirane luske prispevajo k Ramanovem signalu, k fotoluminiscenčnemu signalu pa zgolj monoplastne, smo kombinirane PL/Ramanove spektre uporabili kot preprost način za beleženje vsebnosti monoplastnih lusk v vzorcu.

Pri posušenih luskah se spekter izsevane svetlobe razširi, kar nakazuje na razliko v dopiranju med dispergiranim in suhim stanjem. Pripravili smo dva kompozita WS_2-PVA, ki kažeta različne optične lastnosti in ju lahko uporabimo za različne optične aplikacije. Eden od njiju ima pri 50 °C nizko sipanje in bi ga lahko uporabili kot saturacijski absorber, drugega pa smo naredili s sušenjem z zamrzovanjem (liofilizacijo), pri čemer se ohrani izvorna emisija.

Dinamiko fotovzbujenih stanj v nekajplastnem WS_2 smo preiskovali s spektralno ločljivo femtosekundno izbujevalno-testno (*ang.* pump-probe) spektroskopijo. Z uporabo kaskadnega modela smo izmerili razpadni čas ekscitona 1,3 ps. Po razpadu ekscitonov oba naboja difundirata, dokler se ne ujameta v defekte, kot so meje med zrni ali manjkajoči atomi žvepla. Pri tem opazimo več sto pikosekund dolg relaksacijski proces, ki bi ga lahko pripisali rekombinaciji naboja.

Contents

List of Figures **xv**

List of Tables **xvii**

Abbreviations **xix**

1 Introduction **1**
1.1 Brief History of Nanomaterials . . . 1
1.2 Transition Metal Dichalcogenides . . . 2
1.2.1 Crystalline structure and electronic properties . . . 3
1.2.2 Raman scattering in TMDCs . . . 5
1.2.3 Exfoliation and growth of TMDCs . . . 6
1.2.4 Electronics of TMDCs . . . 8
1.2.5 TMDCs spintronics and valleytronics . . . 9
1.2.6 Bound particles in TMDCs . . . 10
1.2.7 TMDCs and nonlinear optical properties . . . 14
1.2.8 Photoexcited states dynamics . . . 15

2 Methods **21**
2.1 Fluorescence, Absorption, Extinction and Raman Spectroscopy . . . 21
2.1.1 Absorption and extinction . . . 21
2.1.2 Photoluminescence . . . 24
2.1.3 Raman spectroscopy . . . 25
2.2 Femtosecond Pump-Probe Spectroscopy, Because Time Matters . . . 26
2.2.1 Introduction . . . 27
2.2.2 Ultrashort pulses . . . 27
2.2.3 Nonlinear optics . . . 29
2.2.4 Pump-probe time-resolved spectroscopy . . . 33
2.2.5 Experimental setup . . . 35
2.3 Liquid Phase Exfoliation . . . 36
2.3.1 Stabilization . . . 37
2.3.2 Exfoliation . . . 42
2.3.3 Flake selection via centrifugation . . . 45

3 Exfoliation of WS_2 in PVA/Water Dispersion **49**
3.1 Exfoliation in PVA/Water Dispersion and WS_2/PVA Composite Formation 49
3.1.1 Introduction . . . 49
3.1.2 Results and discussion . . . 51
3.1.2.1 Polymer-stabilized nanosheets: microscopy . . . 51
3.1.2.2 Optimization of the polymer concentration . . . 54
3.1.2.3 Optimization of the postexfoliation centrifugation. . . . 58
3.1.2.4 Optical properties of WS_2 during drying . . . 60

3.1.2.5 Production of luminescent WS_2–PVA composites 64
3.1.3 Conclusion 66

4 Photoinduced Dynamics in Transition Metal Dichalcogenides 69
4.1 Ultrafast Dynamics in Non-Size-Selected WS_2 69
4.1.1 Introduction 69
4.1.2 Results and discussion 70
4.1.3 Conclusions 76

5 Conclusions and Outlook 79

Appendix A Preliminary Work on Stabilization of WS_2 in Polymer/Solvent Dispersion 81

Appendix B Suplementary Information for Exfoliation of WS_2 in PVA/Water Dispersion 85
B.1 Extinction Coefficient of WS_2 85
B.2 Fitted PL Spectra of LPE WS_2-PVA on Drying 87
B.3 Effect of PVA on Optical Properties of CVD-WS_2 88
B.4 As Recorded Raman Spectra of WS_2-PVA Composites 90

References 91

Bibliography 107

Biography 111

Index 113

List of Figures

Figure 1.1: Damascus steel blade. 1
Figure 1.2: Microscope glass slide from Faraday's lectures. 2
Figure 1.3: Layer stacking and crystalline polytipes. 3
Figure 1.4: Thickness dependent MoS_2 energy band structure. 4
Figure 1.5: 2H-TMDCs Raman modes 5
Figure 1.6: MoS_2 CVD growth. 7
Figure 1.7: Graphical visualization of Moore's law. 8
Figure 1.8: Spin-valley polarization. 9
Figure 1.9: Excitons in TMDCs. 11
Figure 1.10: Photoluminescence enhancement in monolayer MoS_2. 12
Figure 1.11: Excitonic and trion transition shift with doping. 13
Figure 1.12: Z-scan measurements. 14
Figure 1.13: Second harmonic generation in MoS_2 15
Figure 1.14: Thermalization and cooling ultrafastphotoexcited states dynamics in MoS_2. 16
Figure 1.15: Ultrafast charges diffusion measurements. 17
Figure 1.16: Trapping via Auger scattering. 17
Figure 1.17: WS_2 bandgap renormalization. 18

Figure 2.1: Semiconductor density of states for 3D, 2D and 1D scenario. 22
Figure 2.2: Van Hove singularities. 23
Figure 2.3: Fluorescence and phosphorescence schematic representation. 25
Figure 2.4: Elastic and inelastic scattering. 26
Figure 2.5: Locked phase light emission. 28
Figure 2.6: SHG coherence lenght 31
Figure 2.7: Pump and probe pulses arriving to the sample 34
Figure 2.8: Origin of the pump-probe signal. 35
Figure 2.9: Schematic representation of our pump-probe setup. 36
Figure 2.10: Helmholtz, Gouy-Chapman and Stern potential model. 39
Figure 2.11: Representation of the steric stabilization on an entropy-enthalpy diagram. 40
Figure 2.12: Dispersion stability as a function of the polymer concentration. 42
Figure 2.13: Liquid phase exfoliation. 44
Figure 2.14: oblate 45
Figure 2.15: <N> vs <L>. 46

Figure 3.1: QR code to exfoliation article. 49
Figure 3.2: Extinction and Raman spectrum of LPE WS_2 51
Figure 3.3: Determination of layer thickness 52
Figure 3.4: Statistical microscopic analysis of PVA-stabilized WS_2 nanosheets . . . 53
Figure 3.5: Effect of PVA concentration, Raman and extinction spectrum. 54

Figure 3.6: Effect of PVA concentration on WS_2 concentration. 55
Figure 3.7: Effect of PVA concentration on <L> and <N>. 56
Figure 3.8: Qualitative monolayer volume fraction and monolayer concentration. . 57
Figure 3.9: Effect of centrifugation parameters on WS_2 <N>, <L> and monolayer V_f. 58
Figure 3.10: Effect of centrifugation parameters on <L> and $I_{PL}I_{Raman}$<N>. 59
Figure 3.11: Spectral shape evolution during drying. 60
Figure 3.12: Exciton and trion energy during drying. 61
Figure 3.13: Height, width and area of emitted light during drying. 62
Figure 3.14: A_{trion}/AExciton 63
Figure 3.15: WS_2-PVA composites 64
Figure 3.16: Reversibility of composite formation. 65
Figure 3.17: Photographs of composite before and after redispersion. 66

Figure 4.1: QR code to WS_2 pump-probe article 69
Figure 4.2: Extinction spectrum of few-layer WS_2. 71
Figure 4.3: WS_2 $\Delta T/T$ experimental data. 72
Figure 4.4: Photoexcited states dynamics. 73
Figure 4.5: Comparison of real data with the cascade model. 74
Figure 4.6: Spectral contribution of each cascade level. 75
Figure 4.7: Evolution of the populations. 76

Figure A.1: Extinction spectra of transferred WS_2 nanosheets. 82
Figure A.2: Normalized PL of the different samples with respect to their absorption at the excitation wavelength (435 nm). 83
Figure A.3: Fitted PL spectra for different samples. 84

Figure B.1: WS_2 extinction coefficient. 85
Figure B.2: PL of LPE WS_2-PVA during drying. 87
Figure B.3: Optical micrographs of CVD-WS_2 88
Figure B.4: Raman/PL spectra of CVD-WS_2 before and after the deposition of PVA on the surface. 88
Figure B.5: Raman/PL spectra of CVD-WS_2 before and after the deposition of PVA on the surface. 89
Figure B.6: Raman/PL spectra of CVD-WS_2 before and after the deposition of PVA on the surface. 90

List of Tables

Table 1.1: Near band-gap optical transitions including the excitonic effect [27]. . . 4

Table A.1: Fitted parameters for each sample. 83

Table B.1: Tabulated data of the fit components of Fig. B.5 showing energy (E), width (w) and area (A) of the exciton and trion, respectively, as well as the trion/exciton ratios. 89

Abbreviations

3D ... Tri-dimeensional
2D ... Bi-dimensional
1D ... Uni-dimensional
0D ... Zero-dimensional
AFM ... Atomic force microscopy
AOM ... Acusto optic modulator
BP ... Black phosphorous
CB ... Conduction band
CPA ... Chirp pulse amplification
CVD ... Chemical vapour deposition
CW ... Continuous wave
DOS ... Density of states
IPA ... Isopropyl alcohol or isopropanol
LPE ... Liquid phase exfoliation
NMP ... N-Methyl-2-pyrrolidone)
PA ... Photoinduced absorption
PB ... Photobleaching
PL ... Photoluminescence
PMMA ... Poly(methyl methacrylate)
PS ... Polystyrene
PVA ... Poly(vynil alcohol)
RSA ... Reverse saturable absorption
SA ... Saturable absorber
SC ... Sodium cholate
SHG ... Second harmonic generation
SPM ... Self-phase modulation
SUC ... Super-continuum
TEM ... Transmission electron microscopy
THF ... Tetrahydrofuran
Ti:sapphire ... titanium sapphire
TMDCs ... Transition metal dichalcogenides
TMOs ... Transition metal oxides
TPA ... Two–photon absorption
Tx100 ... Triton X-100
VB ... Valence band

Chapter 1

Introduction

In this Chapter I will summarize the history, opto-electronic properties, some applications and production techniques of nanomaterials.

1.1 Brief History of Nanomaterials

Nanomaterial science is a field of science focused on materials with at least one of their dimensions in the nanometric scale. These materials can be grouped as 0D, 1D or 2D determined by how many of their dimensions (3, 2 or 1, respectively) have nanometric size. At this scale there are main changes in materials' physicochemical properties like surface plasmon resonances in metal particles or quantum confinement effects in semiconductors.

It is hard to determine the birth date of nanotechnology. It is known that as early as ninth century, in the old Mesopotamia, craftsmen used nanoparticles to generate a glittering effect on their pottery [1]. In the middle ages there was strong empirical knowledge on how to treat some metals to generate luster in pots.



Figure 1.1: Damascus steel blade [2].

When the Crusaders arrived to the Middle east, to kill in the name of their religion, they found that certain Muslim warriors brandished extremely flexible, hard and sharp swords. These blades were known as Damascus swords (made of Damascus steel). Damascus steel was recognisable because of a particular patterned structure in the blade (Fig. 1.1). Recent studies link the exceptional mechanical properties of the blade to a reinforcement of the iron with nanowires and carbon nanotubes [3].



Figure 1.2: Microscope glass slide used by Faraday at his lectures. This glass slide is preserved in the Whipple Museum of the History of Science in Cambridge [6].

In the XIXth century Faraday discovered that if the size of gold particles is small enough, they abandon their metallic behaviour. They stop reflecting the light and they aquire a color that is characteristic of their size (Fig. 1.2). Even though he did not have the tools to understand the process, it is considered the first scientific approach to nanotechnology [4].

Richard Feynman's speech "There's Plenty of Room at the Bottom", given at an American Physical Society meeting in December 1959 [5], is considered by many authors as the starting point of the nanotechnology field as we understand it nowadays. Feynman listed possible future applications such as new and better microscopes, higher computation power and others that were developed afterwards. This speech remained largely unnoticed for decades but nowadays it is well known.

First scientific publications about nanomaterials were about the crystalline structure of 2D material such as CdI_2 [7] and MoS_2 [8]. They were followed by the theoretical prediction of unidimensional structures [9], their observation [10] and their synthesis [11], [12]. 0D structures arrived in the 1980s with the discovery of the fullerene [13].

As we can see, even when it sometimes looks like graphene is the king of nanomaterials [14], humanity has studied and used nanomaterials for centuries. Nowadays the palette of available 2D materials is only increasing further. Application fields are also constantly rising and feeding the research interest.

1.2 Transition Metal Dichalcogenides

Transition metal dichalcogenides (TMDCs) are a family of materials composed by two elements with MX_2 stoichiometry, where M is a transition metal (groups IV, V and VI of periodic table) and X is a chalcogen (sulphur, selenium or tellurium). Inside this family of materials we can find metals, semimetals, superconductors and semiconductors [15], [16].

TMDCs have been known for a long time. They were confused with lead compounds until the 1770s, when Carl W. Scheele identified molybdenum and tungsten as unique chemical elements.

During my PhD work I focused on semiconductor TMDCs (molybdenum and tungsten combined with sulphur, selenium or tellurium), particularly WS_2 and MoS_2. From this point on I will use TMDCs to refer to the particular case of semiconductor TMDCs.

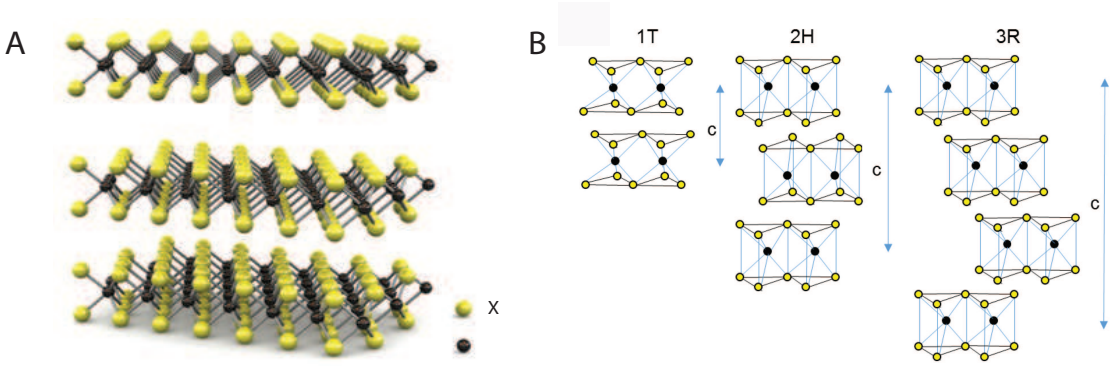


Figure 1.3: (A) Representation of layer stacking in few-layer TMDCs. (B)1T, 2H and 3R crystalline polytype of TMDCs [19], [20].

1.2.1 Crystalline structure and electronic properties

The crystalline structure of MoS_2 was first determined by Dickinson and Pauling [8]. MoS_2 crystalline structure is similar for all TMDCs. TMDCs can be found organized in three different crystalline structure polytypes (Fig. 1.3), 2H, 3R and 1T. The three of them have the same basic structure, a layer of hexagonally arranged molybdenum atoms is sandwiched between two hexagonal sulphur layers. 2H and 3R have trigonal prismatic coordination (D_{3h}) where each molybdenum atom is covalently bound to six sulphur atoms. 2H and 3R can be differenced in the layer stacking. 2H has two layers in the unit cell in hexagonal symmetry while 3R has three layers per unit cell in rhombohedral symmetry. 2H and 3R converge to the same crystal structure when they are thinned down to the monolayer regime, typically recognised as 2H. In the 1T polytype each Mo atom is also covalently bound to six sulphur atoms but with octahedral coordination and one layer per unit cell. 2H and 3R crystals of TMDCs are semiconducting and 1T is metallic. 2H is a more stable phase than 3R which tends to transform to the 2H polytype with time or upon heating [17]. The 1T phase is metastable. 1T phase cannot be found naturally and appears when MoS_2 is intercalated with Lithium [18]. In the following, unless something else is specified, whenever I talk about MoS_2, I will be refering to 2H-MoS_2 polytype.

TMDCs have strong covalent S-Mo-S bonds (intralayer) versus the weaker Van der Waals interlayer bounds between the layers. This is the reason for the ease of their exfoliation.

Knowing the exact crystal structure of MoS_2 is important to understand some of its properties. Bulk MoS_2 is in the D_{6h} symmetry group, while monolayer and all odd-layers are in the D_{3h} group. D_{6h} has inversion symmetry, but D_{3h} lacks it. As we will see in Chapter 2, in order to have second-order non-linear effects an asymmetric term (x^3) must appear in the electron's potential. If our material is perfectly symmetric, this term is negligible and hence it will not exhibit second-order non-linear optical effects. The material's second-order susceptibility ($\chi^{(2)}$) is seven times smaller in trilayer than in monolayer. $\chi^{(2)}$ is two orders of magnitude lower in even-layered flakes than in monolayer [21]). This is the reason why efficient second harmonic generation has been reported only in samples with odd layer numbers [22], [23].

MoS_2 electronic band structure has been studied since the 70's [24], [25]. All semi-

Table 1.1: Near band-gap optical transitions including the excitonic effect [27].

		Transition energy (eV)		
Structures	Transitions	Calculated	With exciton	Experiment
monolayer	K_{v1} to K_c	2.759	1.862	1.90
	K_{v2} to K_c	2.905	2.008	2.05
bilayer	Γ_v to K_c	1.888	1.341	1.6
	K_{v1} to K_c	2.427	2.003	1.88
	K_{v2} to K_c	2.601	2.177	2.05

conducting TMDCs have a similar energy band structure (Fig. 1.4). Bulk TMDCs have an indirect band gap. The maximum of valence band (VB) energy is at the Γ point. The minimum of the conduction band (CB) is placed between the Γ and K points. There is a local CB minimum and VB maximum at the K point. In the monolayer they become the absolute extreme and form a direct gap, in contrast to the indirect gap of bilayers and thicker crystals. The first explanation of this behaviour was that the local minimum placed in the K point originates in molybdenum d-orbitals and hence it is quite insensitive to a thickness variation. On the other hand, the states close to the indirect bandgap originate from the hybridisation of p_z-orbitals of sulphur. This hybridisation does not just originate from sulphurs of the same layer, but also has some contributions from sulphur atoms of different layers. Then, the indirect bandgap close to Γ is quite sensitive to changes of thickness. As MoS_2 is thinned, the bandgap at Γ expands more than the local bandgap at K [26]. At the transition between bilayer and monolayer the global Bandgap shifts from Γ to K and it changes from indirect to direct. This explanation roughly describes the main spectral features of MoS_2 and it was accepted by the research community, but it has some shadows. It does not take into account the binding energy of excitons (bound electron-hole pairs). The transition energy between the ground state and the exciton, called the optical gap, is lower than the electronic gap by the amount of the exciton binding energy. According to the calculations of Cheiwchanchamnangij and Lambrecht [27], where the exciton binding energy was taken into account, the bandgap at K point expands more than what it was initially thought (Table 1.1), but the binding energy of the exciton increases, which compensates the expansion and provokes the indirect-direct change of the optical gap. That would explain why the excitonic PL almost does not shift with the layer number [28], [29] and is supported with the extraordinary big exciton binding energy [30], and its increment as the material is thinned [31], [32].

The splitting in the maximum of the VB in the K point is assigned to the spin-orbit

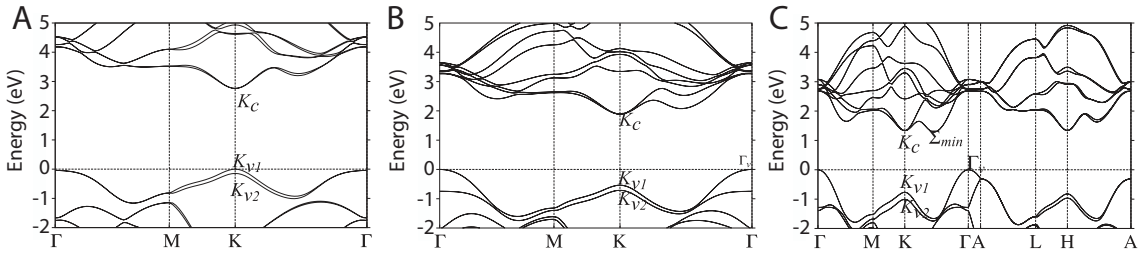


Figure 1.4: Energy band structure of MoS_2 monolayer (A), bilayer (B) and Bulk (C).

coupling in the monolayer, interlayer interaction has a certain effect on the splitting in bilayer and bulk material. The calculated splitting (146 meV in monolayer and 176 meV in bilayer, for MoS_2) nicely agrees with the A-B exciton separation. The CB minimum in K is also split, but in a much smaller value (4 meV). This splitting is attributed to the strong spin-orbit coupling and it varies between different members of the TMDC family (it is as big as 400 meV for WS_2).

The exceptionall strong light-matter interaction associated with the transition across the direct gap is one of the main reasons for the research community's interest in TMDCs. Bandgap increasing for reduced dimensionality is a quantum confinement effect observed in other materials, such as black phosphorous (BP) or indium selenide, but the shift from indirect to direct bandgap is quite unique [33], [34].

Mechanical properties of TMDCs, although they do not quite reach graphene's [35], are exceptional with big Young modulus and flexibility [36], [37], which added to their direct band gap and the high charge carrier mobility in the monolayer regime makes them perfect candidates for flexible optoelectronics.

1.2.2 Raman scattering in TMDCs

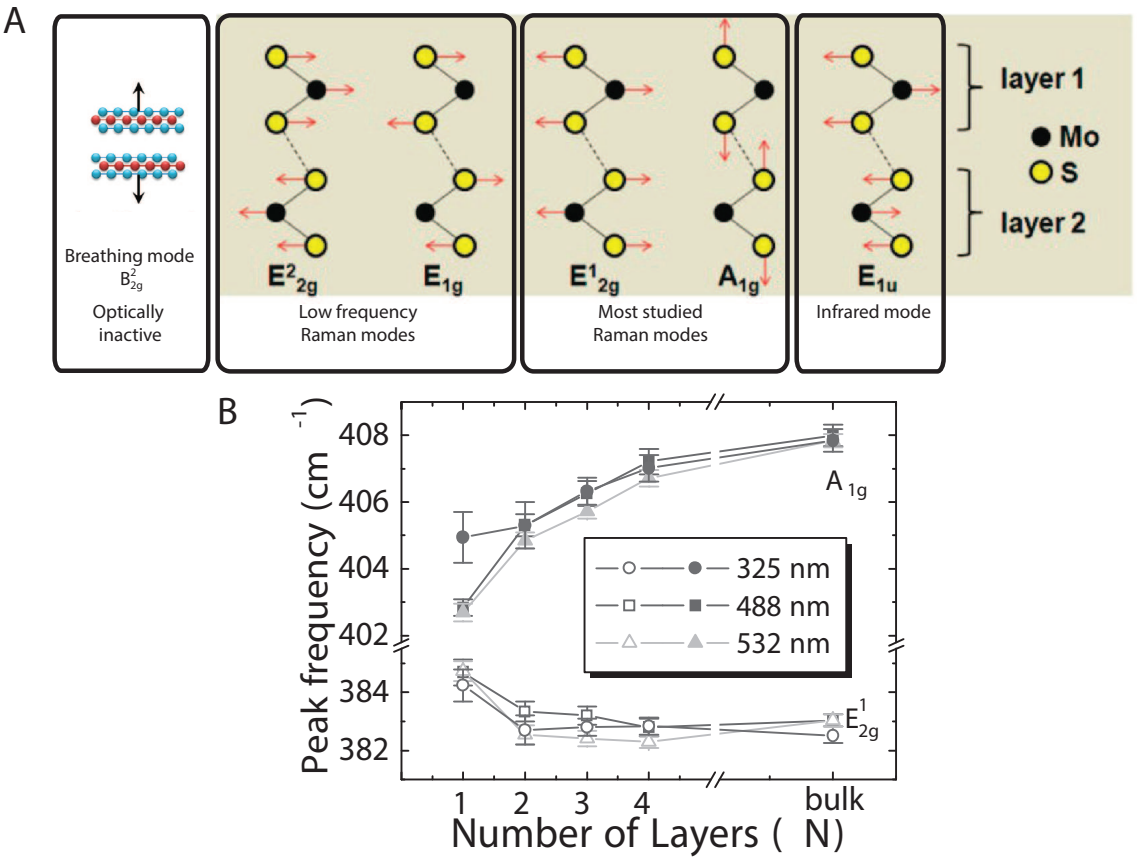


Figure 1.5: Illustration of the active lattice interlayer vibration modes [38] and intralayer E^2_{2g}, E_{1g}, E^1_{2g}, A_{1g} and E_{1u} [39]. (B) Evolution of E^1_{2g}, A_{1g} Raman modes frequencies with MoS_2 flake thickness for different excitation wavelength [40].

TMDCs have a common crystalline symmetry group. That means that all the materials of the family exhibit the same Raman modes. They will be located at different frequencies due to the different atomic masses and interatomic distances. Lattice vibrations in TMDCs can be described with a simple chain model where only interactions with the nearest neighbours are taken into account [38]. Due to the plane crystalline structure of TMDCs, their lattice vibrations mode can be grouped as in plane (shearing) modes and out of plane (breathing) modes.

Raman spectroscopy has become the main way to characterise TMDCs thickness [40], [41]. On one hand, the interlayer modes E^2_{2g} and B^2_{2g} logically vanish when we reach the monolayer regime, and could be good indicators of the flake thickness, but B^2_{2g} is optically inactive and E^2_{2g} is at low frequency (~ 30 cm^{-1}) and not every Raman spectrometer has the capability to measure so close to the laser line. On the other hand, E^1_{2g} and A_{1g} shift, red and blue respectively, as the number of layers is reduced (Fig. 1.5). They have been used to identify the number of layers in a flake [41], [42]. Raman scattering is powerful and useful for obtaining the number of layers in the flakes but there are other factors such as doping [43], temperature [44] or strain [45] that also affect spectral positions of Raman peaks. Then, it should be complemented with other spectroscopic or microscopic techniques.

1.2.3 Exfoliation and growth of TMDCs

TMDCs can often be found naturally occurring in mineral forms all over the world. The most obvious way to obtain mono- and few-layered TMDCs samples is to start from a pre-existing material of mineral origin and exfoliate it. One of the main reasons for the sharp rising of papers regarding 2D materials, beyond their interesting properties, is the ease of their availability. With conventional and cheap scotch tape, a crystal of the desired material, some training and a few hours of microscopy, it is possible to exfoliate and identify single and few layers of almost any layered material. Scotch tape is a broadly extended technique that produces flakes big enough for fabricating devices but just for research purposes due to the low productivity yield.

A big crystal of the selected material is put into contact with the glued side of an adhesive tape. The tape is removed and this process is repeated a few times with the material that remains attached to the tape and is then deposited on a substrate. Flake identification can be done with AFM. If the flakes are deposited onto a dielectric substrate of a certain thickness, the flake thickness can be identified using a simple optical microscope. For the particular case of MoS_2, 270 μm of SiO_2 on top of Si gives the optimal contrast [20] to identify layer numbers up to 6. As SiO_2 might not be the desired final substrate, flakes need to be transferred. There are different protocols for this last transfer, but generally a thin film of polymer is deposited on top of the substrate where the flakes are present. The polymer film is disattached from the substrate (taking with it the flakes) and deposited on the desired substrate. The polymer is then removed by soaking the sample in the proper solvent.

Another method, less widespread, is known as laser thinning. Starting from a pre-exfoliated few-layered flake it is possible to remove material layer by layer until the monolayer regime [46]. This technique allows us to choose the size and shape of the final monolayer area. Laser thinning produces flakes with similar quality to the mechanically exfoliated flakes. However, the disadvantage is that we need to start the process from a pre-exfoliated flake (it does not work for flakes thicker than 20 layers). This production technique as well as the scotch tape lacks production scalability.

Under certain conditions of temperature and inert gas flow it is possible to sublimate

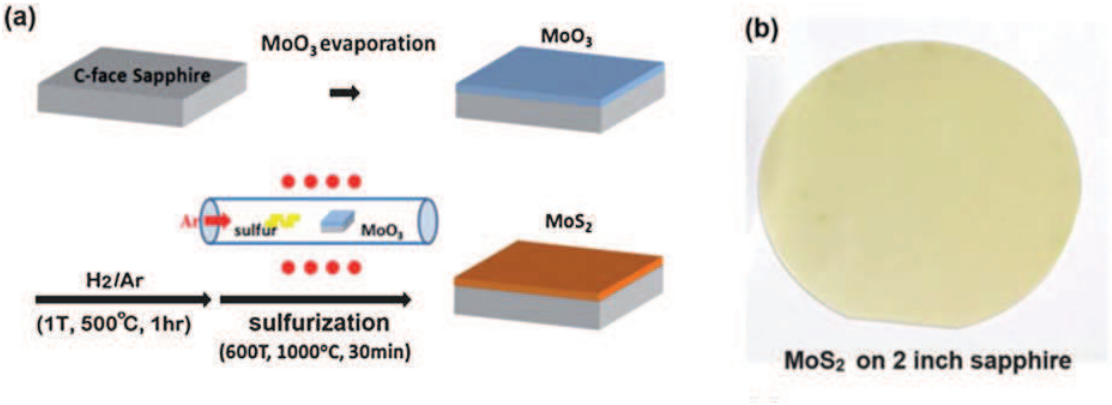


Figure 1.6: (A) Schematic representation of MoS_2 CVD growth. First a MoO_3 layer is deposited on top of shapphire. The sample is afterwards exposed to two thermal processes, under Ar-H_2 atmosphere at 500 °C for an hour and afterwards at 1000 °C in an Ar atmosphere with sulphur present for 30 minutes. (B) Final sample.

layer by layer until the monolayer regime. A layer of material per hour is removed from the flake. This process also reduces the flake's lateral size [47].

An alternative method that gives higher volumes of final material is the liquid phase exfoliation (LPE) [48]. There are several LPE techniques.

1. *Oxidation*: if the material is oxidized and dispersed in a proper solvent, it is possible to exfoliate it. Exfoliation can occur spontaneously [49] or under the effect of an external stimuli such as ultrasound. This method applied to graphene produces stable dispersion of mono- and few-layer flakes. In the particular case of graphene, the exposure of the material to oxidising agents creates hydroxyl and epoxide groups attached to the basal plane. This induces hydrophilicity which allows water molecules to intercalate in between layers.

2. *Intercalation*: some molecules, such as n-buthyllithium or IBr, can intercalate in between layers. If the dispersion is afterwards exposed to ultrasound or thermal shock [50], the flakes exfoliate. This method is not entirely appropriate for MoS_2, as it partially transforms the crystal phase [18]. The final polytype of the material is 1T which is metallic. Lately, there have been some efforts in transforming the flakes back to the 2H polytype [51].

3. *Ultrasonication*: by pouring the material in a solvent with similar solubility parameters (see Section2.3.1), the energy difference between the exfoliated and non-exfoliated material is very small and hence there is no reaggregation. This method was initially developed for graphene exfoliation by Hernandez et al. in 2008 [52], but has been proven as flexible and versatile for many materials such as graphene, transition metal oxides (TMOs) [53], [54], TMDCs [55], [56], [57], [58], [59], BN [60] or BP [61] among others.

A different strategy to obtain the monolayers is to follow a bottom-up techniques. Starting from precursor materials that contain Mo and S it is possible to obtain MoS_2 films. These processes need more than one step. There is an initial deposition where molybdenum is deposited (Fig. 1.6). During the second annealing step, the sample is

exposed to sulphur and the first deposited layer of material transforms to MoS_2. Among the three possible precursors(ammonium thiomolybdate, a thin film of deposited Mo or MoO_3), MoO_3 is the most broadly used because of a better quality of the final sample. CVD growth of MoS_2 is still in an early stage of development. The grains are rather small and the properties of the material are worse than the mechanically exfoliated one.

1.2.4 Electronics of TMDCs

Gordon Moore, in an excellent exercise of prescience, predicted in 1965 that the density of transistors on a chip and computing power will double every 24 months [62], [63]. The computing technology has followed his prediction quite well (Fig. 1.7). Transistors have permanently scaled their size and speed overcoming technological limitations. Nowadays, Moore's law is risking to fail, but not because of technological reasons. The main pursued strategy to increase computing power is to scale down transistor dimensions. This strategy is now facing fundamental limitations, such as subthreshold swing increase or provoking an increase of the current passing through the device while it is in the off state (I_{off}). Short-channel effects are expected to affect devices with channel lengths up to six times bigger than device's natural length (λ) [64], defined as:

$$\lambda = \sqrt{\frac{\epsilon_{ch}}{N\epsilon_{ox}} d_{ch} d_{ox}}, \tag{1.1}$$

where ϵ_{ch} and ϵ_{ox} are the dielectric constants of the channel and the oxide respectively, d_{ch} and d_{ox} are their thicknesses and N is the effective gate number (1 for conventional transistors and 2 for doubled gate transistors). A strategy to minimise λ and hence avoid short-channel effect is to choose an oxide of lower thickness and change the channel material by another with a higher dielectric constant.

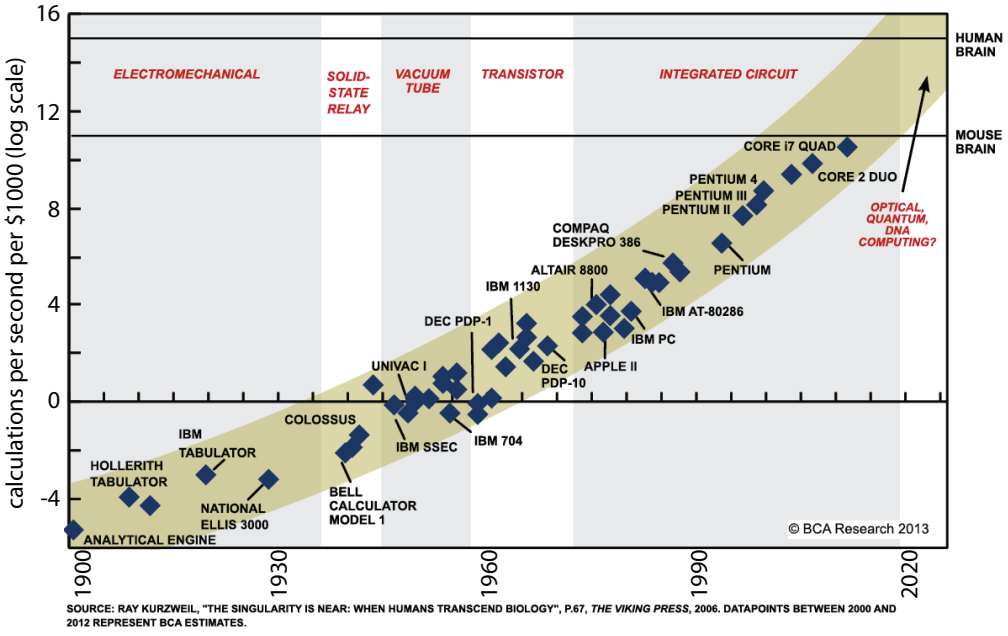


Figure 1.7: Graphical visualization of Moore's law.

If we want to reduce the size of transistors further, it makes sense to start using nanomaterials in their fabrication, in particular 2D materials. The best known among them is graphene. Graphene is an atomically thin layer of graphite. It was first reported in 2004 by Novoselov and Geim [14]. Graphene immediately attracted the attention of the research community due to its exceptional mechanical and electronic properties [65], [66] among others; extremely high mobility [67], it is the strongest material ever measured and it can be generously stretched [35].

Mobility is one of the first properties studied when a material is investigated for electronic applications. Higher mobilities give higher on–state current, I_{on}. A more interesting parameter to check whether a material is good for electronics is the on-off current ratio (I_{on}/I_{off}). Graphene has an extraordinary I_{on} but as it lacks a gap it can not be properly switched off, hence the I_{off} value is also high. In order to reduce the I_{off} value the material placed in the channel needs to have a bandgap. The higher the bandgap, the smaller the I_{off}. Empirical data show that mobility (I_{on}) is reduced as the band gap increases [68].

Despite all its exceptional properties graphene lacks a band gap. That excludes graphene as a material for logical electronic devices and future substitute of the silicon technology. TMDCs on the other hand have a bandgap, relatively high mobility values and their natural phase is semiconducting.

First TMDC transistors were done using bulk material (WSe_2 [69]). Even when the on/off ratio was poor, it exhibited high mobility and ambipolar behaviour. More recently, Radisavljevic et al. [20] fabricated a single-layer MoS_2 transistor that exhibited an I_{on}/I_{off} ratio as high as 10^8. Many reports followed that one, placing TMDCs, and MoS_2 in particular, as promising candidates for future optoelectronic technologies. Flash memories [70], amplifiers [71] or phototransistors [72] are just some examples of proof of concept reported devices.

1.2.5 TMDCs spintronics and valleytronics

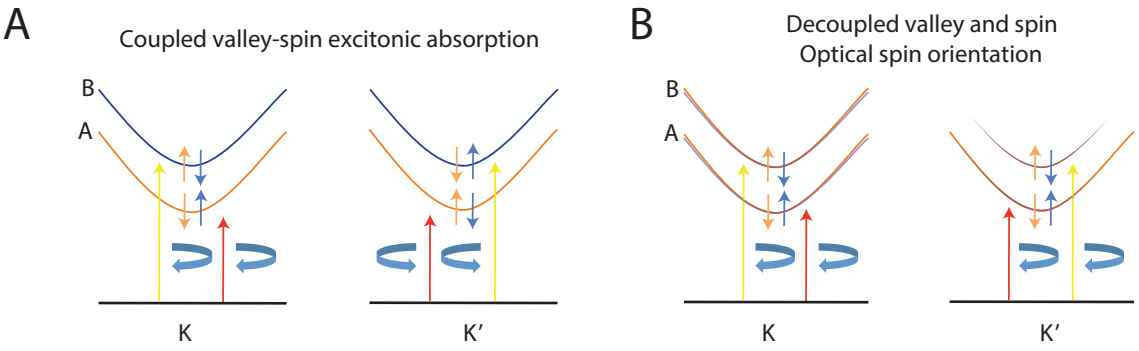


Figure 1.8: Schematic representation of the spin-valley polarization. (A) In monolayers different valleys are accessible with opposite circular polarization. (B) In bilayers this selection rules are different and both excitons in the same valley are accessible with the same polarization [73].

Typically the way to exchange information in electronics is through a flow of charges, where the presence of a charge flow indicates a 1 and the lack of this flow indicates a

0. More novel branches of electronics are paying attention to other properties of charge carriers to hold or transmit information such as spin or a material's quantum valley effect.

By controlling the quantized spin degrees of freedom it is possible to send simultaneously two signals through the same channel, which doubles the bandwith. 2D materials have been explored in this direction [74]. Due to its low spin-orbit coupling, graphene is a promising material for this applications [75], [76].

As already mentioned, spin-orbit interaction in TMDCs provokes the splitting in the maximum and minimum of VB and CB, respectively, but in addition it means that the two valleys at the $+K$ and $-K$ points of the Brillouin zone have spin valley coupling. Under an in plane electric field charges with opposite spins flow towards opposite valleys [73], [77], [78]. It is possible to selectively confine charges in each of these valleys and build a valleytronic device. Until now, it has been shown that we can selectively excite charges according to their spin. Access to spin-selected states is done via circularly polarized light. Spin valley polarization has been confirmed by polarization-dependent PL measurements, where the light emmitted from the TMDC monolayer keeps the polarization of the incident light [79]. Spin polarization relaxation lifetime has been measured and is around 1 ns.

1.2.6 Bound particles in TMDCs

If the electrons of the valence band are excited above the gap they tend to relax towards lower energetic states of the conduction band, seeking to be in a state with an energy as low as possible. Electrons can undergo processes such as electron-electron scattering or electron-phonon scattering in order to relax towards conduction band minimum. Similarly holes will relax towards the maximum of the valence band. A lower energy state can be achieved if an electron and a hole tie to each other in an intragap bound state, known as exciton. An exciton is an intra-bandgap (they have also been reported in metals as transient species) electron-hole bound particle. According to the size of the excitons we can differentiate two kinds:

- Frenkel excitons: they can be found in semiconductors with a low dielectric constant that enhances Coulomb interaction. Electron and hole are strongly attracted to each other and they remain in a small volume (typically in a volume equal to or smaller than a unit cell). Typical Frenkel excitonic binding energies are around 1 eV.

- Mott-Wannier excitons: they are present in semiconductors with a higher dielectric constant. That provokes screening and Coulomb interaction is reduced. As electron and hole are more separated, they feel less of each other and Coulomb interaction is weaker.

Excitons are one of the main (optical) spectral features in TMDCs and hence they have been used to characterize them. There are three main resonances in TMDCs absorption spectra named as A, B and C (from lower to higher energy transition). A and B excitons are placed in the K valley of the Brillouin zone, where the bandgap is in the monolayer regime. The resonance C is assigned to a band nesting region close to the the Γ point. By studying the PL excitation spectra of mono- and bi-layer Kozawa et al. [80] clarified this picture. Photoexcited electrons and holes in the band nesting region relax towards the minimum of the conduction band and the maximum of the valence band respectively with equal velocities but opposite signs. This provokes a spontaneous separation of electron-hole pairs, meanwhile the carriers photoexcited at K point remain closer in the reciprocal space.

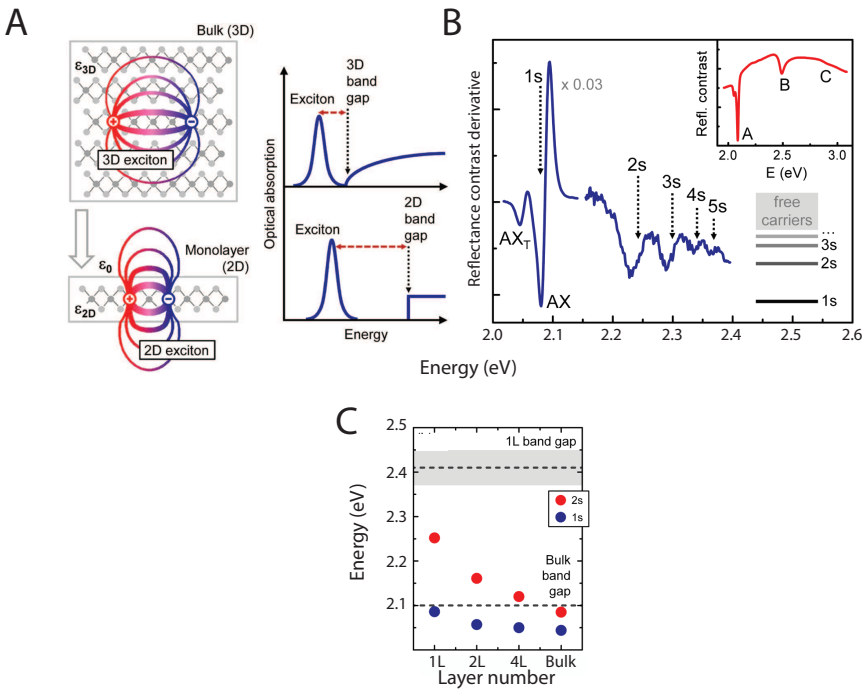


Figure 1.9: (A) Representation of an exciton and its electric field, binding energy and bandgap of WS_2 from bulk case and monolayer regime. (B) The derivative of the reflectance contrast spectrum (d/dE) $(\Delta R/R)$ of a WS_2 monolayer and its reflectance contrast spectrum (inset). (C) Experimentally and theoretically values of exciton binding energy as a function of the number of layers [31], [32].

Excitons in TMDCs within the plane have a Mott-Wannier behaviour and their binding energy has been calculated by measuring the excitonic energy level series (Fig. 1.9) [31], [32] (because of the lack of inversion symmetry the different excitonic levels can be measured from a single photon absorption spectrum or by measuring the PL excitation line). The series of excitonic energy levels can be obtained my measuring the reflectance contrast spectrum at low temperature (5 K). The reflectance contrast spectrum can be obtained from the formula:

$$\frac{\Delta R}{R} = \frac{R_{Sample} - R_{substrate}}{R_{substrate}}, \tag{1.2}$$

where $R_{substrate}$ is the light reflected by the substrate in the abscence of the sample and R_{Sample} is the light reflected by the sample (the reflectance contrart spectrum of WS_2 can be observed in Fig. 1.9 B inset). The width of the different excitonic transitions at 5 K is narrow enough to observe their position in the second derivative of the reflectance contrast spectrum (Fig. 1.9 B). The binding energy of the excitons (how deep they are inside the gap) is normally obtained by fitting the experimental energy transition to a hydrogen series:

$$E_b^{(n)} = \frac{\mu e^4}{2\hbar^2 \epsilon_n^2 (n-1/2)^2}, \tag{1.3}$$

$$\tag{1.4}$$

where n is the quantum number of the state and ϵ_n is the material's dielectric constant and μ is the reduced mass of the exciton. This model successfully describes the exciton energy level serie in bulk materials. In a 2D scenario (i.e. an exciton in a semiconducting TMDC monolayer) there is a fraction of the exciton's electric field that is out of the media (Fig. 1.9 A). This causes that the effective dielectric constant is lower than the material's. The fraction of electric field out of the flake is bigger for those states with lower quantum number, hence a quantum number dependent effective dielectric constant must be introduced in Eq. 1.3:

$$\epsilon_n = \left(2\hbar^2 E_{b,expt}^{(n)}(n-1/2)^2/\mu e^4\right)^{-1/2}, \tag{1.5}$$

where $E_{b,expt}^{(n)}$ is the experimental nth exciton level of the series. Once this correction is included in Eq 1.3 it is possible to fit the data and obtain how deep the excitonic ground state is inside the bandgap. Hundreds of meV have been obtained (~320 meV in WS_2 and ~440 meV in MoS_2). Such a big binding energy results in long exciton lifetime in monolayer TMDC. A direct consequence of this is that many of the electronic and optoelectronic properties are ruled by an excitonic behaviour. Later experiment measured how the excitonic binding energy increases as the number of layer decreases (Fig. 1.9 C) [32].

The gradual transition from indirect to direct bandgap as we approach the monolayer regime has a strong fingerprint in the optical properties. It has been shown how the PL quantum yield (QY) can increase by 3–4 orders of magnitude between bulk and monolayer [28] (Fig. 1.10 A). The total QY is still quite low (10^{-2}) but under the proper chemical treatment and at low excitation regime a QY as high as 1 can be reached [81]. PL also shows how the indirect bandgap changes with thickness and that this shift is stronger than the direct (optical) bandgap.

Excitons have, in principle, in plane freedom of movement, and after photoexcitation they tend to diffuse. Excitons can get trapped at defects, which allows to find the areas with higher density of (trapped) excitons by mapping the PL emission of the flakes [82]. PL from excitons trapped at defects tends to exhibit a broader emission than free

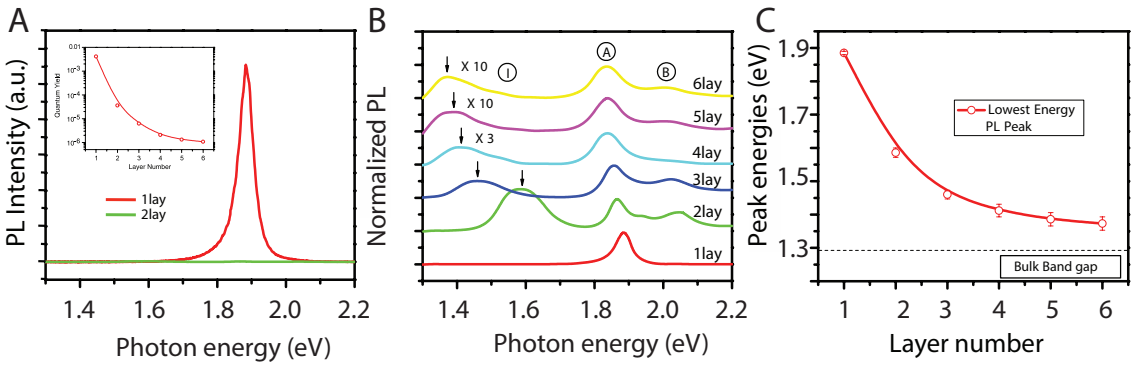


Figure 1.10: (A) PL intensity comparison between MoS_2 mono- and bilayer. Inset: evolution of quantum yield with the number of layers (B) Spectral fingerprint of bandgap rearrangement for six to one layer sample thicknesses. (C) Exciton bandgap increases as the sample is thinned [28].

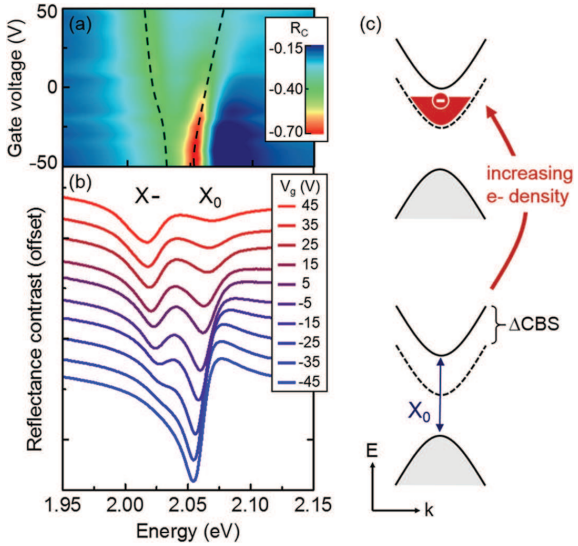


Figure 1.11: (A) PL color plot of the reflectance contrast spectra for different gate voltages (level of doping). Sample is expected to be neutral at V_g= -45 V and increases its electron density by 0.8×10^{12} cm^{-2} for each 10 V. Dashed lines indicate the center position of excitonic(X_0) and trion(X_-) transitions. (B) The same as (A) but for selected gate voltages, offset for clarity. (C) Schematic representation of WS_2 energy band structure around the fundamental bandgap with and without electron doping where X_0 indicates the bright exciton transition and ΔCBS the conduction band splitting [84].

excitons. It has been shown for LPE WS_2 flakes that the exciton emission full with half maximum is insensitive to temperature, what reflects the heterogeneous distribution of trapped excitons binding energies [83].

Low temperature measurements indicate the existence of dark excitons. A dark exciton is an exciton whose lowest energetic state is not accessible from a single absorbed photon process. Its energy is close to the energy of the next higher state and a signature of its existence is the reduction of the PL intensity as we decrease the temperature [85], when the opposite is expected.

A trion is a charged exciton, that is, a bound electron-hole pair coupled with an electron (hole). The presence of trions in semiconductors is a signature of doping. They radiatively recombine and can be tracked either in absorption spectra [86] or in PL spectra [84], [87]. The trion binding energy is the energy needed to dissociate the electron (hole)-exciton state. It can be obtained from the PL spectra as the energetic separation of trion and exciton peak and is around 40 meV. This value is not constant, as the level of doping increases so does the charge screening and the trion PL peak strongly red-shifts. Excitonic resonance also shifts because of screening and bandgap renormalization [84].

Doping in TMDC flakes can be controled if a transistor is built using a TMDC flake. By varying the gate voltage, positive and negative doping can be induced in the flake. PL measurements proved the existence of positive and negative trions, and its screening (Fig. 1.11) as a function of the density of carriers in a transistor [87].

1.2.7 TMDCs and nonlinear optical properties

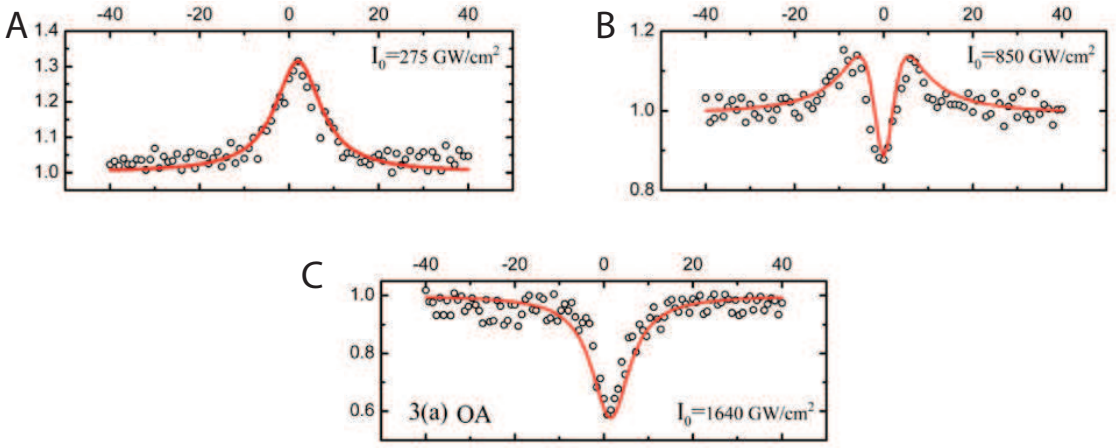


Figure 1.12: Z-scan transmission results in (A) increase of transmission due to SA, (C) reduction of transmission due to TPA or RSA and (B) intensity regime where SA and TPA are both present [88].

Open and close Z-scan experiments are performed in order to obtain the non-linear refractive index of a material. If a laser beam is focalized the field intensity increases as we get closer to the focal plane. By placing a sample at different distances from the focus (z) it is possible to study how the intensity of transmitted light changes as a function of initial intensity, this is known as open Z-scan. If we place an iris before our detector (close Z-scan) we can observe the intensity of the Kerr effect in the sample. Saturation of absorption (SA) is a process particularly useful in laser technology, as it can be used to decrease pulse lengths or to make pulsed emission dominant in the laser cavity.

Due to its direct application, as laser mode-locker or Q switcher [89], [90], few-layer MoS_2 and WS_2 non-linearities were rapidly characterised [88], [91]. SA properties of TMDCs have been reported typically in fiber laser disposition due to the ease of placing the sample inside the laser cavity (TMDC-composite film in between two fiber ferrules or even just by drop casting a TMDC dispersion in the fiber connector) or by interacting with the light's evanescent field in tapered optical fibers.

At higher intensities than those needed to observe SA, two–photon absorption (TPA) can be observed as an increase of the absorption. This is known as reverse saturable absorption (RSA). SA and RSA can be studied and modelled (Fig. 1.12) in the same experiment with the following formula [92]:

$$\alpha(I) = \frac{\alpha_0}{1 + I/I_S} + \beta I, \tag{1.6}$$

where β is the TPA coefficient, I_S is the saturation intensity and α_0 is the absorption in the low intensity regime.

Strong second harmonic generation (SHG) has been reported in WS_2 and MoS_2 [21], [23] and it has been used to build a Frequency-Resolved Optical Gating (FROG) detector to characterize ultra-short laser pulses [93]. The SHG efficiency depends on many factors such as phase matching and the different propagation speeds of fundamental and

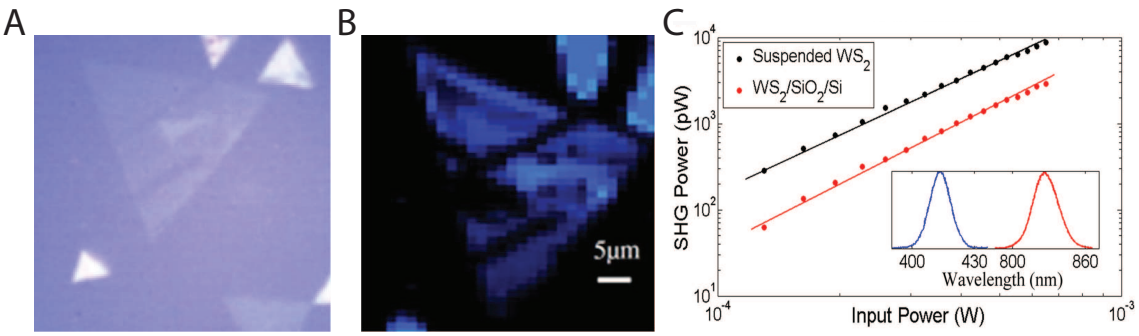


Figure 1.13: (A) Optical image of a WS_2 monolayer. (B) SHG map of the same monolayer [93]. (C) SHG pump power dependence. Inset: fundamental and doubled spectra [23].

doubled frequency. Due to the intrinsic 2D structure of the flakes, the light propagates through the materials along just 0.6 nm (WS_2), strongly relaxing the phase matching restrictions and increasing their doubling bandwidth. One can see how that is influenced by thickness in the expression of the doubled field [23]:

$$A_2(2\omega) \quad \propto \quad S(\omega)\,\mathrm{sinc}\left(\frac{\Delta k}{2\pi}L\right), \tag{1.7}$$

where $S(\omega)$ is the Fourier transform of the fundamental pulse, $\Delta k = k_\omega - k_{2\omega}$ is the phase mismatch between the fundamental and doubled frequency, $\delta = v_{g1}^{-1} - v_{g2}^{-1}$ is the group velocity mismatch parameter (difference of the inverse group velocities of fundamental and doubled frequency) and L is the crystal thickness. If $\Delta k = 0$, the doubled field is proportional to $\mathrm{sinc}\left(\frac{\Delta k}{2\pi}L\right)$ which will act as an effective bandwidth $\sim (\delta L)^{(-1)}$. The smaller L, the broader the doubled spectra. As the SHG is produced in a single flake of 0.6 nm thickness, SHG generation is efficient over a large spectral range

1.2.8 Photoexcited states dynamics

An important thing to consider before starting to study femtosecond dynamics of photoexcited states in TMDCs is that even when experimental results (lifetimes or spectral features) are consistent in between different reports, they tend to have a different interpretation. Similar spectral features or decay may be assigned to different phenomena. There are also differences in experimental setup (pump fluence regime, excitation in or out of resonance, delay window, fitting model etc). Production technique and quality of the measured sample is also not standarized. In this subsection I will try to shed some light on previous work on photoexcited states dynamics.

In one of the first reports about photoexcited states dynamics in MoS_2 Shi et al. [94] measured photoexcitation lifetimes of mono- and few-layer MoS_2. This experiment was performed in an unconventional way, as the probe pulse power was stronger than the pump pulse's. They describe the dynamics as the sum of three exponential processes. While in the mono- and few-layer sample the signal rises within the time resolution of the setup followed by three decay processes, in the bulk sample there were two delayed (slower) rising processes followed by an exponential decay in the nanosecond timescale.

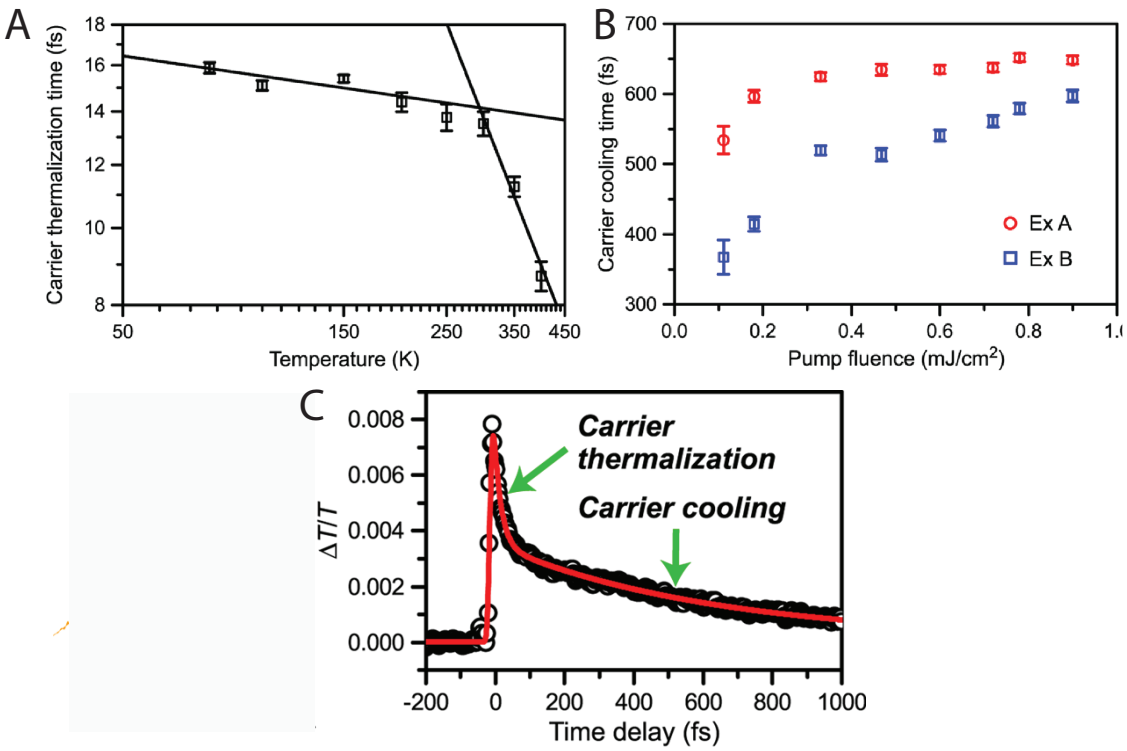


Figure 1.14: (A) Evolution of the short (thermalization) lifetime <20 fs with temperature. (B)Evolution of the 100's fs lifetime (cooling) with fluence. (C) Experimental (empty circles) and fitted (red line) of sub-ps dynamics in MoS_2, assigned to a cooling and a thermalization process [95].

They suggest that the photoexcited population in the monolayer undergoes a starting intraband relaxation faster than 500 fs followed by three processes; the first one of the order of few ps, in which excitons are trapped by surface states, the second one in tens of ps, in which the electron and holes scatter with phonons and relax to the minimum of the conduction band and to the maximum of the valence band (respectively); third lifetime of the order of hundred of ps was assigned to direct recombination of excitons.

The two rising processes in the bulk sample were assigned to a much slower carrier-carrier (~2 ps) and carrier-phonon (~20 ps) scattering during cooling and thermalization. Intervalley exciton relaxation was assumed as the process beyond the relaxation lifetime of 2.6 ns.

In a setup with better temporal resolution Nie et al. [95] performed an experiment with ~10 fs time resolution, where they studied the dependence of two observed lifetimes (<20 fs and ~600 fs) on the fluence and the temperature. They assigned these lifetimes to carrier thermalization and carrier cooling (Fig. 1.14). Carrier-carrier and carrier-phonon scattering contributes to the ~ 20 fs thermalization process (in agreement with Wteinhoff et al. calculations [96]) meanwhile the carrier cooling is assigned to phonon emission.

Wang et al. published two articles [98], [99] where the energy of the probe photons was 1.37 eV. That energy probes the intragap states of the material (defects). By doing so they identify two trapping processes, one of ~ 2 ps and another of hundreds of picoseconds. Auger scattering was the trapping mechanism, when two carriers scatter they exchange energy and the one which ends with less energy is trapped at a de-

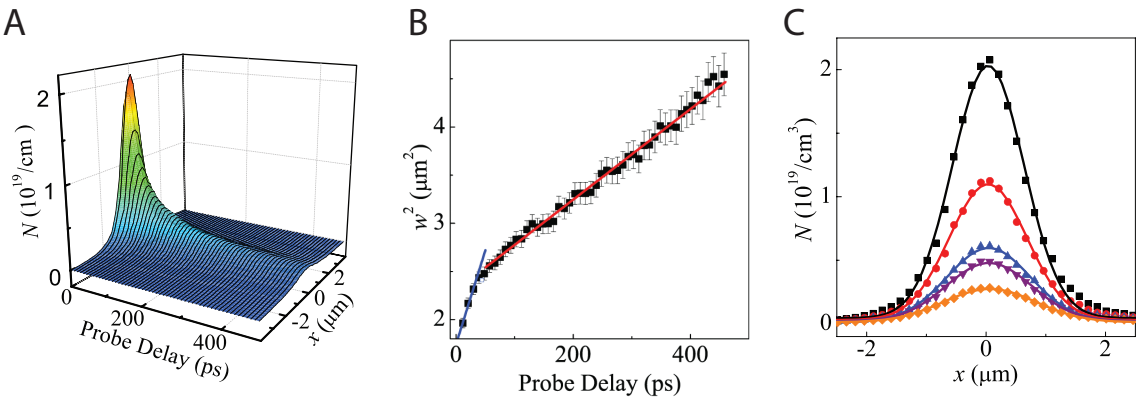


Figure 1.15: (A)Distribution of signal (carriers) as a function of delay and relative position of pump and probe pulse, (B) squared width of the spatial profiles a function of pump-probe delay. (C) Spatial distribution of signal (charges) width at the selected delays of 10, 30, 75, 100 and 200 ps (black, red, blue, purple and orange respectively) [97].

fect(Fig.1.16. They studied how the sample thickness affects that trapping and found a thickness-dependent trapping rate, assigned to the higher sulphur vacancies density as the number of layers is reduced.

There is a set of scientific works that rest a big part of their interpretation not just on the lifetime value or its evolution with other parameters but also on the spectral shape of the pump-probe signal. A lot of new information can be collected in this way.

Pump-probe spectra of MoS_2 has some features common to all the reported studies. It can be described as an alternation of positive and negative peaks. That can be interpreted as a derivative shape. Sim et al. [100] base their interpretation in shifts and broadenings of excitonic resonances. In this way they base their interpretation on A-B interexcitonic interactions. Following a transition broadening explanation of the excitonic resonances, Cunningham et al. [101] observed an increase of the photoconductivity in the decay lifetime of 600 fs. They assigned that to a charge relaxation process, but it might also indicates an increase in the charge carrier number via dissociation of excitons.

Borzda et al. [102] used femtosecond pump-probe measurements and continuous wave photomodulation to make an accurate description of the spectral shape and its

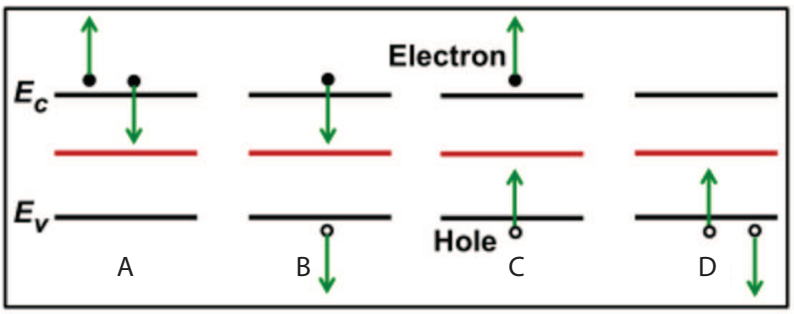


Figure 1.16: Auger processes for the trapping of electrons (A and B) and holes (C and D) (Suplementary info of [98]).

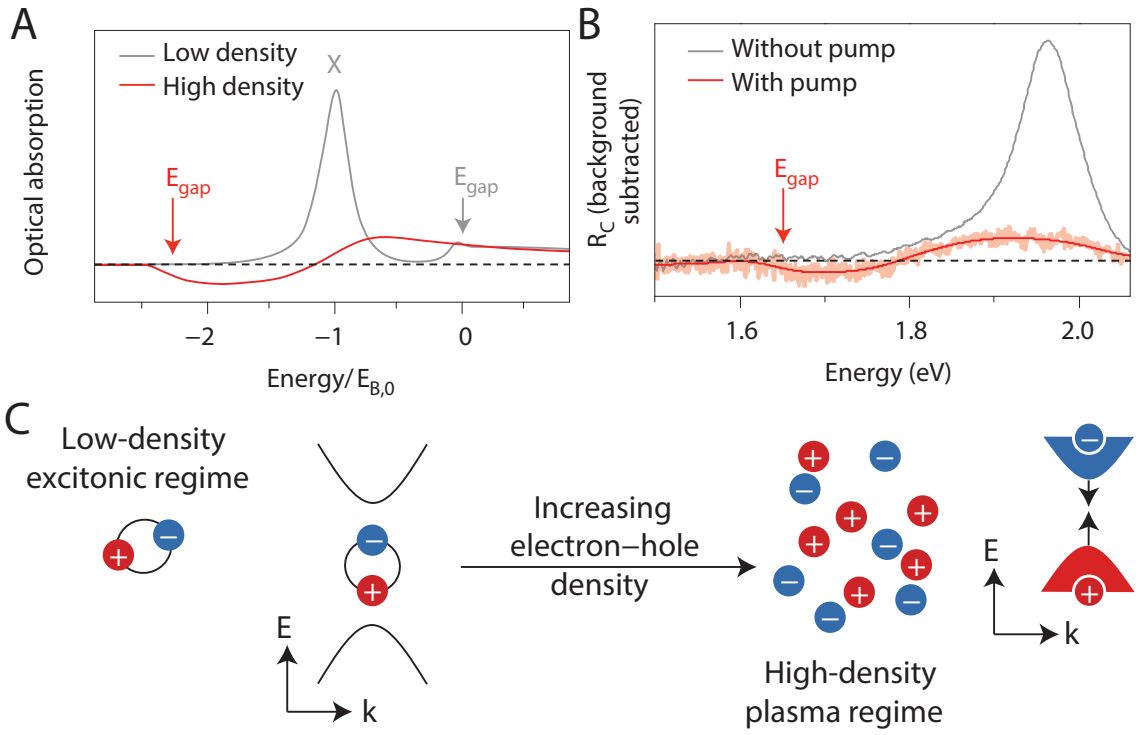


Figure 1.17: (A, B) Predicted and experimentally observed bandgap renormalization in WS_2. (C) Schematic representation of the transition between the low density excitonic regime until the electron hole plasma regime (Mott transition) [105].

evolution, including a starting blue shift of the signal. They introduce a fitting procedure based on a cascade model that is able to fit the full spectra over the whole delay window. (an extension of this model is used in the experiments explained in Chapter 4). They obtained two lifetimes. Their analysis focused on the shorter one (~ 700 fs), which was assigned to exciton dissociation (photogeneration of charges).

If the pump fluence is kept in the linear absorption regime, the level of the signal can be identified as a magnitude proportional to the number of photoexcited states. Then, by scanning with the probe pulse in a radial direction of the pump pulse on the sample, the spatial profile of photogenerated state can be obtained. By repeating this procedure for different delays it is possible to study the diffusion of photoexcited states in the material as Wang [103] and Cui [104] did. They obtained the diffusion constant for MoS_2 (20 cm^2/s) and WSe_2 (15 and 9 cm^2/s for monolayer and bulk, respectively). Kumar et al. [97] in a similar experiment identified two different diffusion regimes, one for short delays with a diffusion constant of 18 cm^2/s and a second one dominated by scattering with defects with a diffusion constant of 4 cm^2/s.

As we are dealing with a 2D semiconductor all our photoexcited states will be confined to a plane. If by increasing pump fluence we increase the density of photoexcited states, we will be shifting the regime towards a scenario where many-body effects become important.

The first report about many-body effects was about exciton-exciton annihilation in $MoSe_2$ [106] closely followed by a similar experiment in MoS_2 [107]. In both studies, with similar pump fluence ($50\mu J/cm^2$), the signal relaxation was not properly fitted with

a multi-exponentional model and the relaxations follow a quadratic differential equation:

$$\frac{dN}{dt} = -k_A N^2, \tag{1.8}$$

where N is the population of excitons and k is the annihilation rate. In MoS_2 the exciton-exciton annihilation is $k_A = (4.3 \pm 1.1)\times^{-2}$ cm^2/s what leads to an equivalent lifetime (from a biexponential fit) of 11 ps at a density of excitons of 10^{12}(46 μJ/cm^2 pump fluence). Because of the interest of the researchers in many-body phenomena, exciton-exciton annihilation has been studied also via time-resolved photoluminescence (TRPL). Mouri et al. [108] measured a much longer equivalent lifetime. Also in WS_2 a much longer exciton-exciton annihilation lifetime has been reported [109]. TRPL and pump-probe measurements gave arguments towards exciton-exciton annihilation in completely different time regimes. As PL origin is assigned to excitons recombination, TRPL gives information just about excitons, meanwhile in pump-probe this assignment cannot be done 100% as non–radiative processes are also measured. As excitons need to diffuse before they scatter with another and annihilate, lifetime of the process depends on exciton mobility.

There are more many-body effects beyond exciton-exciton annihilation that emerge as the pump fluence is increased. Bandgap renormalization arises as the dominant effect for high pump fluences in monolayer TMDCs. It was initially predicted for MoS_2 [110] and observed afterwards in WS_2 [105] (Fig. 1.17). If a WS_2 monolayer is in the high exciton density regime, it can undergo the so–called Mott transition where the picture of photoexcited states changes. As the number of charges increases, the screening of their Coulomb interaction also increases. At a certain point this screening is so strong that the exciton binding energy vanishes and there are no longer electron-hole bound states present in the sample and the exciton resonance dissapears. Then, the photoexcited species are electrons and holes in a plasma. The vanishing of the exciton binding energy is not the only consequence of the screening between charges. It also reduces the quasi particle energy, red-shifting the bandgap.

In 2016 a theoretical calculation supported by an empirical measurement of pump-probe in monolayer MoS_2 claimed that the transient absorption signal is the result of a combination of Pauli blocking and a renormalization of the exciton binding energy [111]. As the excitonic resonance spectral features were visible in the pump-probe spectra, that would mean that band-gap renormalization is present at pump fluences much lower than those needed for Mott transition (10 μJ/cm^2, seven times lower).

Chapter 2

Methods

This chapter describes the techniques used to exfoliate TMDCs and to perform a characterisation of their physical properties including their photoexcited species dynamics.

A brief introduction to femtosecond pulse generation and nonlinear optics is present in this chapter for a better understanding of the physics behind some processes present in our experimental setup. The chapter also contains references to suggested further reading about lasers and nonlinear optics.

2.1 Fluorescence, Absorption, Extinction and Raman Spectroscopy

Spectroscopy is a broad field used to characterize matter through its interaction with radiation. Bunsen and Kirchhoff (1859) were the first who developed a spectroscope. The idea came to them when they were watching a fire in the Hamburg harbour. When they looked at the light through a prism they observed a bright yellow light, similar to the light produced by sodium combustion. Later, they discovered that the building which was burning that day was a salting stock. They thought that if they had been able to discover the origin of that fire, maybe it was possible to identify the composition of different materials just by studying the light which arrives to us from them.

Following that idea they developed a basic spectroscope which allowed them to identify which materials were in the sun (in fact helium was discovered in the sun rather than on Earth) [112], [113]. Lots of different spectroscopic techniques have been developed since then. Those used in this thesis are explained in the following.

2.1.1 Absorption and extinction

When light passes through a medium, it is attenuated. This attenuation is a function of material properties (Γ), frequency of light(ω), initial intensity (I_0) and optical path length (L).

$$dI(\omega) = -I_0(\omega)\Gamma dL \tag{2.1}$$

Integrating Eq. 2.1 :

$$I(\omega) = I_0(\omega)e^{-\Gamma L} \tag{2.2}$$

Eq. 2.2 is the Beer-Lambert law. Lambert, starting from Bouguer's [114] studies, proposed that attenuation of light is proportional to sample thickness [115]. Beer [116]

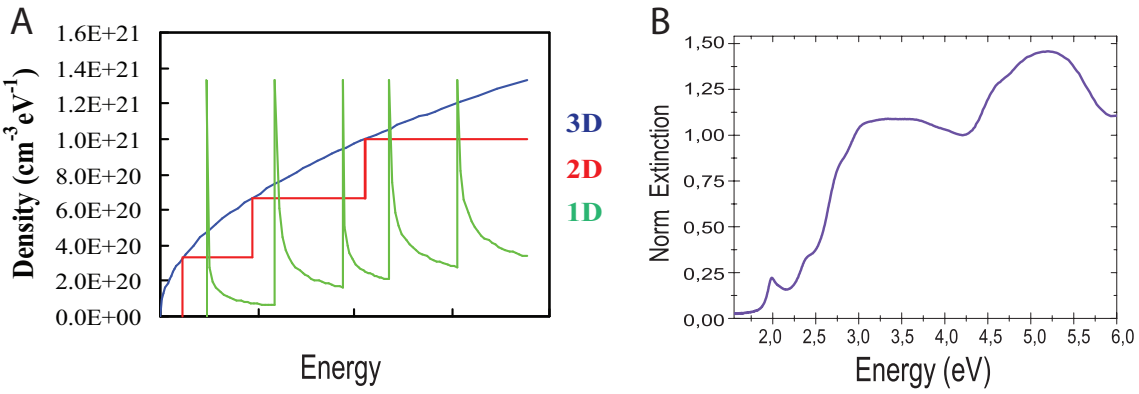


Figure 2.1: (A) Density of states in the CB for the tri-, bi- and unidimensional semiconductor. (B) Extinction spectrum of LPE WS_2.

stated that the attenuation is proportional to the concentration of absorbers c, where α is the absorption coefficient. α is directly proportional to the concentration of the absorber material and the absorption cross section σ of the material for the frequency ω.

$$I(\omega) = I_0(\omega)e^{-\alpha L} \tag{2.3}$$

$$\alpha = \sigma(\omega)c \tag{2.4}$$

$$I(\omega) = I_0(\omega)e^{-\sigma(\omega)cL} \tag{2.5}$$

From here we can define the absorbance as:

$$A = \sigma(\omega)cL = -\ln\frac{I}{I_0} \tag{2.6}$$

In the simplest case, σ depends on the density of states ρ (DOS) of our material. The density of states per unit of volume and energy can be easily calculated and depends on the dimensions of the material.

$$\rho(E)_{3D} = \frac{dN_{3D}}{dE} = \frac{8\pi\sqrt{2}}{h^3}m^{*3/2}\sqrt{E-E_{\min}} \quad \text{for} \quad E > E_{\min} \tag{2.7}$$

$$\rho(E)_{2D} = \frac{dN_{2D}}{dE} = \frac{4\pi m^*}{h^2} \tag{2.8}$$

$$\rho(E)_{1D} = \frac{dN_{1D}}{dE} = \sqrt{\frac{2\pi m^*}{h^2}}\frac{1}{\sqrt{E-E_{\min}}} \quad \text{for} \quad E > E_{\min}, \tag{2.9}$$

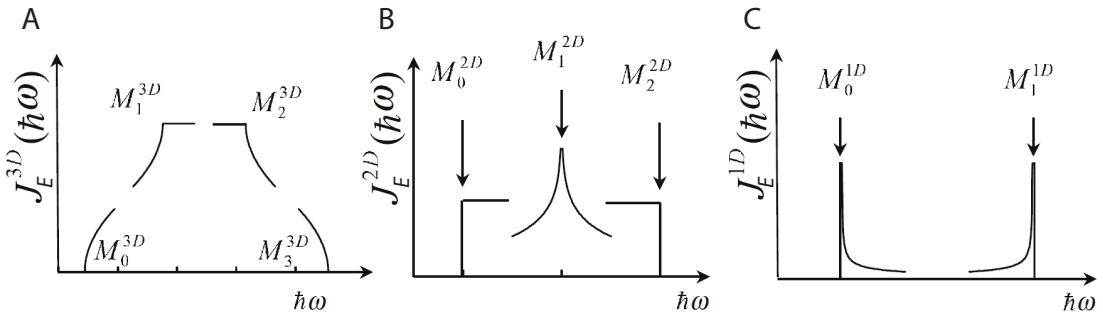


Figure 2.2: Van Hove singularities in the Joint density of states for A) 3D, B) 2D, and C) 1D materials.

E_{min} is the the energy at the bottom of that energy band. Eqs. 2.7, 2.8, 2.9 represent the DOS for the case of a tridimensional, bidimensional or unidimensional material. That leads to a DOS (and hence an absorption spectra) with a shape like the one in Fig. 2.1 A.

The red line of Fig. 2.1 A represents the bidimensional case. If intra gap excitons are present in our material, there will be an extra spectral feature, a bump present at lower energies than the edge of the step (see section 1.2.6). These spectral shapes are perfectly recognisable in the absorption spectra of all exfoliated TMDCs (Fig. 2.1 B).

This connexion between ρ and the absorption is valid if the optical transition is between two narrow bands. If this is not the case the Joint density of states (J) must be taken into consideration:

$$J(E) = \frac{2}{(2\pi)^3}\int_E \frac{dS}{\nabla_{\vec{k}} E(\vec{k})} \tag{2.10}$$

This integral has to be carried out over the constant energy surface S, where $E(\vec{k}) = E_{conduction}(\vec{k}) - E_{valence}(\vec{k})$. This expression diverges at those points of the Brillouin zone where $\nabla_{\vec{k}} E(\vec{k}) = 0$. If J diverges the optical transition reaches its maximum probability. This behaviour will be observed under the following scenarios.

$$\nabla E_{conduction}(\vec{k}) = \nabla E_{valence}(\vec{k}) = 0 \tag{2.11}$$

$$\nabla E_{conduction}(\vec{k}) = \nabla E_{valence}(\vec{k}) \neq 0 \tag{2.12}$$

These conditions are fulfilled in those points where conduction and valence band are parallel (and horizontal for Eq. 2.11). In the particular case of semiconducting TMDCs, the k point of the Brillouin zone fulfil Eq. 2.11 condition and Eq 2.12 is fulfilled in the band nesting area close to γ point. These points are known Van Hove singularities. Van Hoves singularities are labelled as M_0, M_1, M_2 and M_3 and they will be labbelled according to the shape of conduction and valence bands. Minima in the band separation are labelled as M_0, saddle points are labelled as M_1 and M_2. M_3 represents a maximum in the interband separation. Plots of the joint density of states for all the different kind of critical points can be observed in Fig. 2.2.

When light passes through a medium, absorption is normally the dominant extinction process. This is true for gases, crystalline solids or molecules dispersed in liquid. But when we have particles, or structures, inside our media with dimensions comparable to light's wavelength, scattering becomes much more efficient and must be considered. We are working with bidimensional flakes dispersed in liquid. The lateral sizes of such flakes range from 40 nm for the smaller ones until 2 μm. I mainly work with visible light, whose spectrum goes from 400 nm to 800 nm. Inside this range we have to consider scattering processes. Hence, contrary to a significant part of the literature, we use the term absorption only for pure absorption of light (A in Eq. 2.6), and extinction for the combined effect of absorption and scattering.

Extinction spectra are measured in a common UV-VIS spectrometer where the attenuation between the incident light and the light that arrives to the detector is measured. Absorption spectra are measured in integrating spheres. An integrating sphere is a device that collects the transmitted light (extinction) and the scattered light (scattering). As extinction is the sum of scattering and absorption, absorption can be easily obtained by subtracting the scattering from the extinction.

Extinction and absorption spectra are useful techniques to characterise 2D nanoflakes because due to confinement effects, the position and shapes of some spectral features change with the thickness and lateral size of the flakes [117], [118].

2.1.2 Photoluminescence

PL was first reported by the Spanish missionary B. de Sahagún in 1560 and published by N. Monardes [119]. B. de Sahagún noticed that a tea produced from kidneywood (*Lignum Nephriticum*) exhibits a blue fluorescence which is caused by the substance called *matlanine* [120]. PL is the spontaneously emitted light by a material that has previously been excited by light. It is useful to identify and characterize radiative transitions (as it happened with hydrogen with the Lyman series and for hydrogenic atoms with Rydberg formula) [121]. When a material is excited, electrons are pumped from their ground state into excited states. As they are now in a non-equilibrium state they will undergo different relaxation processes. These relaxation processes can be either through radiative transition, through a nonradiative transition or through a combination of both. If there is a radiative decay, the mechanism to preserve the system's energy is the emission of photons. These emitted photons can be measured to characterize the transition (Fig. 2.3).

- *Fluorescence*: After optical excitation an electron relaxes from an excited state to its ground state. In order to keep the energy of the system constant a photon of light is emitted. The typical time scale of the process is of tens of nanoseconds or faster.

- *Phosphorescence*: The process is basically the same as fluorescence but in between the excitation of the electrons and their radiative relaxation electrons are stored in metastable electronic states (such as triplets). These electrons are released normally through slow, thermally-activated processes. Besides the different relaxation path of excited electrons, phosphorescence differs from fluorescence in the timescale of the process, typically in the order of miliseconds, but it can last several hours.

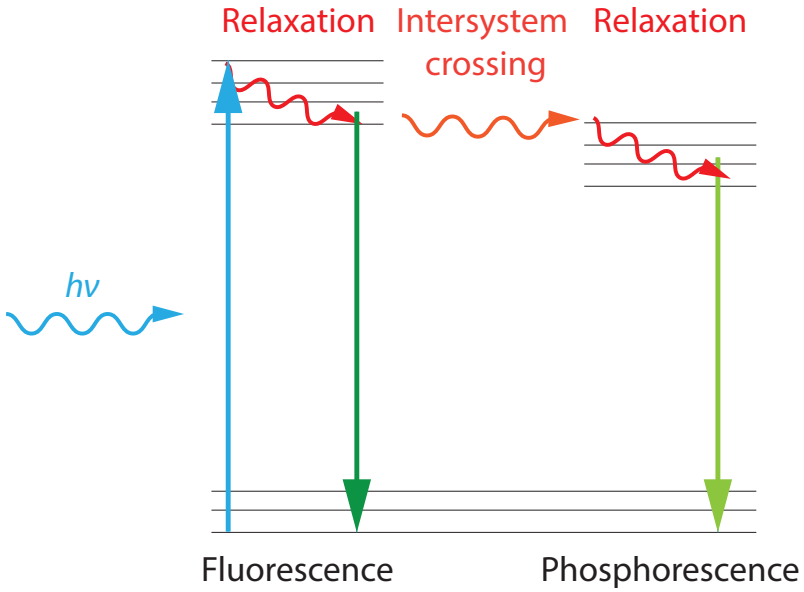


Figure 2.3: Fluorescence and phosphorescence schematic representation.

Recombination of an electron and a hole in a bound state (exciton or trion) is the origin of the PL in semiconducting TMDCs. PL is a non-intrusive way to determine their optical bandgap. It can give information about exciton and trion binding energy or level of doping.

Semiconducting TMDCs undergo a transition from indirect to direct band gap as they go from bulk to monolayer. As only monolayers have a direct bandgap, their light emission yield is several orders of magnitude higher than that of bi-, tri- and few-layer TMDCs. That makes photoluminescence a powerful tool to identify monolayers, or the monolayer content in dispersions.

2.1.3 Raman spectroscopy

When photons pass through a medium, they are subject to scattering processes. During a scattering process photons can preserve their energy (elastic scattering such as Rayleigh or Mie scattering) or they can exchange energy with the medium (inelastic scattering). The energy exchange is made through phonons which are quanta of the vibrational modes of the material's crystal structure. This process was discovered by Sir Chandrasekhara Venkata Raman in 1928 [122]. The process and the spectroscopic technique are named after him. For this discovery he received a Nobel prize in physics in 1930. Nowadays Raman spectroscopy is a broadly used technique to characterise materials, from drugs to semiconductors.

A lot of information can be extracted from the energy difference between incident and scattered photon (phonon energy). As the oscillations of the lattice depend on crystal structure, atom's weight, their position in the unit cell and the nature of the interatomic bounding, the change of the scattered photon's energy can be used to characterise the material. Raman spectra are typically displayed as a function of wavenumber (cm^{-1}) as units to express the energy difference between the incident photons and the scattered ones. The wavelength of photons and the wave number can be linked easily:

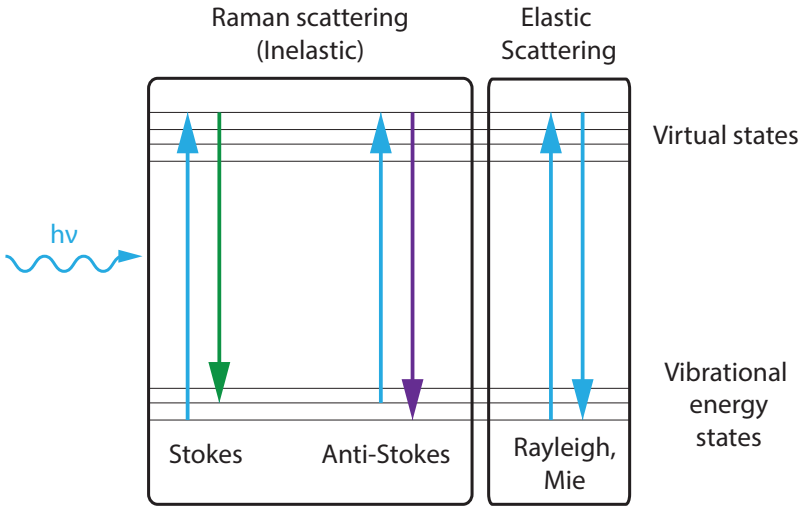


Figure 2.4: Elastic and inelastic scattering.

$$\Delta k = \left(\frac{1}{\lambda_0(\text{nm})} - \frac{1}{\lambda_i(\text{nm})}\right) \times 10^7 \frac{(\text{nm})}{(\text{cm})}, \tag{2.13}$$

where λ_0 is the wavelength of the incident light and λ_i is the wavelength of the scattered light. The origin of the shift in energy is explained in Fig. 2.4.

As Raman scattering provokes a shift in the energy of incoming photons, the narrower the spectrum of the incident light, the higher energy resolution we can achieve. Highly monochromatic laser sources are used to excite the media. Concerning the final energy of the scattered photon we can distinguish Stokes and anti-Stokes scattering. Photons that suffer Stokes scattering have less energy than the initial ones. Photons that suffer anti-Stokes scattering have more energy than the initial ones. Fig. 2.4 shows a schematic representation of both processes. Stokes and anti-Stokes spectra are symmetric with respect to the laser line and give the same information.

It has been reported that graphene [123], MoS_2 [40] and WS_2 [41] change their crystal lattice vibrations (and hence the Raman signal) as they are thinned. This makes Raman spectroscopy a really useful technique to characterise 2D flakes thickness.

The fact that Raman signals excited at or above resonance also contain a contribution from PL bears an additional advantage. As all TMDCs flakes contribute to the Raman signal but only monolayer TMDCs exhibit PL, the PL/Raman ratio can be used as a metric to estimate the monolayer volume fraction [118].

2.2 Femtosecond Pump-Probe Spectroscopy, Because Time Matters

All spectroscopic techniques described previously are not time-resolved. The development of ultrashort laser pulses opened the door to ultrafast spectroscopy. Ultrafast spectroscopy is a field of experimental physics that studies dynamic processes all the way down to the attosecond regime. Transient reflectivity, transmission or absorption in the visible, ultraviolet, infrared or terahertz range, time-resolved Raman spectroscopy, time-

resolved ARPES, X-ray and electron diffraction are just a few examples of the available spectroscopy techniques.

2.2.1 Introduction

Time-resolved spectroscopy is a study of dynamic processes in materials. The temporal resolution will be determined by the technology used. If it is based on electronics, the temporal resolution cannot be smaller than picoseconds. If we use optical methods, we can improve the resolution down to the femtosecond (fs) regime using visible light or even to attosecond (as) resolution if we work in the ultraviolet with spectrally broad pulses [124]. Moving to the UV spectral regime (high energy photons) wouldn't be the best choice to perform the experiments carried on in this work.

If we want to study a dynamic process, we should put our sample out of the equilibrium regime. For that, we use a fs laser pulse from a titanium sapphire laser (Ti:sapphire) with suitable photon energy. This pulse generates a population of excited states that slightly modify the light transmission. By tracking how that transmission changes with the delay between pump and probe pulses we can follow the dynamics of the photoexcited species.

In order to increase our accuracy/resolution we need to generate temporally well defined pump and probe pulses. Ti:sapphire pulsed laser technology is mature enough for generating pulses with a temporal length of tens of fs with a fixed repetition rate and constant output power.

2.2.2 Ultrashort pulses

There are many techniques to obtain short laser pulses; output switching, gain switching, Q switching, cavity dumping and mode locking.

Output switching is a normal continuous wave laser (CW) with a shutter in the cavity output that generates pulses of light. This technique is strongly limited in terms of output power and output pulse length.

A different approach is to have 100% reflective mirrors in our cavity and extract pulses by a switching mirror or an acusto-optic modulator. This technique is called cavity dumping [125].

Gain switching is achieved by using a pulsed pump source. The laser will only lase when the active medium (AM) is pumped until the population inversion regime. The pulse length in this technique is limited by the pump pulse length, the cavity length and by the AM response time.

Q switching was developed in 1961 in the same lab where the first laser was achieved [126]. It is based on a modulation of the laser intracavity losses. Losses modify the quality Q factor of the cavity and will determine if the cavity can lase. Losses are introduced by an element inside the laser cavity. This element will modulate the losses either by itself (passive Q switching) as a saturable absorber or triggered by an external signal (active Q switching) as opto-electronic or AOM. In both cases, the generation of the pulses follows the same sequence:

- *High losses in the cavity*: there is no stimulated emission inside the cavity. As there is no lasing, the AM does not lose pumped energy, population inversion becomes bigger (more energy stored in the AM).
- *Fast reduction of losses*: As losses of the cavity reduce, the Q factor of the cavity increases. A spontaneously emitted photon, coupled to the cavity, is amplified by the strongly pumped active medium.

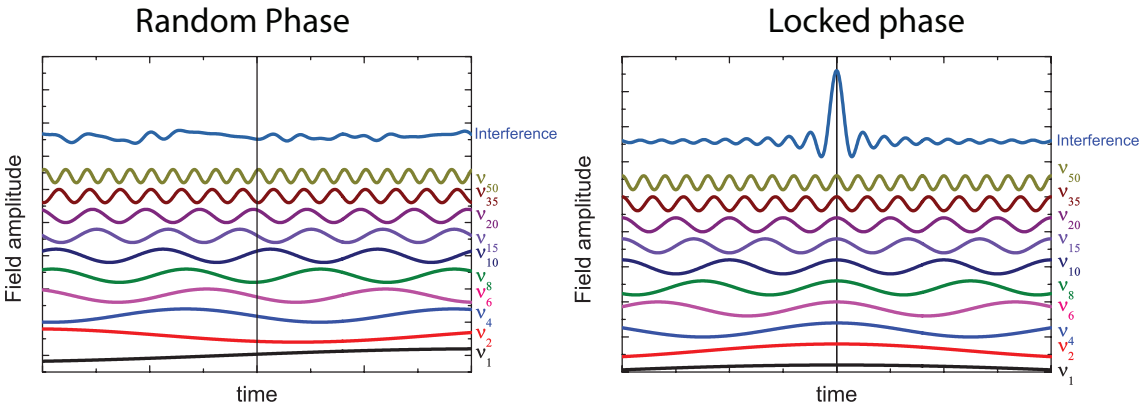


Figure 2.5: Field amplitude with a random phase between plane waves and with all the plane waves in phase (locked phase).

- *Gain saturation*: At a certain point the AM gain can not compensate the cavity losses and optical field gain saturation is reached. Then the cavity losses are increased again to repeat the process.

Pulses of nanosecond temporal length with high energy per pulse are typically obtained from Q switched lasers. This temporal resolution is typically used to study molecular dynamics in this range. However, for many electronic processes in semiconductors, these pulse lengths are not short enough. We need much shorter pulses to track electrons and excitons dynamics inside our material.

From the uncertainty principle of quantum mechanics $\Delta t \Delta E \geqslant \hbar/2 \Rightarrow \Delta t \Delta \omega \geqslant 1/2$. If we want a process well defined in time (an ultra short laser pulse), we need a broad spectrum. Ti:sapphire crystal can emit light in a broad range, from 650 nm until 1050 nm, which makes it a perfect candidate as AM for ultrashort laser pulses.

We can consider that each optical frequency is an independent wave confined inside a cavity. If all of these waves have an arbitrary phase, the intensity of light will be randomly distributed along the cavity in time and space and we will have what it is called continuous wave (CW) emission (Fig. 2.5), but if the phases of all of these plane waves are in phase we will have temporal packets of light (pulses). The second situation is called mode locking and the destructive and constructive interference between the cavity modes generates ultrashort pulses.

As the stored pump energy in the active media is finite, the time-averaged power in CW and in mode-locking situations will be similar, but as in the mode locking case we have the photons temporally confined, the peak power is much higher than in CW emission. This property is used to design the laser cavity for forcing mode locking.

The refractive index modification due to the Kerr effect scales linearly with the light intensity (Eq. 2.37). If we make two light beams, a pulsed one and a CW one, pass through a highly nonlinear crystal (sapphire Al_2O_3), the pulsed one will focus more strongly than the continuous one. If then we place an aperture that selectively cuts part of the spatially broader CW beam but does not cut the strongly focused pulsed laser beam, we will selectively introduce high losses in CW laser emission mode and CW lasing will no longer be possible, while losses for the pulsed laser are still low.

The aperture placed inside the cavity can be a real one, like a diaphragm. Another option is to do a fine alignment of the pump beam to selectively pump just the mode-

locking volume of the AM. That will provoke losses in the CW operation mode and lasing will not be possible.

The previous paragraphs describe a Ti:sapphire mode-locking oscillator. The technology these lasers are based on is completely mature. The AM is pumped by a neodimium laser doubled in frequency (532 nm). Oscillator output is a train of light pulses with high repetition rate (tens or hundred MHz) but relatively low energy per pulse. Pulse duration is around ~ 50 fs.

There are different parts of the pump-probe setup where nonlinear processes are needed. The energy per pulse must be increased and an amplification stage is placed after the oscillator. The most widespread technique to increase the energy per pulse is chirped pulse amplification (CPA) [127].

The basic idea behind CPA is that as we are working with femtosecond laser pulses, the peak power in each pulse is really high. It is really easy to reach the damage threshold of the amplifying crystal. If we increase the pulse length, we can decrease peak power and we can store higher energy per pulse without damaging the amplifying crystal. After amplification the pulse is compressed again. The result is a pulse with similar pulse length and at least 4 orders of magnitude more energy per pulse at a proportionally lower repetition rate.

2.2.3 Nonlinear optics

The development of the pulsed laser allowed scientists to research with high intensities of light and led to the development of nonlinear optics as a research field.

The classical theory of dispersion describes the electrons as point charges in harmonic oscillator potentials (Lorentz model). The harmonic potential and the response of electrons to an external monochromatic field are described by the equations[128]:

$$V(x) = V_0 + \left.\frac{dV}{dx}\right|_{x=0} x + \frac{1}{2}\left.\frac{d^2V}{dx^2}\right|_{x=0} x^2 \tag{2.14}$$

$$m\frac{d^2x}{dt^2} = -eEe^{-i\omega t} - m\gamma\frac{dx}{dt} - m\omega^2 x, \tag{2.15}$$

where x is the distance to potential minimum, ω is the frequency of the external field, γ is the damping term and for simplicity we have assumed that the minimum of the potential is at $x_0 = 0$. This expression can be solved as:

$$x = \frac{eE}{m}e^{-i\omega t}\frac{\omega^2 - \omega_0^2 - i\omega\gamma}{(\omega^2 - \omega_0^2)^2 + \omega^2\gamma^2}, \tag{2.16}$$

giving the solution for a single charge. The macroscopic response of the medium will be described by:

$$P = -eNx \tag{2.17}$$

$$P = \frac{e^2N}{m}\frac{\omega^2 - \omega_0^2 - i\omega\gamma}{(\omega^2 - \omega_0^2)^2 + \omega^2\gamma^2}Ee^{-i\omega t}, \tag{2.18}$$

where N is the number of electrons, P is the polarization, the medium's answer to the electric field. If we define susceptibility (χ) as:

$$\chi = \frac{e^2N}{m\epsilon_0}\frac{\omega^2 - \omega_0^2 - i\omega\gamma}{(\omega^2 - \omega_0^2)^2 + \omega^2\gamma^2}, \tag{2.19}$$

we obtain a linear optical response of the material's electrons (in amplitude and frequency).

$$P = \epsilon_0 \chi E \tag{2.20}$$

We have assumed that the electric field depends exclusively on the macroscopic (external) electric field. Generally this is not true and the Lorentz field (local field corrections) should be added (This correction can be checked at [128]).

This theory nicely describes many light–matter interaction phenomena, but certain effects, such as generation of new frequencies, solitonic propagation, self focusing and others cannot be explained with linear behaviour. These effects appear when a more intense electric field interacts with media. If the electrons move further from the equilibrium position, the potential they feel is no longer harmonic. We should add more terms to Eq. 2.14:

$$V(x) = V_0 + \left.\frac{dV}{dx}\right|_{x=0} x + \frac{1}{2}\left.\frac{d^2V}{dx^2}\right|_{x=0} x^2 + \frac{1}{6}\left.\frac{d^3V}{dx^3}\right|_{x=0} x^3 + ... \tag{2.21}$$

With a monochromatic external field we obtain an anharmonic differential equation:

$$F_{\text{ext}} = -e\left[E_\omega e^{-i\omega t} + E_\omega^* e^{i\omega t}\right] \tag{2.22}$$

$$m\frac{d^2x}{dt^2} = E_{\text{ext}} - m\gamma\frac{dx}{dt} - m\omega^2 x - mA_2x^2 + ... \tag{2.23}$$

Equation 2.23 cannot be solved analytically, but if we search for a solution in a perturbative series, we can obtain the susceptibility as a contribution of many terms of different orders. The first term will reproduce the linear behaviour described previously, the second term will reproduce second order processes, third term will determine the third order processes and so on. a nonlinear solution in x leads to a nonlinear polarization in the medium.

It is possible to see that the non–linear polarization inside a material can generate an electric field at frequencies 2ω starting from an electric field of frequency ω. The intensity of the light at 2ω will depend on the process efficiency, given by tue second order susceptibility ($\chi^{(2)}$) and the self-interference of the generated light, given by the phase matching between the fundamental and the doubled frequency. That leads to the definition of a coherence length for which the intensity of the second harmonic field is maximum (Fig. 2.6). SHG crystal thickness is chosen according to the coherence length (L_C). The total intensity conversion efficiency of the process is given by:

$$e_{\text{SHG}} \propto L^2 \,\text{sinc}\left(\frac{\Delta kL}{2}\right)^2 \tag{2.24}$$

$$L_C = \frac{\pi}{|\,\delta k\,|} \tag{2.25}$$

If the incident light is composed of more than one frequency, more nonlinear effects can be observed such us parametric oscillation, sum frequency generation, difference frequency generation and optical rectification.

Second-order optical effects allow us to change the frequency of our light but they give spectrally narrow distribution of frequencies (consequence of the starting narrow laser spectral line). In our experiments we are interested in spectrally broad probe pulses

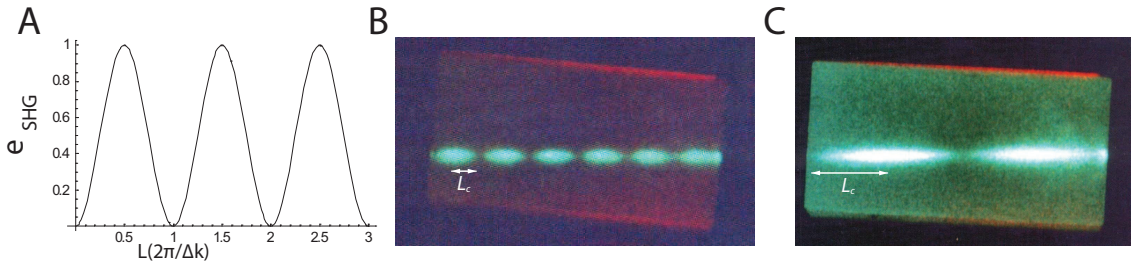


Figure 2.6: (A) Efficiency of second harmonig generation (SHG) as a function of the crystal thickness. (B) and (C) Constructive and destructive self-interference of the doubled frequency as a function of propagation length (L). It can be observed how the coherence length (LC) changes between (B) and (C), a direct consequence of different phase matching conditions [129].

.

because that will allow us to simultaneously study different transitions. Supercontinuum (SUC) generation allows us to obtain pulses with broad spectra. SUC was first reported in 1970 [130].

SUC generation is a more complex phenomenon that involves many nonlinear optical processes like self-phase modulation (SPM), cross-phase modulation, Kerr effect, ionization, four-wave mixing and stimulated Raman scattering among others. Even when it is not completely clear which is the exact weight of each of these processes in the generation of a SUC pulse, there is the agreement that the main contribution to the SUC comes from a combination of Kerr effect, ionization and SPM.

SPM refers to the phenomena where an intense laser beam propagates through a medium. The high electric field of the laser beam is capable of inducing an appreciable intensity dependent variation in the refractive index of the material. This variation of the refractive index induces at the same time a phase change in the incoming light wave, leading to a self phase modulation of the light's electric field. SPM appears in two ways, spatial SPM and temporal SPM.

The simplest way to explain SPM is, if we describe the propagation of a laser pulse through an isotropic medium with the equation of a plane wave and we isolate the third order of the medium polarization.

$$\left(\frac{\partial^2}{\partial z^2} - \frac{n_0^2}{c^2}\frac{\partial^2}{\partial t^2}\right)E = \frac{4\pi}{c^2}\frac{\partial^2}{\partial t^2}P^{(3)} \tag{2.26}$$

where:

$$E = \xi(z,t)e^{(ik_0 z - i\omega_0 t)} \tag{2.27}$$

$$P^{(3)} = \chi^{(3)}|E|^2 E \tag{2.28}$$

If we assume that the envelope of the pulse ($\xi(z,t)$) varies on a length scale much longer than the carrier wavelength (slowly varying amplitude approximation), we can neglect $\partial^2\xi/\partial z^2$ on the left side of Eq. 2.26. On the right term we will just keep $(4\pi\omega_0^2)\chi^{(3)}|\xi|^2\xi$. Following these approximations we can reach the expressions:

$$|\xi| = |\xi(t)| \tag{2.29}$$

$$\phi = \phi_0 + \frac{2\pi\omega_0^2}{ck_0}\chi^{(3)}|\xi(t)|^2 z, \tag{2.30}$$

where Eq. 2.29 is telling us that there is no modification in the temporal profile of the pulse during propagation (propagation without dispersion). Eq. 2.30 means that the phase of the pulse changes while it propagates from 0 to z because of an induced change in the refractive index.

$$\Delta n = (2\pi/n_0)\chi^{(3)}|\xi|^2 \tag{2.31}$$

$$\Delta\phi(t) = \frac{\omega}{c}\int_0^z \Delta n dz \tag{2.32}$$

A pulse's instantaneous frequency is given by Eq. 2.33. A modulation of the phase will lead to a frequency modulation, which brings a spectral broadening that can be calculated from the Fourier transform Eq. 2.34.

$$\Delta\omega = -\frac{\partial\Delta\phi}{\partial t} = -\frac{2\pi\omega_0^2}{c^2k_0}\chi^{(3)}\frac{\partial|\xi|^2}{\partial t}z \tag{2.33}$$

$$|E(\omega)|^2 = \left|\frac{1}{2\pi}\int_{-\infty}^{+\infty}\xi(t)e^{-i\omega_0 t+i\omega t}dt\right|^2 \tag{2.34}$$

Due to the finite section of the laser beam and because of its spatial Gaussian-like profile variation, Δn (Eq. 2.31) follows a similar shape as the spatial beam profile, and leads to the well known self-focusing (Kerr effect, spatial SPM). The Kerr effect is a third-order nonlinear effect, which causes the refractive index of a material not to depend only on the material, but also on the light intensity through it.

$$n = n_0 + n_2 I \tag{2.35}$$

As laser beams have a Gaussian distribution of intensities (higher intensities in the center of the beam that are reduced as we move away), the refractive index of the material is different for different distances to the center. The laser intensity has a radial dependence that induces a radial dependence in the refractive index.

$$I(r) = I_0 e^{-\frac{r^2}{r_0^2}} \tag{2.36}$$

$$n(r) = n_0 + n_2 I_0 e^{-\frac{r^2}{r_0^2}} \tag{2.37}$$

It is a direct conclusion from Fermat's principle that the light moving through a medium with a gradient of refractive index moves towards higher refractive index values. As the higher intensities of the beam shape are present in the center of the beam, so will be the higher refractive index values. Our beam will go through a process of auto-focusing, known as self-focusing. n_2 can be measured by the Z-scan technique (see Subsection 1.2.7). As an orientative value, n_2 of air is 5×10^{-19} cm^2/W. For a modulation of 10% of the refractive index of the air we need intensities as high as 2×10^{17} W/cm^2

(luckily for researchers in experimental optics there are materials with higher nonlinear refractive index values, like sapphire $n_2 \sim 3\times10^{-16}$ cm^2/W or monolayer WS_2 $n_2 \sim 10^{-10}$ cm^2/W [131]).

By focusing the laser beam the intensity rises. At a certain point its value is so high that the propagation medium (typically air) is ionized. That provokes a divergence in the beam stronger than self-focusing. Once the beam has diverged enough, the propagation media is not ionized any more, but the light intensity is high enough for provoking self-focusing again. These processes can concatenate through long distances and provoke what is known as filamentation.

The theory of spectral broadening is in the simplest case as described, but normally SPM occurs simultaneously with the Kerr effect, or Kerr effect is the origin of the high light intensities that lead to SPM. The Kerr effect drastically modifies light intensity, which will strongly influence SPM. Simulations that predict SPM and Kerr effect need to solve a time-dependent tri-dimensional wave equation. As self-focusing rapidly modifies the pulse temporally and spatially, the solution of this wave equation is challenging and requires many resources.

Besides the calculation problems, SPM and Kerr effect are useful tools in experimental optics and are used to broaden our laser pulses, initially centered at 830 nm with a spectral full width half maximum (FWHM) of 30 nm to laser pulses with a spectrum from 460 nm until 760 nm and a second wing of similar width on the low-energy side of 830 nm.

2.2.4 Pump-probe time-resolved spectroscopy

Pump-probe is a powerful technique that allows us to study and characterise the photoexcited states dynamics. A first pulse, the pump, arrives to our material and is absorbed. As we are working with semiconductors, in order to have photoexcited states the photons that compose the pump pulse must have at least the energy of the bandgap. A second, spectrally broad and low power pulse is sent to the sample at a well defined delay (τ), Fig. 2.7.

By comparing the transmitted light of this second pulse, with(T_{on} and without(T_{off}) the presence of the pump, it is possible to identify the pump-induced response of the material. If we scan the delay between pump and probe pulses (τ), it is possible to track the population dynamics of photoexcited states.

The pump-probe signal is given by the expression:

$$\frac{\Delta T}{T} = \frac{T_{\text{on}} - T_{\text{off}}}{T_{\text{off}}} \tag{2.38}$$

The pump beam is chopped. T_{on} is the probe transmission when the pump is present, and T_{off} is the probe transmission when the pump is blocked. $T_{\text{on}} - T_{\text{off}}$ is the change in transmission induced by the population of photoexcited states. This difference is normalized by T_{off} in order to have a value that is independent of the probe power.

Introducing in Eq. 2.5:

$$T = I_0 e^{-\alpha(\omega)d} \tag{2.39}$$

It can be easily shown that for $\Delta T/T \lll 1$:

$$\frac{\Delta T}{T} \approx -\Delta\alpha(\omega)d \tag{2.40}$$

We can consider the absorption coefficient of a transition between the states i and j for the frequency ω as:

$$\alpha_{i,j}(\omega) = \sigma_{i,j}(\omega)(N_i - N_j) \tag{2.41}$$

Where $\sigma_{i,j}(\omega)$ is the cross section (cm^2), which has information about the dipole moment of the transition and the line shape. N_i and N_j are respectively the populations of levels i and j. Expression 2.41 can be extended to several levels:

$$\alpha = \sum_i \left(\sum_j \sigma_{i,j}(\omega) \Delta N_{i,j} \right) \tag{2.42}$$

The pump pulse will induce a change in the absorption coefficient, which is originated in a change of the populations or in a change in the absorption cross section. This variation are observed by the changes in the probe pulse transmission and depend on the delay between pump and probe pulses (τ):

$$\frac{\Delta T}{T} = -\sum_{i,j} \Big(\sigma_{i,j}(\omega) \Delta N_j(\tau) + N_j \Delta \sigma_{i,j}(\omega, \tau) \Big) d \tag{2.43}$$

Considering that only transitions between dipole-coupled states have a non-negligible $\sigma_{i,j}(\omega)$, and that our interest will be restricted to a certain range of ω, only few transitions will have to be considered for this calculation.

The first term of Eq. 2.43 represents the changes in the signal due to changes in populations (ΔN). The second term represents changes in absorption cross section ($\Delta \sigma_{i,j}$) due to photoexcitation. Many effects, such as band gap renormalization [111], Burstein-Moss effect [132] or Stark effect [133], can provoke such changes. These processes are population dependent, so we assume the temporal dynamic of $\sigma(\omega, \tau)$ will have a similar time evolution as the photoexcited states populations. In our research we assume that the contribution of this second term is either negligible or is tangled with the first term and hence indistinguishable.

We can describe the pump-probe signal with three basic processes. When the pump pulse arrives to the material it will excite a certain amount of electrons from the ground

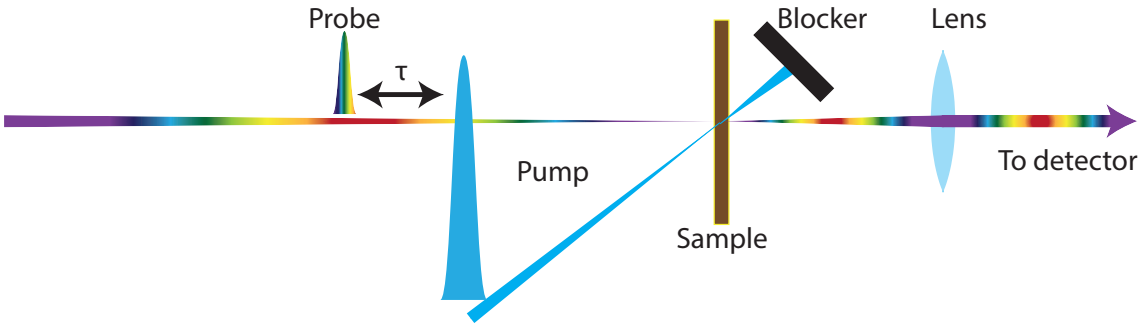


Figure 2.7: Schematic representation of how pump and probe pulses arrive to the sample.

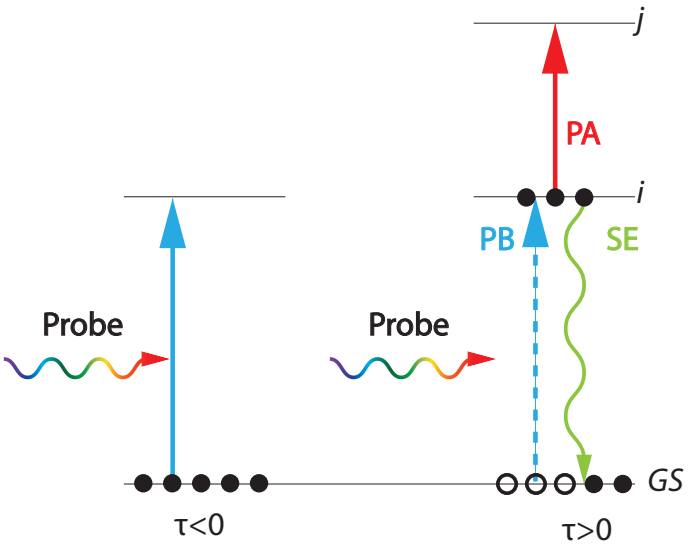


Figure 2.8: Schematic representation of the origin of the pump-probe signal. For negative delays probe is absorbed by the medium. For positive delays (pump pulse arrives before) the probe interacts with the photoexcited states' population and it can suffer photobleaching, photoinduced absorption or stimulated emission.

state to the i energy level. When the probe pulse arrives to the material we can observe the following processes:

- If the probe pulse is resonant with the $i \rightarrow j$ transition with $i \neq GS$ and $i < j$ ($E_i < E_j$), the material will absorb more probe photons compared with the not pumped material. This phenomenon will increase absorption (negative $\frac{\Delta T}{T}$ signals) and is called **photoinduced absorption (PA)**.
- If the probe pulse is resonant with the transition $i \rightarrow j$, with $i = GS$(ground state), it will find less electrons in the ground state when the material has been pumped. A positive $\frac{\Delta T}{T}$ signal is generated, and this phenomenon is called **photobleaching (PB)**.
- If the lowest excited state is dipole coupled with the ground state and the probe pulse is resonant with the $1 \rightarrow 0$ transition, new coherent photons are generated by **stimulated emission (SE).** This effect causes a positive $\frac{\Delta T}{T}$ signal.

With these three effects we can roughly explain the $\Delta T/T$ signal. By scanning the delay between pump and probe pulses, the photoexcited states dynamics are obtained.

2.2.5 Experimental setup

A Ti:sapphire oscillator is used to generate our starting train of pulses pulses. The oscillators output is a train of pulses with high repetition rate and low energy per pulse. As chirped pulse amplification stage is place afterwards. The output of the amplification stage is guided until the pump probe setup.

Fig. 2.9 shows our pump-probe experimental setup. The starting laser beam consist of a train of pulses with 1 kHz repetition rate and $\sim 100 - 150$ fs of full width half maximum (FWHM) with a central wavelength of 800 nm and an energy per pulse of 200 μJ

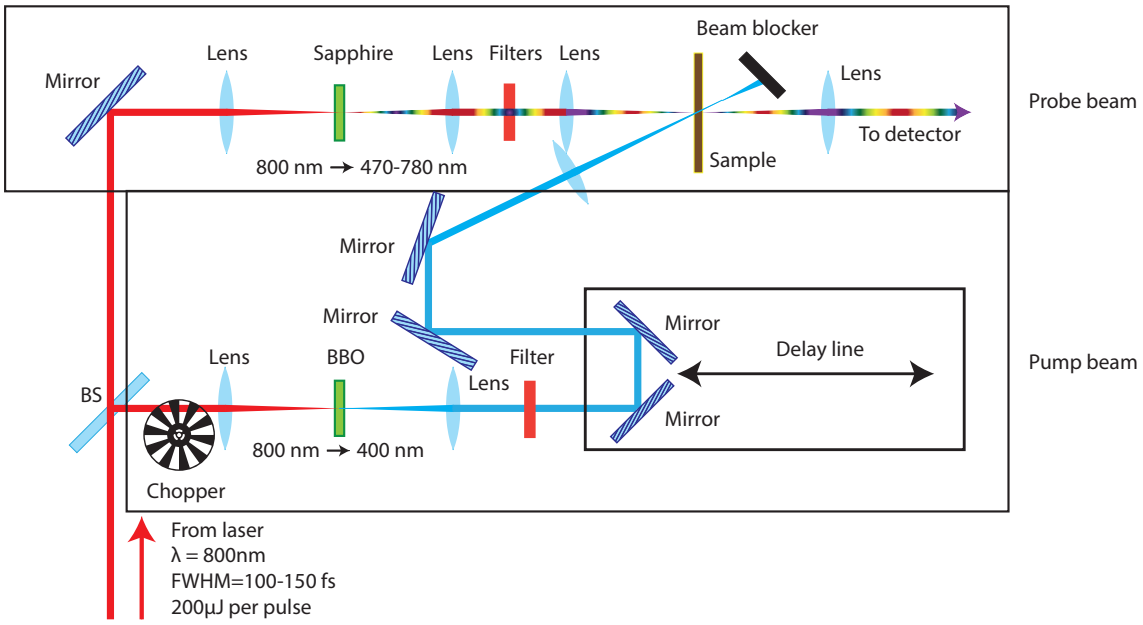


Figure 2.9: Schematic representation of our pump-probe setup.

.

is the starting laser beam. The beam is split between pump and probe beams. The probe beam is focused in a nonlinear crystal (either sapphire or calcium fluoride) and a white light SUC is generated. Some filters are added in the beam path to remove the fundamental frequency and to reduce the energy per pulse. The probe beam is focused on the sample ($\sim 150\ \mu$m diameter), afterwards the beam is collimated and sent to the detector. The pump beam is chopped at 500 Hz and focused on a barium borate crystal (BaB_2O_4, generally known as BBO), where the laser frequency is doubled. The pump beam is collimated and some filters are added to remove the residual fundamental frequency. The setup's delay line is placed immediately afterwards to control the delay between pump and probe pulses. Then, pump beam is overlapped with the probe on the sample.

After pump-probe interaction in the sample, the pump beam is blocked and the probe beam is sent to the detector. Chopper, detector and delay line are synchronized and $\Delta T/T$ signal is recorded.

2.3 Liquid Phase Exfoliation

There are many techniques that allow us to produce TMDCs in mono- and few-layer form. We can roughly divide them into bottom-up and top-down processes.

Bottom-up techniques, such as chemical vapour deposition (CVD), requires furnaces where the ambient conditions are carefully controlled. The chosen substrate is placed on a heater that heats it to the required temperature (normally few hundred degrees). Then there is a flow of precursor materials, typically oxides, such as MoO_3 for molybdenum and sodium dodecyl benzene sulphonate for the sulphur (in the particular case of MoS_2 growth). Then by controlling the temperature of the substrate, flow of precursor, pressure in the chamber and baking time it is possible to control how the material grows (thickness, lateral size of the flakes, continuous film). Even though the use of CVD

allows the growth of continuous films of monolayer TMDCs, it was not yet possible to obtain the large areas needed for industrial applications. However, as it has happened with graphene, industrial growth of monolayers is expected.

Top-down techniques obtain the flakes by cleaving a bulk TMDC crystal. Mechanical cleaving (Scotch tape technique) was the first technique used to obtain graphene monolayers [14] and it has also been used for all the 2D materials coming after it. It produces flakes with lateral sizes of hundred microns in the best cases. This is enough to build state of the art devices for research purposes, but lacks the potential to scale its production.

CVD is the ideal technique if large area high quality monolayer film is needed. But there are a bunch of applications where these properties are not needed. For these applications liquid phase exfoliation (LPE) arises as a fast and cheaper alternative for material production.

As important as exfoliating the material is to keep it stable in dispersion without reaggregation. In the following, I will summarize dispersion theory based on Hansen parameters as well as polymer stabilization.

2.3.1 Stabilization

Generating a dispersion of TMDCs flakes needs to overcome two hurdles; (i) exfoliate the material from bulk and (ii) generate the conditions to have a stable dispersion. A good exfoliation is completely useless if the flakes reaggregate afterwards. This subsection is focused on the physics of dispersions and which parameters will determine their stability.

A first rule of thumb approach to the solubility theory is *like dissolves like*. Materials with similar solubility parameters will dissolve in each other while materials with different solubility parameters will not produce stable dispersions.

The first to realize that the solubility could be described by parameters were Hildebrand and Scott. Hildebrand defined his parameter as the square root of the cohesive energy density [134]:

$$\delta = \sqrt{E/V}, \tag{2.44}$$

where E is the energy of vaporization and V is the molar volume of the pure solvent. By mixing two different chemical compounds a change in the system entropy (S) and enthalpy (H) occurs. The mix will be stable only if the Gibbs free energy is negative:

$$\Delta G^M = \Delta H^M - \Delta S^M T \tag{2.45}$$

where ΔH^M is the enthalppy of mixing (heat of mixing), ΔS^M is the change in entropy and T is the absolute temperature. A typical strategy to obtain stable dispersions is to have large ΔS^M and hence negative G^M. However from previous experience with carbon nanotubes (CNT) [135], [136] ΔS^M is small due to their large size and relative rigidity. This can be extended to TMDCs flakes [137]. Hence we can not rely on the term ΔS^M to keep ΔG^M negative. ΔH^M must be kept as small as possible. ΔH^M can be expressed as [134]:

$$\Delta H^M = \varphi_1 \varphi_2 V_M (\delta_1 - \delta_2)^2, \tag{2.46}$$

where φ_i is the volume fraction of a component of the mix, V_M is the total volume and δ_i is the Hildebrand solubility parameter of a component of the mix. A straightforward

conclusion of Eq. 2.46) is that minimising the difference between Hildebrand solubility parameters reduces the enthalpy of mixing. There is an alternative expression for Eq. 2.46 broadly used in polymer science. It gives the enthalpy of mixing per unit volume.

$$\frac{\Delta H^M}{V_M} = \frac{\chi \varphi_1 \varphi_2 \kappa_B T}{\upsilon_0}, \tag{2.47}$$

where κ_B is the Boltzmann constant, T is the temperature, υ_0 is the molecular volume of the solvent, χ is the Flory-Huggins parameter (that can be approximated as a function of Hildebrand solubility parameters):

$$\chi \approx \frac{\upsilon_0}{\kappa_B T}(\delta_1 - \delta_2)^2 \tag{2.48}$$

Which reminds us that the best way to obtain ΔG^M zero or negative is to minimise H^M ergo to match Hildebrand solubility parameters. Eq. 2.48 works nicely for those mixes without polar interactions, this somehow limits the applicability of this theory. Charles M. Hansen extended the Hildebrand solubility theory taking into account three interactions:

- *Non-polar interactions* (E_D) come from atomic interaction. Its elemental nature makes this attractive force present in all kinds of mixes.
- *Permanent dipole* is related to the polar cohesive energy (E_P). This parameter is calculated from the molecular dipole moment and can be experimentally verified.
- *Hydrogen bonding* (E_H). It is an electron exchange parameter. This parameter represents the attraction between particles due to hydrogen bondings.

By considering just these three kinds of interactions we might not end up with a completely accurate theory, but we can have a good enough prediction of dispersibility without raising the number of parameters. The Hildebrand solubility parameter is related to the Hansen solubility parameters (HSP) by assuming that the sum of all the cohesive energies is equal to the total cohesive energy.

$$E = E_D + E_P + E_H \tag{2.49}$$
$$E/V = E_D/V + E_P/V + E_H//V \tag{2.50}$$
$$\delta^2 = \delta_D^2 + \Delta_P^2 + \delta_H^2 \tag{2.51}$$

We can obtain an equivalent expression to Eq. 2.48 with HSP:

$$\chi \approx \frac{\upsilon_0}{\kappa_B T}\left((\delta_{D,1} - \delta_{D,2})^2 + (\delta_{P,1} - \delta_{P,2})^2 + (\delta_{H,1} - \delta_{H,2})^2\right) \tag{2.52}$$

The HSPs have been accepted by the scientific community and they have been obtained for a broad set of solvents. A particular study of solubility parameters was done by J. M. Hughes [138]. Solubility expressions were adapted, as a function of their dimensions, to typical nanomaterial shapes as nanotubes and 2D platelets (D=2,1 for platelets and nanotubes, respectively) and a term describing permanent dipole-induced dipole term (cross term of Eq. 2.53):

$$\begin{aligned}\left(\frac{\Delta H^M}{V_M}\right)_d = &\left(1 - \frac{d}{3}\right)\varphi_1 \varphi_2 \Big((\delta_{D,1} - \delta_{D,2})^2 + \\ &+(\delta_{P,1} - \delta_{P,2})^2 + 2A(\delta_{D,1} - \delta_{D,2}) \times (\delta_{P,1} - \delta_{P,2})\Big)\end{aligned} \tag{2.53}$$

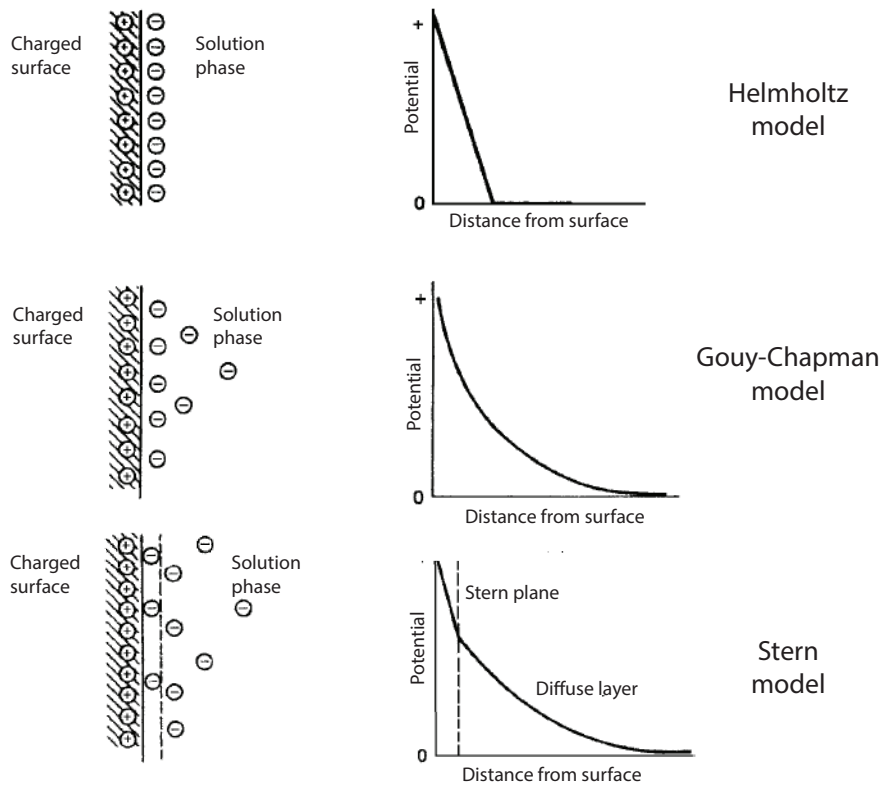


Figure 2.10: Counterion distribution in the vicinity of the interface and evolution of electric potential with distance from the charged surface for Helmholtz, Gouy-Chapman and Stern model [142].

.

Surfactant stabilization

When HSP of solvent and solute do not match, it is common to add an extra kind of particles, called surfactant, that will help with the dispersion stabilization. Because of the high surface tension of TMDCs ($\sim$ 280 mJ/m^2 in MoS_2 [139]) it is difficult to have a stable disperson without avoiding flocculation by adding a surfactant [140].

Surfactants have two regions perfectly defined (amphiphilic) in their chain shape [141]. One of these regions is oil-soluble (lipophilic, oleophilic or hydrophobic), while the other region is water-soluble (hydrophilic). Due to this dual behaviour surfactants tend to generate certain structures in dispersions in order to reduce their energy.

Adsorption at interfaces is one of the fundamental properties of surfactants. When dispersed in water, the hydrophilic region faces the solvent while the hydrophobic part tends to avoid the solvent. This disposition uses to be achieved in interfaces, like solvent-solvent, or solvent-flake. At a solvent-solvent surface (like water-air) surfactant particles are aligned in the interface with the hydrophobic region facing the air. If we have a solvent-flake interface, surfactant particles will tend to attach to the flake and the hydrophobic region will face the flake surface.

There is a range of surfactant concentrations for which there is no need for an interface to generate structures. For surfactant concentrations equal or higher to the so-called

critical micellization concentration (c.m.c.) surfactant particles aggregate in micelles. A micelle is a structure formed by many surfactant particles where their hydrophobic regions associate together and generate volumes where the solvent of the dispersion is not present.

One of the surfactants more used in MoS_2 exfoliation and stabilization is sodium cholate ($C_24H_39NaO_5$, also knwon as SC). SC is adsorbed at the MoS_2-water interface and generates what is called an electrical double layer; an unequal distribution of charges is always present at any interface. This unequal distribution of charges results in a net charge generated at one side of the interface, while at the other side of the interface an equal net charge of opposite sign is generated.

As there is a charge distribution there is an associated potential, and a region where the major portion of the electrical interactions occur. The thickness of this region is called *Debye length*.

$$\frac{1}{\kappa} = \left(\frac{\epsilon_r \epsilon_0 RT}{4\pi F^2 \sum_i C_i Z_i^2} \right)^{\frac{1}{2}}, \tag{2.54}$$

where ϵ_r, ϵ_0 are the relative and vacuum dielectric constant, R is the gas constant, T is the absolute temperature, F is the Faraday constant, C_i is the molar concentration of any ion in the solution phase and Z is the valence of the ions. Electrical interactions inside the *Debye length* has been studied by many authors. Helmholtz considered a uniform and narrow distribution of charges of opposite sign at both sides of the interface, which produces a fast drop of the potential. This "parallel plate condenser model" did not consider that thermal agitation tends to move some of these ions. Gouy and Chapman considered the contribution of diffused ions obtaining a potential that falls more softly. The accepted model is a mix of these two. It was proposed by Stern, who divided the solution in two regions and assumed a different distribution of ions in each. The first region has a uniform charge density and is strongly bound to the surface counterions. The second region has a diffuse layer of counterions (Fig. 2.10).

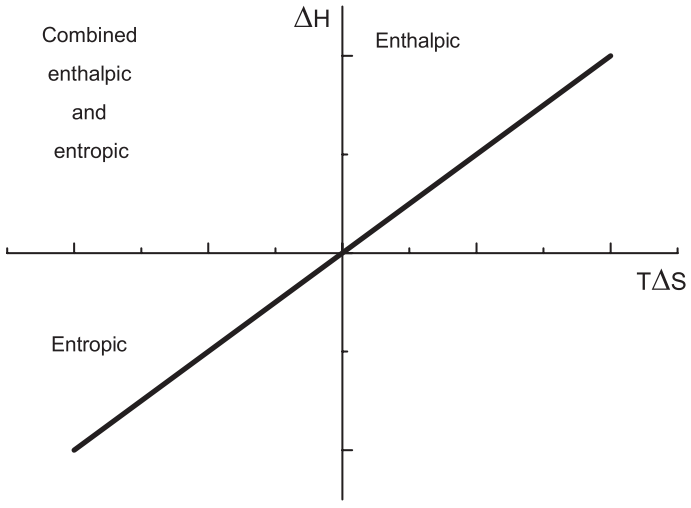


Figure 2.11: Representation of the steric stabilization on an entropy-enthalpy diagram.

Polymer stabilization

If polymers are adsorbed on the flake surface, they can act as surfactants and avoid reaggregation of flakes after exfoliation. Stabilization of 2D flakes dispersion using polymers follows different rules than surfactant stabilization. Any lyophobic particle in a solvent/polymer dispersion will have (partially) covered its surface by polymer chains. When two of these particles approach each other, they will suffer repulsion due to the interaction of the polymer chains on its surface. As these two particles approach each other the chain-chain interaction becomes dominant over the chain solvent interaction. As the polymer chains are lyophilic, that leads to a rise in the free energy of mixing (Eq. 2.45), which generates a repulsive force and keeps the dispersion stable. This effect is called steric stabilization.

Steric stabilization is broadly used because it is non-sensitive to electrolyte concentration, it works in aqueous and non-aqueous media and it exhibits good freeze-thaw stability [141]. It is easier to illustrate the polymer stabilization if we use the osmotic pressure of the polymer (Π)

$$\frac{\Pi}{c} = \frac{RT}{< M_n >} \tag{2.55}$$

where c is the polymer concentration (kg/m^3) and $< M_n >$ is the number average molecular weight. The polymer chain-chain interaction can be positive (attractive chain-chain interaction) or negative (repulsive chain-chain interaction). If attraction and repulsion forces are balanced, our dispersion is in the so-called θ-point and the dispersion will be stable. The stability of the dispersion can be compromised by increasing the pressure, adding to the dispersion a miscible non-solvent for the stabilizing moieties or by modifying the temperature, which leads to a critical flocculation pressure, volume and temperature. The origin of the temperature dependence is shown in Fig. 2.11 and can be used to classify the stability of a dispersion.

Until now, we have considered how the adsorbed polymer chains influence the stability of the dispersion, but non-adsorbing polymer chains also play an important role in the stabilization of a dispersion. Depletion interactions are the effects of the non-adsorbing polymer chains. Depletion interactions are strongly dependent on the polymer concentration and can lead to different stabilization regimes summarized in Fig. 2.12.

- For low polymer concentration dispersed flakes compete to adsorb polymer chains on their surface. Several flakes can adsorb the same polymer chain and lead to bridging flocculation.

- For higher polymer concentration exfoliated flakes are uniformly covered by polymer chains and the dispersion is in the steric stabilization regime.

- If the polymer concentration is increased until we reach the regime where dispersed particles approach distances comparable to the size of the dissolved polymer chains, those chains will move away from the gaps. The volume between dispersed particles will be filled just with solvent particles. This generates an osmotic pressure that sucks the solvent out of this volume provoking a flocculation named depletion flocculation.

- At even higher concentrations of polymer a similar effect can be observed. In this case the particles are slightly more separated than in the previous one. Forcing dispersed flakes together in this situation can be done only by demixing polymer

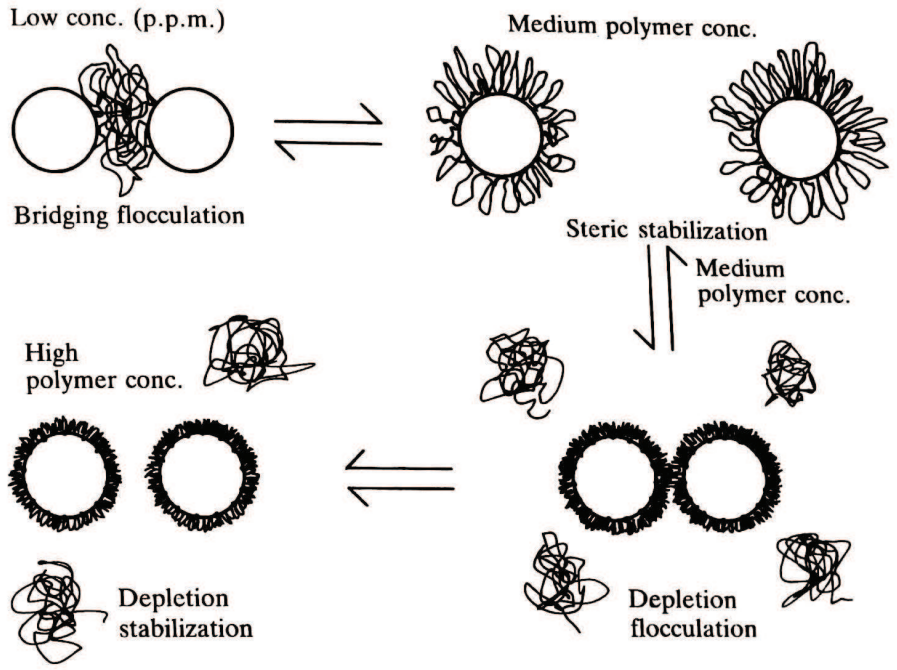


Figure 2.12: Dispersed polymer concentration influence on 2D flakes' dispersion stability as a function of its concentration [141].

chains from the solvent. If we are working with a good solvent-polymer combination, that will increase the free energy of the system. This leads to a repulsive interaction. This situation is called depletion interaction.

As described in this subsection the effects of a polymer in a dispersion can be completely different. A polymer can lead to the stability or the flocculation of a dispersion as a function of its concentration, molecular weight or liophobicity. Polymer stabilization of dispersions can be tricky and a systematic study of those parameters must be done in order to obtain the right polymer chain length and concentration.

2.3.2 Exfoliation

Exfoliation refers to the peeling of the different layers of a material. Many exfoliation methods have been explained in the introduction of the thesis. My research has been mostly focussed on exfoliation of TMDCs with a sonic tip. I am aware that the term LPE refers to a set of techniques that exfoliate material in liquid media, in any case I will use the term LPE to refer to the exfoliation through ultrasound in liquid media.

LPE is a simple, cheap and scalable technique for the production of 2D materials. The LPE process is described in Fig. 2.13. Starting from bulk TMDCs powder mixed with the proper solvent it is possible to exfoliate it by applying ultrasound. A sonic tip is introduced in the beaker where our starting dispersion of water, SC and bulk material is present. The sonic tip emits ultrasound centered at 20 kHz with a power of 750 W. The ultrasound is reflected by the walls of the beaker and generates points of maximum and minimum intensity. At certain places of our dispersion cavitation bubbles will self generate. These bubbles will implode, generating a shock wave in the solvent. This shock wave produces a movement in the solvent and when solvent molecules move in

the vicinity of a static TMDC bulk crystal a shear force is applied. This shear force is responsible for peeling off the external layers of a bulk crystal.

By controlling ultrasound power, sonication time and starting concentration of surfactant and TMDCs it is possible to obtain a stable dispersion of exfoliated TMDCs flakes.

The dispersion after exfoliation is called *stock dispersion*. Stock dispersion contains a broad distribution of flakes in terms of lateral size and thickness. For most purposes size and thickness selection of exfoliated flakes must be done.

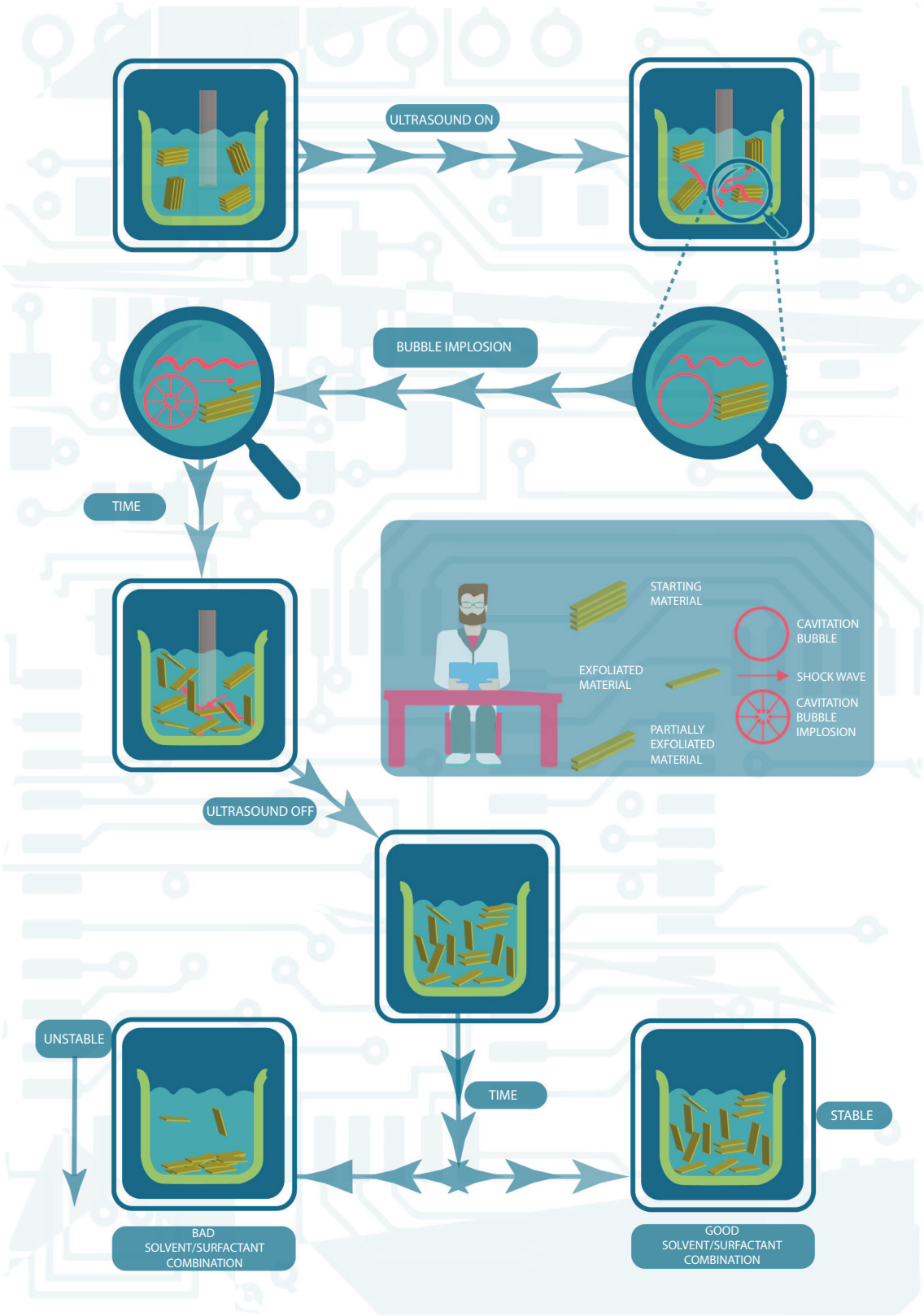


Figure 2.13: Sonication process and the importance of matching solubility parameters in the dispersion.

2.3.3 Flake selection via centrifugation

Stock dispersions have a broad distribution of flakes (in terms of thickness and length), from monolayer to almost non-exfoliated material. These last flakes will sediment by themselves over time. Stock dispersions are used to be left unshaken over night and sedimented/unstable material is separated from the stable flakes dispersed in the supernatant. A finer selection of flakes in terms of lateral size and thickness can be done following certain centrifugation protocols.

The effective mass of a particle immersed in a fluid can be obtained using the buoyancy of the medium as $m_{eff} = bm$, where m is the mass of the particle and:

$$b = 1 - \rho V_s, \tag{2.56}$$

where ρ is the solvent density and V_s is the partial specific volume of the solute, then, ρV_s is the mass of solvent displaced per gram of solute. There are two main forces acting over a particle in suspension; gravitational(F_g) and frictional (F_c) force [143]:

$$F_g = m_{eff} g \tag{2.57}$$
$$F_f = -v_s f \tag{2.58}$$
$$F_T = m_{eff} g - v_s f, \tag{2.59}$$

frictional force is proportional to the speed of the particle. After a transitory period the particle will move at a drift speed, a constant speed, when the total force (F_T) is zero:

$$0 = F_T = m_{eff} g - v_s f \tag{2.60}$$

The drift speed of the particle in the medium can be expressed as:

$$v_s = \frac{m_{eff} g}{f} \tag{2.61}$$

Sedimentation speed is proportional to the mass of the particle. Hence sedimentation can be used to separate flakes attending to their masses. Sedimentation speeds due to gravitational forces are rather small, hence it is convenient to sediment the dispersed

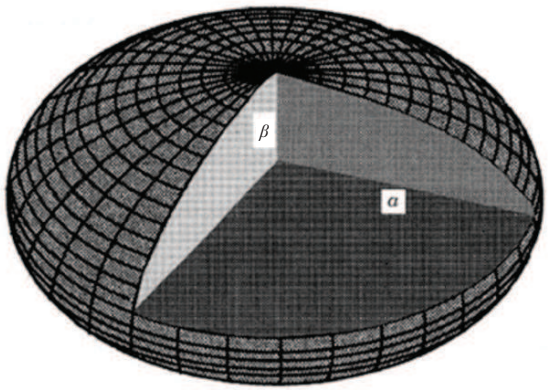


Figure 2.14: oblate ellipsoid. $2a$ is the major axis and β is the minor axis

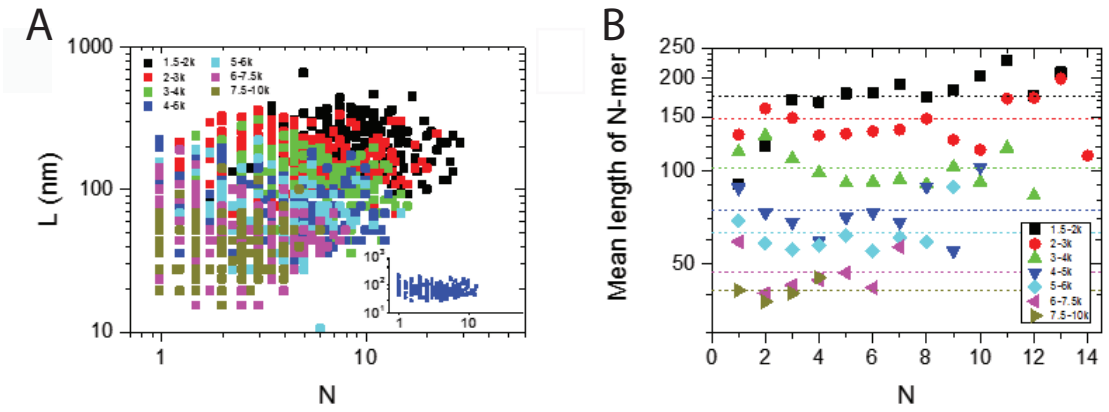


Figure 2.15: (A) <N> and <L> distribution of selected samples by simple LCC. (B) <L> of each layer number (N) subgroup inside each sample. It looks clear that the centrifugation protocol selects the flakes attending mainly to <L>, as N doesn't play an important role in the selection via centrifugation.

particles via centrifugation. In that case the force that causes the movement is the centrifugal force:

$$F_c = m_{eff} r \omega^2 \tag{2.62}$$

Then,

$$v_s = \frac{m_{eff} r \omega^2}{f} \tag{2.63}$$

Note that the bigger our particle the faster the sedimentation. f is the frictional coefficient, which depends on particles geometry. If we assume that the dispersed flakes are an extremal case of an oblate (an ellipsoid of revolution, Fig. 2.14) where its major axis ($2a$) is much bigger than the minor axis (2β), the frictional coefficient is [144]:

$$f = \left[\frac{(\frac{a^2}{\beta^2} - 1)^{1/2}}{(\frac{a}{\beta})^{2/3} (\arctan[(\frac{a^2}{\beta^2} - 1)^{1/2}]} \right] 6\pi\eta(a^2\beta)^{1/3} \tag{2.64}$$

$$f \approx 12\eta a \tag{2.65}$$

where η is the viscosity of the solvent. Taking Eq. 2.65 to Eq. 2.63 and we replace the partial specific volume as the inverse of the density, the sedimentation speed of a flake of thickness t and aspect ratio $K = L/W$ is:

$$v_s = \frac{r\omega^2 L}{12\sqrt{K}\eta} t\left(\rho_{flake} - \rho\right) \tag{2.66}$$

Size selection through centrifugation of 2D nanoflakes is not fully understood and the latest experiments [118] suggest that this model might be too simple. During a typical

size selection process (liquid cascade centrifugation, LCC), where the flakes are selected by collecting the sediment trapped between two centrifugation speeds, flakes sedimentation is done as a function of their lateral length(not the product $t \times L$ as it should be in accordance with Eq. 2.66). In each selected sample flake lengths (L) are roughly constant for different flake thicknesses (t) (Fig. 2.15).

Chapter 3

Exfoliation of WS_2 in PVA/Water Dispersion

This chapter is based on the publication [145]. Dr. Claudia Backes and me contributed equally to this work.



Figure 3.1: Link to the article *PL from Liquid-Exfoliated WS_2 Monomers in Poly(Vinyl Alcohol) Polymer Composites* online version [145].

3.1 Exfoliation in PVA/Water Dispersion and WS_2/PVA Composite Formation

3.1.1 Introduction

Over the last few years, the study of 2D materials has become one of the most vibrant areas of nanoscience. Although this area was initially dominated by research into graphene, it has since broadened to encompass a wide range of 2D materials including BN, TMDCs, TMOs such as MoO_3 and RuO_2 as well as a host of others including BP, silicene, and germanene. These materials are extremely diverse and have been employed in a wide range of applications in areas from energy to electronics to catalysis [19], [48], [146], [147], [148].

2D nanosheets have been seen by many authors as ideal for inclusion in advanced composites. Nanoclay-polymer composites [149] have been studied for decades while graphene has been widely explored as a filler in nanocomposites [150], [151], particularly for mechanical reinforcement [152] and optical applications [153], [154], [155].

However, the broader family of inorganic 2D materials has only recently been targeted for composite applications. For example, both BN and MoS_2 have followed graphene as fillers for mechanical reinforcement of polymers [60], [156], while MoS_2 has also been used as an additive to reduce wear and improve fire retardency in plastics [157], [158] and for photoactuation applications [159]. In addition, both MoS_2- and $MoSe_2$-filled composites have been used as saturable absorbers for the production of fiber lasers [160], [161], [162], [163], [164].

For composite applications, because large quantities of 2D nanosheets are usually required, probably the most suitable nanosheet production method is LPE. In this method, layered crystals, usually in powdered form, are exfoliated by ultrasonication [52], [56] or shear mixing [55], [165], usually in appropriate solvents or surfactant solutions. After centrifugation to remove any unexfoliated powder, this method gives dispersions containing large quantities of high quality nanosheets. A significant advantage of this approach is its versatility; it has been used to exfoliate graphene [52], [165], [166], [167], [168], [169], BN [60], a range of TMDCs [55], [56], [57], [58], and TMOs [53], [54] as well as BP [61], [170], [171], [172], [173] and a host of other 2D materials [174], [175]. Another advantage is the inherent processability of nanosheet dispersions. They can be fractionated to select nanosheets by size [117], mixed with dispersions of other nanomaterials to create hybrids [56], [176] or fabricated into films or other structures [48].

It is also very simple to produce polymer-based composites from nanosheet dispersions. In the applications described above [85], [156], [160], [161], [162], [164] the nanosheets were generally first exfoliated in solvents or surfactant solutions and then mixed with polymer solutions. The resultant composite dispersions can then be cast or formed as required. However, an even simpler composite formation route has been described [177], [178]. Nanosheets can be exfoliated directly by sonication or shearing in polymer solutions [165], [169], [179]. Any exfoliated nanosheets are then coated with polymer chains and sterically stabilized against reaggregation [179], [180]. The resultant dispersions can be cast directly into composite films which have been studied for mechanical applications [177], [178]. However, exfoliation in polymer systems is still rather immature compared to LPE in solvents or surfactant systems. For example, while some work has been done to identify the rules relating polymer/solvent/nanosheet combinations [179], no work has been done to study the effect of polymer concentration, centrifugation conditions or other processing parameters.

There are also other problems associated with composite formation, notably in relation to aggregation. If care is not taken, nanoscale fillers tend to aggregate during composite formation. This is particularly problematic for high aspect ratio 2D fillers which can show aggregation effects even at loading levels below 0.5% [177], [178], [181], [182]. Such aggregation is almost always detrimental to the properties of the composite, for example resulting in fall off in mechanical properties [177]. Alternatively for optical applications, well-defined properties associated with monolayers might be required which would be destroyed by aggregation. This makes the ability to control aggregation during composite formation very important. To do this, it will first be necessary to routinely monitor the aggregation state of the filler particles. Such rapid and routine monitoring techniques are currently not available.

In this paper we address both the problem of the lack of detailed characterization of direct polymer exfoliation and the lack of rapid screening of the aggregation state. We used poly(vinyl alcohol) (PVA) as a model polymer system to study the liquid exfoliation of WS_2 in water. PVA has been chosen as a model because of the results of the preliminary work of Appendix A. By using semiquantitative spectroscopic metrics, we tracked nanosheet length, thickness, and monolayer content during the exfoliation and

postexfoliation size selection by centrifugation. When the monolayer content is increased by appropriate centrifugation conditions, we observe luminescence from monolayered nanosheets. The ability to use luminescence measurements of monolayered WS_2 allowed us to track whether aggregation occurs on drying, i.e., during composite formation. Importantly, while we observe a change in doping level of the nanosheets in the dried state, the luminescence from monolayered WS_2 is preserved even in composites with high WS_2 loading level.

3.1.2 Results and discussion

3.1.2.1 Polymer-stabilized nanosheets: microscopy

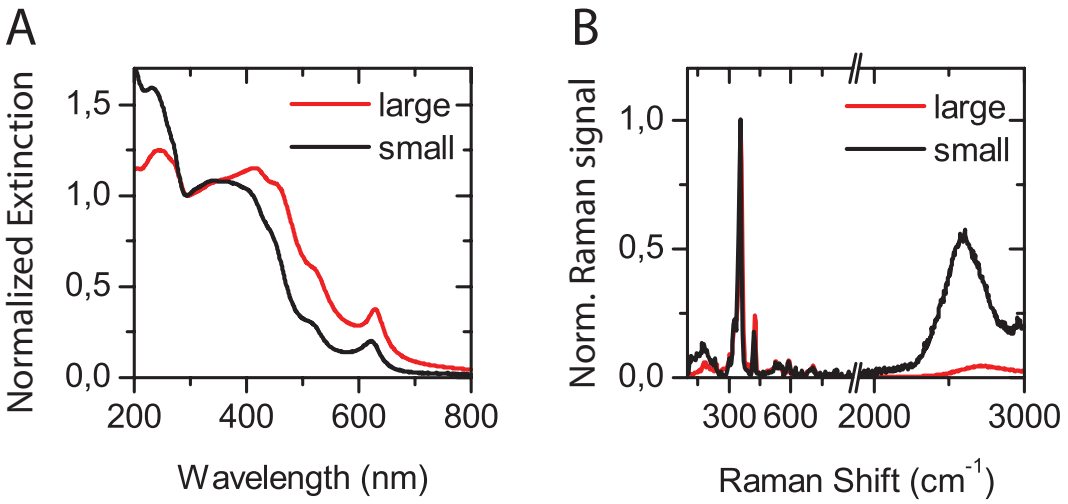


Figure 3.2: (A) Optical extinction spectra and (B) Raman/PL spectra of dispersions of PVA-stabilized WS_2 nanosheets produced using two different centrifugation regimes resulting in large and small nanosheets.

To gain insights in liquid exfoliation of TMDCs using polymers as stabilizers, we have focused on WS_2 and PVA in water as a model system. PVA/water is a well-known stabilizer and has been shown to exfoliate both graphene and BN nanosheets [177], [178]. We produced exfoliated WS_2 nanosheets by sonicating powdered tungsten disulphide (initial concentration C_i = 30 g/L) in an aqueous solution of poly(vinyl alcohol) (C_{PVA} = 2 g/L) for 1 h. Any unexfoliated crystallites were removed by centrifugation, initially using two distinct sets of conditions utilizing relatively high and low rotation speeds. Under such conditions we would expect to achieve dispersions of relatively small and large nanosheets respectively [117], [183].

The simplest way to characterize such dispersions is by extinction spectroscopy (usually referred to as absorption spectroscopy). As recently shown, this is a powerful technique for the characterization of liquid-exfoliated TMDCs, as the spectra not only contain information on dispersed nanosheet concentration, but also on mean length and thickness of the exfoliated TMDCs [117]. The length dependence is due to the effect of nanosheet edges on the spectral profile while quantum confinement effects result in well-defined shifts in A-exciton position with nanosheet thickness.

Shown in Fig. 3.2 A are extinction spectra normalized to the local minimum measured for large and small PVA-stabilized WS_2 nanosheets. These spectra are typical of

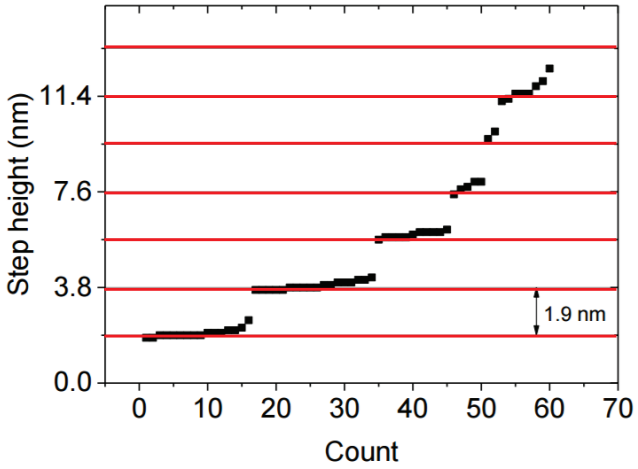


Figure 3.3: AFM height of the edge of incompletely exfoliated nanosheet. The step height is constant (1.9 nm), this step will be considered in the following as monolayer thickness.

WS_2 and display the characteristic A-exciton at $\sim$ 625 nm. The spectra are of slightly different shapes, consistent with the different lateral nanosheet sizes [117]. In addition, the A-exciton positions are slightly different from each other indicating that, in addition to differences in lateral size, the mean nanosheet thickness is different in each sample [117].

Raman spectroscopy is an important tool for the characterization of liquid-exfoliated nanosheets [29], [41], [42], [44]. Usually, Raman spectroscopy is performed on nanosheets which have been deposited on a surface. However, here we performed Raman characterization directly on the dispersion. We achieved this by using a Raman spectrometer to probe individual droplets of WS_2 dispersion on a microscope slide. Typical spectra (excitation wavelength 532 nm) are shown in Fig. 3.2 B for both large and small nanosheets. In addition to the characteristic Raman modes of WS_2 (e.g., the 2LA(M) at 352 cm^{-1}) [41], [184], a broad peak is observed at $\sim$ 2580 cm^{-1} (617 nm, 2.00 eV). We attribute this peak to PL from monolayered WS_2 [29], [185]. It is clear from this data that when normalized to the main Raman mode at 352 cm^{-1}, the PL is considerably stronger for the dispersion of small nanosheets. While both monolayered and few-layered WS_2 will contribute to the Raman signal, only monolayers display any significant PL. This means that the ratio of PL intensity to Raman intensity is related to the monolayer content in the dispersion. Because the PL/Raman ratios were I_{PL}/I_{Raman} = 0.04 and 0.55 for large and small nanosheets, respectively, this in turn implies that the monolayer content is considerably higher in the dispersion of smaller nanosheets.

In order to characterize the differences between the nanosheets in the dispersions, we deposited nanosheets both on holey carbon transmission electron microscopy (TEM) grids and Si/SiO2 substrates for statistical TEM and atomic force microscopy (AFM) analysis. Typical TEM images of large and small nanosheets, respectively, are shown as insets in Fig. 3.4 A, C. The lengths of a number of nanosheets in both dispersions were measured using TEM with histograms shown in Fig. 3.4 A, C. The nanosheet sizes were in the ranges 50–350 and 25–160 nm, respectively, for large and small nanosheets with corresponding mean nanosheet lengths of 120 and 60 nm.

The determination of mean nanosheet length using statistical TEM is well established

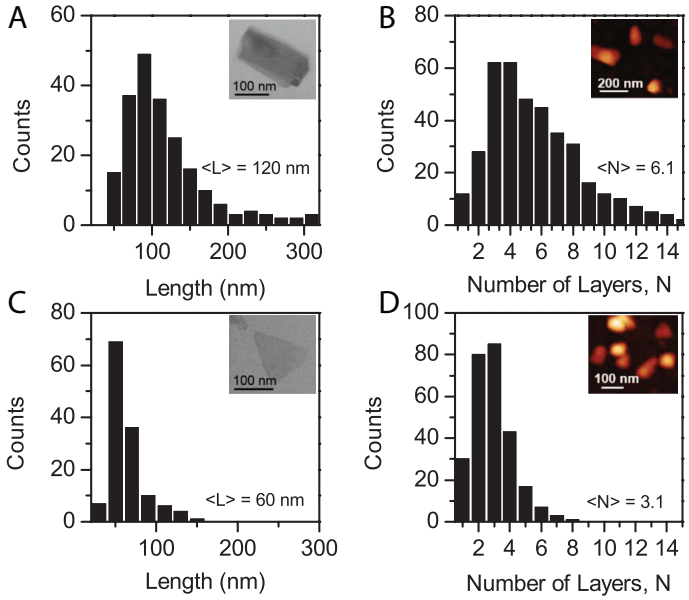


Figure 3.4: Statistical microscopic analysis of PVA-stabilized WS_2 nanosheets. Insets show representative images. (A,B) TEM length histograms for large and small nanosheets, respectively. (C,D) AFM thickness histogram (expressed as number of monolayers, N, per nanosheet) for large and small nanosheets, respectively.

and reasonably straightforward. However, determination of the mean number of layers or monolayer content from AFM is more challenging. One obstacle is that stabilizers such as solvent, surfactant or polymer, may contribute to the measured apparent AFM thickness so that nanosheets with a given number of layers appear thicker than their theoretical values. Thus, it is important to remove as much free polymer/surfactant as possible (such as by centrifuging the polymer/WS_2 dispersion at high speeds and redispersing the sediment in water). Then, as it was demonstrated previously [61], [117], [165], [175], this problem can be overcome by analyzing the height of steps of incompletely exfoliated nanosheets allowing for a determination of number of layers from the measured AFM thickness (Fig. 3.3). We note that care must be taken to only measure individually deposited nanosheets such as the ones in the images in Fig. 3.4 B, D.

If these requirements are fulfilled, the number of layers of liquid-exfoliated nanosheets can be determined from statistical AFM analysis. The corresponding histograms for the WS_2–PVA samples are presented in Fig. 3.4 B,D for the large and small nanosheet samples respectively. The observed nanosheet thickness ranges were 1–17 and 1–8 monolayers per nanosheet with mean values of $< N >$ = 6.1 and 3.1 layers for the large and small nanosheets respectively. In addition to $< N >$ it is possible to estimate the monolayer content from the AFM data. This can be represented as the number fraction or the volume fraction of monolayers. The monolayer number fraction, number of monolayers divided by the total ammount of flakes (NML/NT), was found to be 3.1% and 11% for the large and small nanosheets respectively. Furthermore, the monolayer volume fraction can be measured by AFM, as long as length, L, and width, W, are recorded simultaneously to the thickness, N, for each nanosheet and enough nanosheets are counted to be statistically relevant. Care must be taken with the resolution limit and the overestimation of the lateral dimensions of the flake. A most detailed explanation is given in the suplementary information of [118] Fig. S8 where in a similar scenario the overestimation of the AFM

can be calculated for particles bigger than 6 nm. Then the volume fraction is given by

$$V_f = \frac{\sum_{ML} LW}{\sum_{All} NLW} \tag{3.1}$$

We have observed that flakes tend to exhibit an aspect ratio of 2:1, where L is the longer side and W the smaller. We have performed such an analysis and estimated the volume fraction of monolayers to be 0.3% for the large nanosheets and 5.3% for the small ones. We suggest that the measured PL intensity scales with the total volume of all monolayers probed by the laser beam while the Raman intensity scales with the total volume of all nanosheets. This implies the PL/Raman ratio should scale with V_f rather than the number fraction. To test this we calculated the ratio of PL/Raman, which we compare to both NML/NT and V_f for both nanosheet samples. For large and small nanosheets, we found (PL/Raman)/(NML/NT) to be ~ 1.3 and ~ 5 and (PL/Raman)/V_f to be ~ 13 and ~ 10, respectively. This is indeed consistent with the suggestion that $I_{PL}/I_{Raman} \propto V_f$.

3.1.2.2 Optimization of the polymer concentration

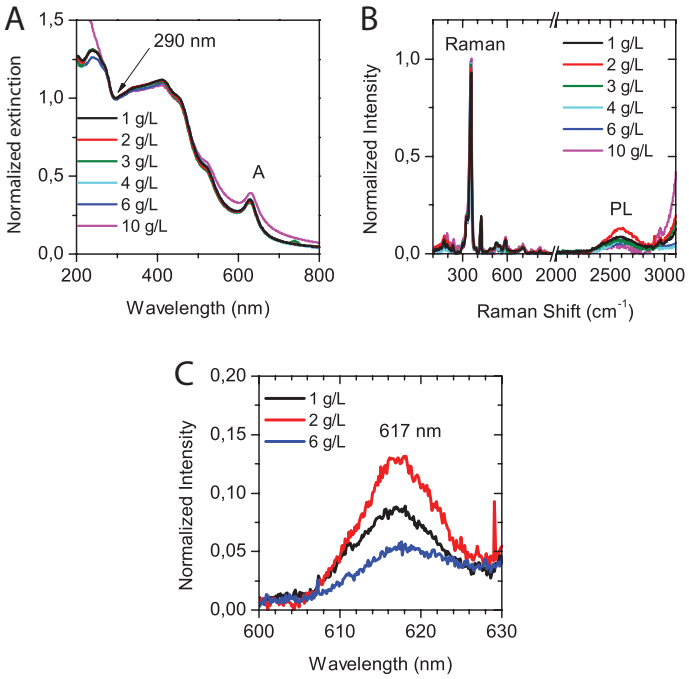


Figure 3.5: (A) Normalized extinction spectra of WS_2 (initial concentration C_i g/L) exfoliated in PVA–H_2O with different concentrations of PVA, C_{PVA} after mild centrifugation (centrifugation speed 24 g, 12 h). No spectral changes are observed, suggesting that the nanosheets have similar size and thickness distributions. (B) Raman/PL spectra (λ_{exc} =532 nm) of WS_2 exfoliated in PVA–H_2O with different concentrations of PVA normalized to the main Raman mode. (C) Zoom-in of the photoluminescence for a subset of the samples showing PL from monolayered WS_2 at 617 nm.

Above, we have demonstrated that WS_2 can be exfoliated and stabilized in aqueous PVA solutions with nanosheet size depending on the centrifugation conditions. However, the

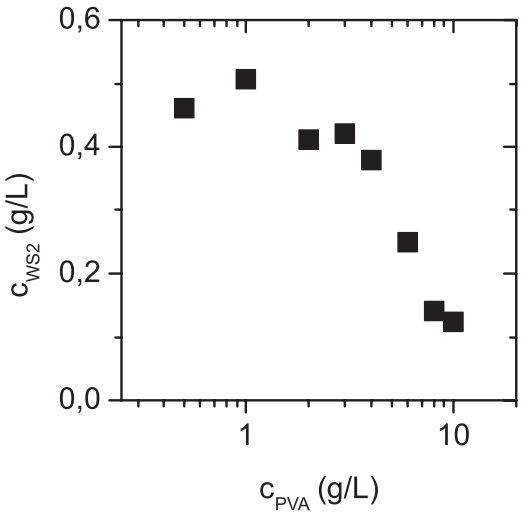


Figure 3.6: Plot of dispersed WS_2 concentration as a function of PVA concentration.

appropriate processing parameters remain unknown. In liquid phase exfoliation, the main parameters are initial concentration of WS_2 (C_i), processing/sonication time, t, power, P, and volume, V, as well as stabilizer concentration, C_{PVA}, and centrifugation conditions [55], [165]. As dispersed concentrations tend to scale monotonically with initial concentration and inputted energy density ($P \times t/V$) [165], [186], these parameters are important, but not very interesting. More interesting are the stabilizer concentration and centrifugation conditions as both these parameters tend to control not only the dispersed concentration but also the nanosheet size and so presumably the monolayer content [55], [117], [183].

Since little is known about the effect of polymer concentration on either dispersed nanosheet concentration or size, we first studied the exfoliation for a range of PVA concentrations. Liquid-exfoliated WS_2 was prepared by sonicating WS_2 powder in a range of PVA–H_2O solutions with different C_{PVA}, followed by low-speed centrifugation (24.4g, 12 h) to remove unexfoliated material (see the Experimental Section). The resultant dispersions were characterized by UV–vis extinction spectroscopy with the normalized extinction spectra displayed in Fig. 3.5 A for a range of C_{PVA}.

We found significant variations in the dispersed concentration of WS_2 as determined from the measured extinction according to the Beer–Lambert law using the extinction coefficient of liquid-exfoliated WS_2 (see Fig. B.1 in Appendix B). The concentration of WS_2 nanosheets (Fig. 3.6) was roughly constant at $WS_2 \sim 0.5$ g/L for PVA concentrations up to $C_{\mathrm{PVA}} \sim 3$ g/L. However for higher PVA concentrations, C_{WS_2} fell sharply. Similar behavior has previously been observed from anionic surfactant-exfoliated MoS_2 and was attributed to depletion interaction and charge screening [55]. While screening effects are unlikely to be important here, the depletion interaction may be relevant at high PVA concentrations. In addition, we suggest that the increased viscosity associated with higher polymer concentration may play a role. This suppresses motion during the sonication-based exfoliation thus reducing the efficiency of the exfoliation process ultimately leading to lower dispersed nanosheet concentration under equal sonication conditions.

As discussed above, extinction spectra of nanosheets contain information about mean nanosheet size and thickness. As previously shown for surfactant-exfoliated MoS_2 and to

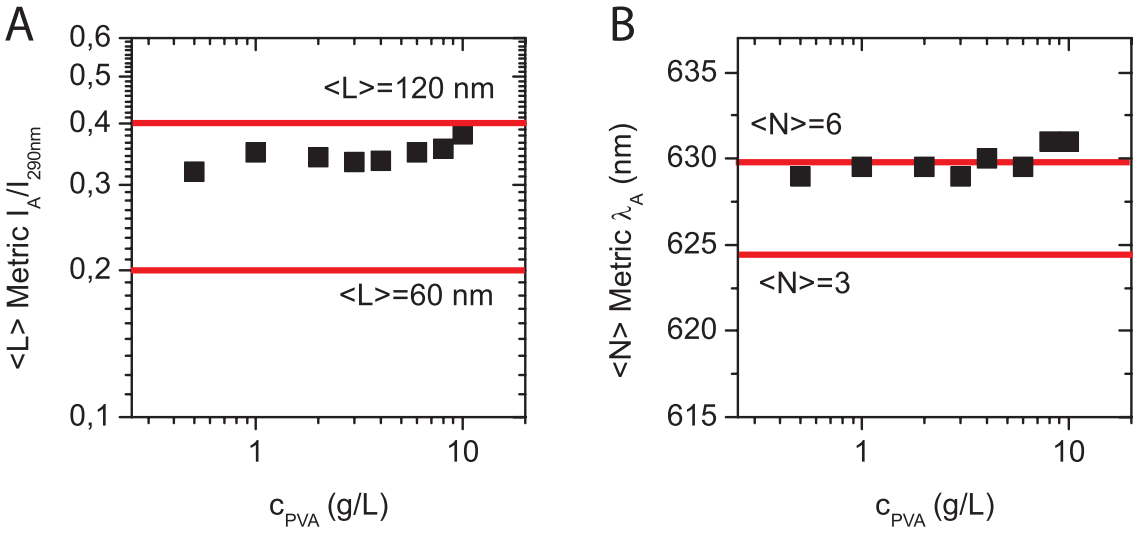


Figure 3.7: (A) Length metric expressed as the extinction intensity ratio of the A-exciton/local minimum as a function of PVA concentration showing no significant changes. The red lines indicate values of the length metric for which nanosheet length has been measured by TEM. (B) Thickness metric expressed as the peak position of the A-exciton as a function of PVA concentration also showing no changes in thickness. The red lines indicate values of the thickness metric for which nanosheet thickness has been measured by AFM.

some extent WS_2 [117], the mean nanosheet length can be related to the peak intensity ratios in the optical spectra. In the case of WS_2, the ratio at the A-exciton/the local minimum at 290 nm, Ext_A/Ext_{290nm} appears to be a suitable choice as the spectral profile changes significantly (see Fig. 3.2 A) for different nanosheet sizes. Here, we therefore refer to this parameter as the $< L >$ metric. In addition, the mean nanosheet thickness is related the spectral position of the A-exciton, λ_A (determined from the second derivative, $\frac{d^2Ext}{d\lambda^2}$, as described in ref. [117]). Here, we refer to λ_A as the $< N >$ metric.

It is clear from Fig. 3.5 A that the spectral profile does not show any significant changes with polymer concentration, indicating that C_{PVA} does not influence mean nanosheet size or thickness. This is confirmed by the plots in Fig. 3.7 A, B showing the length and thickness metrics, respectively, to be invariant with PVA concentration. The data presented in Fig. 3.2 and 3.4 allows us to associate measured values of both $< L >$ and $< N >$ with two specific values of the length and thickness metric (red lines). This shows the dispersed nanosheets to be slightly below 120 nm long and ~ 6 layers thick for all PVA concentrations studied. This invariance of nanosheet dimensions with PVA concentration is in stark contrast to recently reported results for the size and thickness of MoS_2 nanosheets exfoliated in aqueous surfactant solutions with varying surfactant content [55]. This is most likely due to differences in the mechanisms of polymer stabilization (steric) versus surfactant stabilization (electrostatic) [180].

In addition to measuring the mean nanosheet concentration, length and thickness as a function of process parameters, it is of great interest to gather information on the content of monolayers produced in the exfoliation. As discussed above, we propose that this can be achieved for a nanosheet dispersion by measuring the Raman/PL spectra and

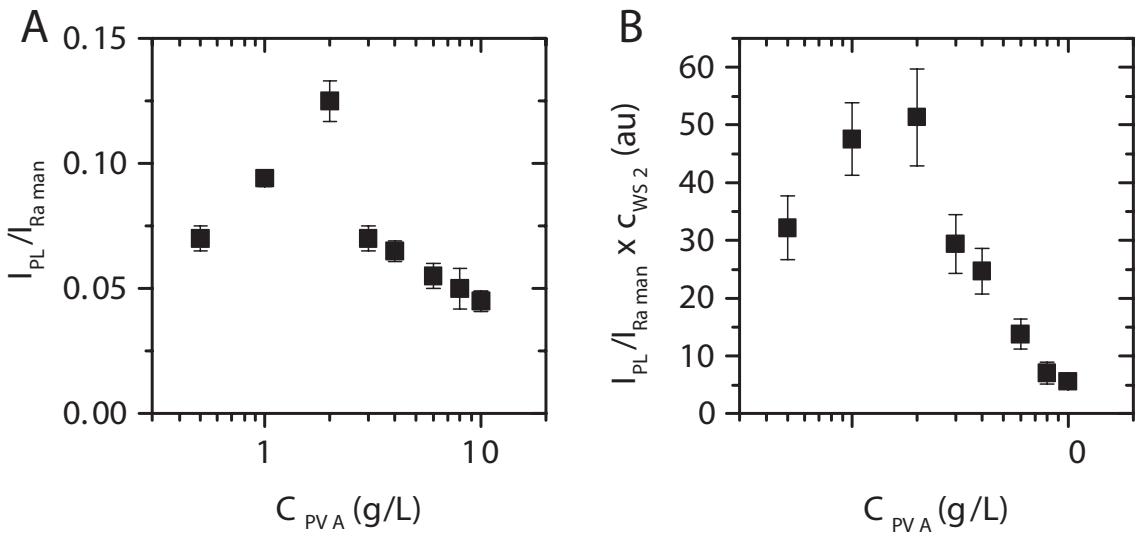


Figure 3.8: (A) Plot of PL/Raman intensity as a function of PVA concentration. (B) Plot of PL/Raman intensity multiplied by the dispersed concentration of WS_2.

using $I_{\mathrm{PL}}/I_{\mathrm{Raman}}$ as a measure of the monolayer volume fraction.

The Raman and PL spectra (excitation wavelength 532 nm) were measured simultaneously on droplets as described above and in the Experimental Section. The resultant spectra are shown in Fig. 3.5 B normalized to the main Raman phonon (2LA(M) at 352 cm^{-1}. Although weaker than that shown in Fig. 3.2, PL can clearly be seen around 2600 cm^{-1}. Fig. 3.5 C shows a magnification of the PL for a subset of the samples where wavenumber has been converted to wavelength. This clearly demonstrates that the PL/Raman ratio varies with C_{PVA}, which may suggest that the monolayer volume fraction depends on the PVA concentration. The $I_{\mathrm{PL}}/I_{\mathrm{Raman}}$ ratio is plotted as a function of PVA concentration in Fig. 3.8 A. It first increases with PVA concentration before falling off at PVA concentration > 2 g/L. While this may indicate that the monolayer volume fraction peaks at ~ 2 g/L, care must be taken with this interpretation. In addition to monolayer population, changes in PVA concentration may lead to different packing densities of PVA on the nanosheet surface. This changes the dielectric constant which may have an impact on the observed PL intensity [187]. More detailed studies will be needed to clarify this. Nonetheless, the data is instructive, as our target was also to produce samples with maximized ML PL, as will be discussed further down below.

Since we observed the dispersed WS_2 concentration to decrease with PVA concentration, it is also important to test whether the actual monolayer PL per WS_2 mass of the stock dispersion also peaks at C_{PCA} = 2 g/L. We therefore plot $I_{PL}/I_{Raman} \times C_{WS_2}$ as a function of PVA concentration in Fig. 3.8 B also showing a peak at a PVA concentration of 2g/L. This means that in order to maximize luminescence and potentially monolayer volume fraction, a PVA concentration of 2 g/L is beneficial and hence chosen for the remainder of the study.

We note that the PL measurements, shown in Fig. 3.5 B, C, were obtained without any size selection. This is in contrast to previous reports on PL of liquid-exfoliated MoS_2 measured using a PL spectrometer [117]. In that case, without size selection to increase the monolayer population, no PL was observed.This illustrates the advantages of using a

Raman spectrometer to acquire PL spectra from the surface of a liquid drop.

3.1.2.3 Optimization of the postexfoliation centrifugation.

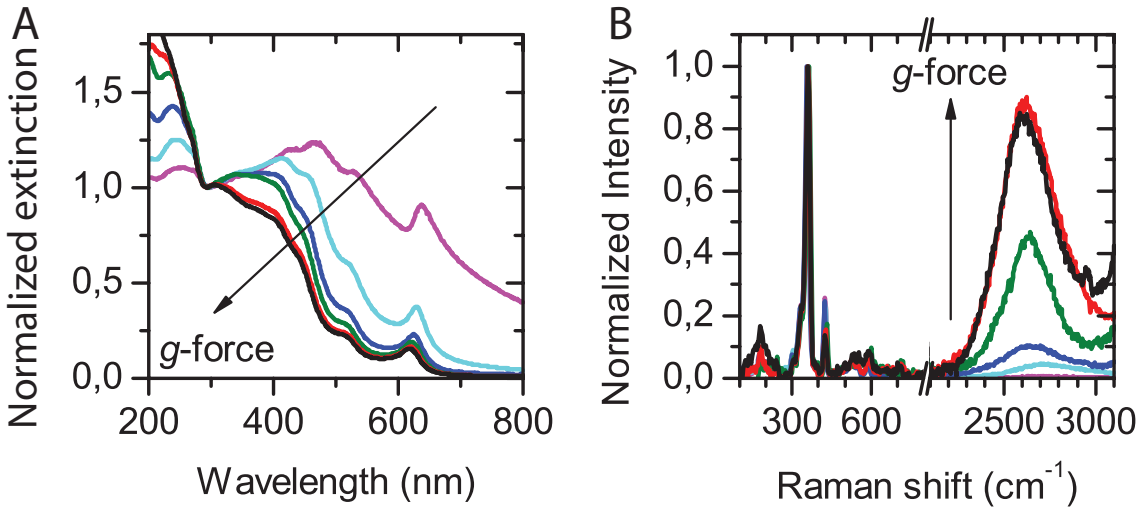


Figure 3.9: (A) Normalized extinction spectra of WS_2 exfoliated in PVA–H_2O (C_i = 30 g/L, C_{PVA} = 2 g/L) after centrifuging at different rotational speeds (1.5 h each step) showing characteristic changes in the spectral shape reflecting different sizes and thicknesses obtained. (B) Raman/PL spectra (λ_{exc} = 532 nm) of WS_2 exfoliated in PVA–H_2O after centrifuging at different rotational speeds. The relative PL intensity, i.e., the volume fraction of monolayers increases as the centrifugal force is increased.

In order to improve the monolayer content in the dispersion and hence optimize the PL intensity, we performed size selection by controlled centrifugation with increasing centrifugation velocities in consecutive steps similar to procedures described previously [61], [165], [175]. Details are given in the Experimental Section. This procedure has been shown to yield dispersions with varying mean size and thickness distributions and, as we will describe below, different monolayer volume fractions. The normalized extinction spectra (Fig. 3.9 A) show expected changes in spectral features for the size-selected dispersions, consistent with both nanosheet size and thickness decreasing with increasing g-force. The length metric, ExtA/Ext295 nm is plotted as a function of mean centrifugal force in Fig. 3.10 B illustrating significant variations in mean nanosheet lengths from $>$ 120 nm at low rotation rate to $<$ 60 nm at high rotation rate. Similarly, the thickness expressed via the A-exciton peak position, λ_A, in Fig. 3.10 C also confirms the size selection with $< N >$ falling with rotation rate from >6 at low rate to $<$ 3 at high rate.

To test whether the changes in length and thickness distributions coincide with different volume fractions of monolayers, the dispersions were subjected to liquid Raman/PL measurements.

The resultant spectra are displayed in Fig. 3.10 B and show that this is indeed the case. Values of I_{PL}/I_{Raman} of up to 1 (indicating relatively high monolayer populations) could be achieved by this simple centrifugation procedure. We plot the PL/Raman peak intensity ratio as a function of centrifugal force in Fig. 3.10 B. The horizontal lines indicate the volume fraction of monolayers determined by AFM on two samples (see Fig,

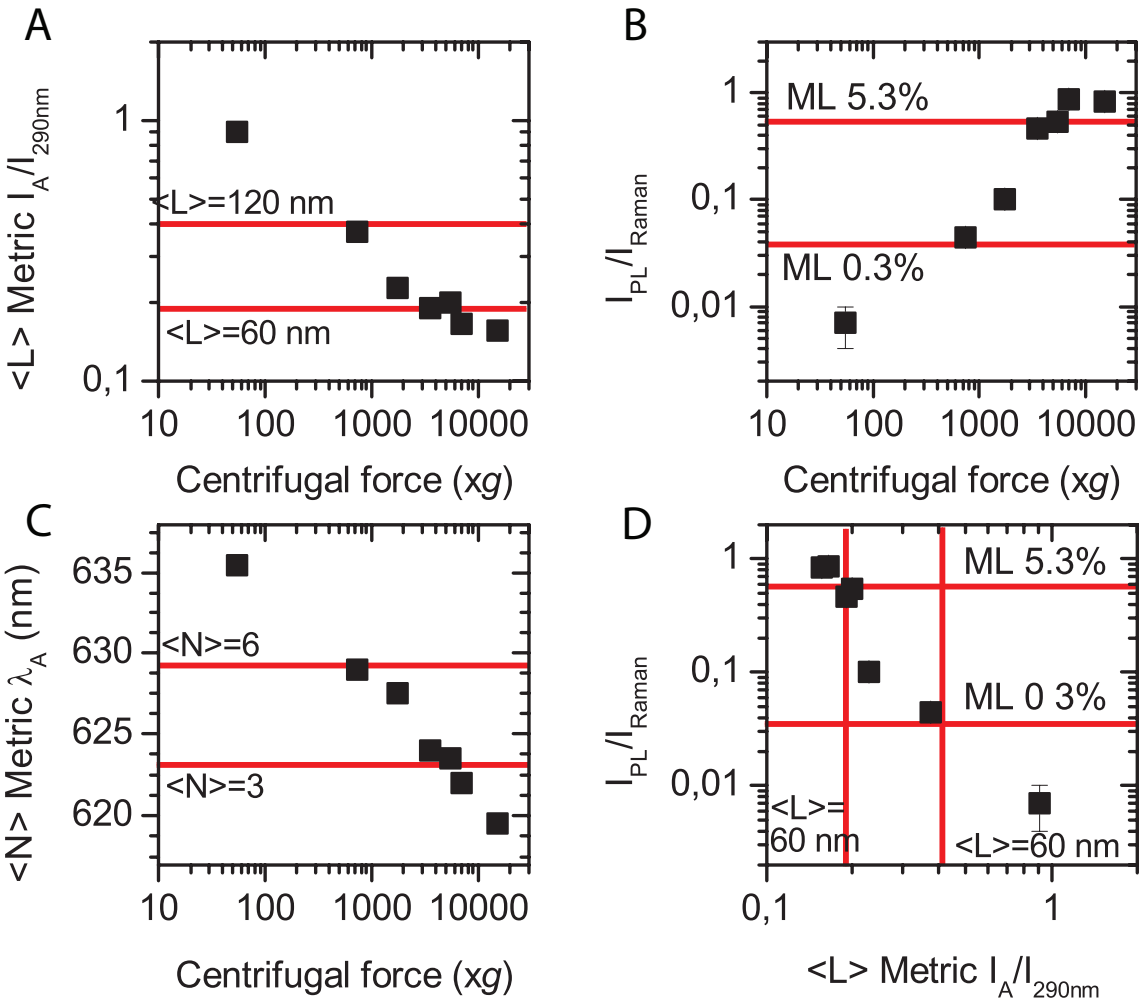


Figure 3.10: (A) Length metric expressed as the extinction intensity ratio of the A-exciton/local minimum as a function of the centrifugal force. The red lines indicate values of the length metric for which nanosheet length has been measured by TEM. (B) Plot of PL/Raman intensity as a function of centrifugal force. The red lines indicate values of ML volume fraction metric for which nanosheet thickness has been measured by AFM. C) Thickness metric expressed as the peak position of the A-exciton as a function of the centrifugal force. The red lines indicate values of the thickness metric for which nanosheet thickness has been measured by AFM. (D) Plot of PL/Raman intensity as a function of nanosheet length metric with measured values of each metric shown as red lines.

3.2 and 3.4). The PL/Raman ratio, and so the monolayer V_f, increases with rotation rate but, interestingly, saturates for very high centrifugation speeds. This is somewhat unexpected and could be attributed to the fact that the nanosheets in this case are also very small (Fig. 3.10 A) in lateral dimensions so that the PL of the monolayers is potentially quenched by edge effects. This has previously been observed for very small liquid-exfoliated MoS_2 nanosheets [117]. We can observe the relationship between monolayer content and nanosheet size in Fig. 3.10 D, where we plot I_{PL}/I_{Raman} as a function of the nanosheet length metric. This shows that to achieve monolayer $V_f > 5\%$ means accepting

monolayer length < 60 nm.

3.1.2.4 Optical properties of WS_2 during drying

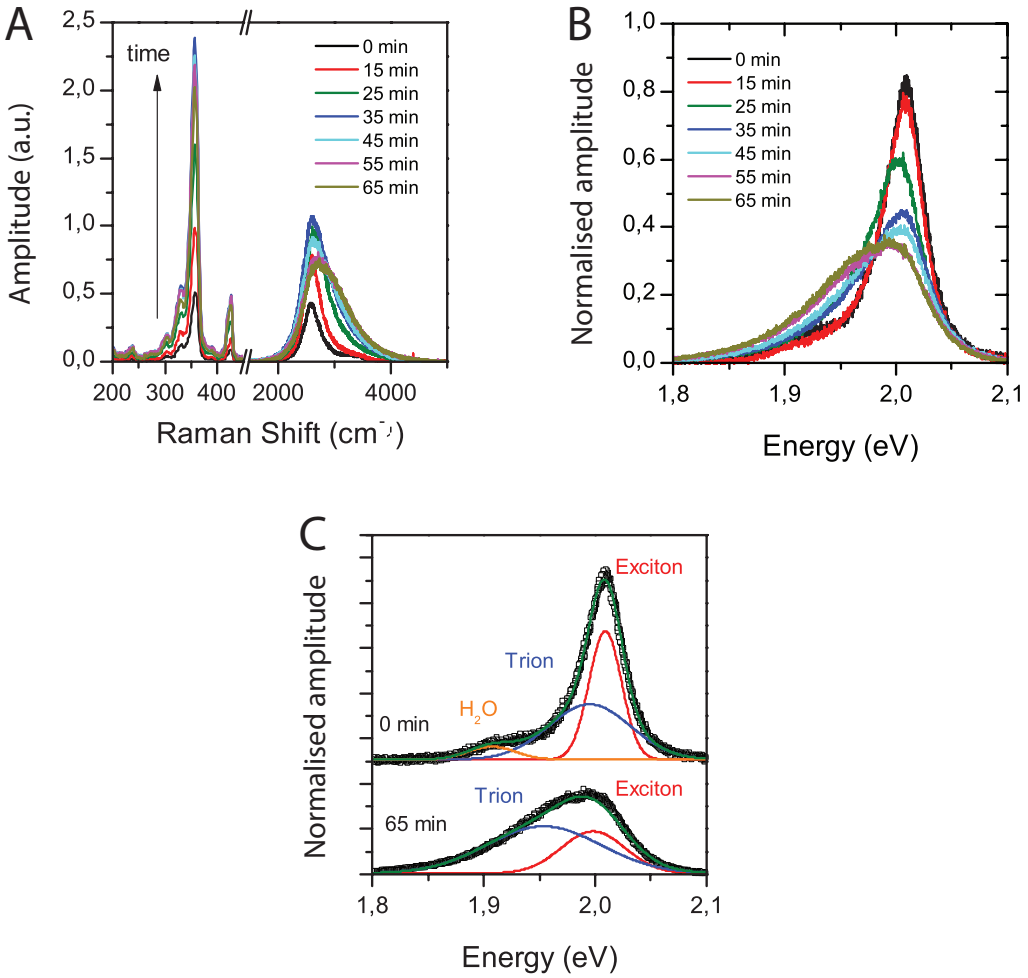


Figure 3.11: (A) Evolution of the Raman/PL spectra of small WS_2–PVA during drop drying. As the drop dries, the concentration is increased leading to more nanosheets being sampled during the measurement hence increasing the signal intensity. (B) Evolution of the PL spectra plotted versus energy after normalization to the Raman mode during drop drying. As the drop dries, the PL of WS_2 becomes lower in amplitude, broadens, and becomes more asymmetric. (C) The PL spectra can be fit with two (dried) or three (dispersion) Gaussian lineshapes, respectively, as exemplarily shown for two spectra. We attribute the components to emission from the exciton at highest energy, trion and slightly lower energy, and Raman scattering from water at ∼ 1.9 eV as indicated.

One of the great advantages of exfoliating nanosheets directly in polymer solutions is that the resultant dispersions can be used to form polymer–nanosheet composites simply by driving off the solvent [177], [178]. However, nanosheet aggregation during composite formation is always a significant problem. The ability to track the monolayer volume fraction using a Raman spectrometer allows us to probe aggregation effects during composite formation for the first time.

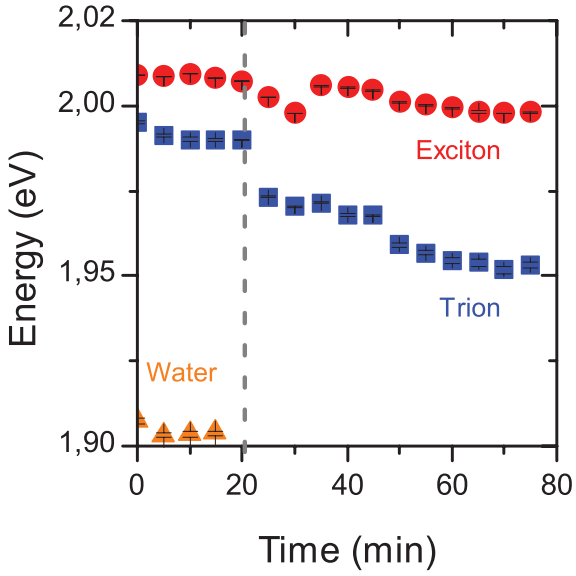


Figure 3.12: Evolution of exciton and trion energies as a function of time from fitting the spectra as shown in Fig. 3.12 C. The water has evaporated after ~ 20 min as indicated by the gray vertical line. Both exciton and trion energy decreases further after all water has evaporated before saturating at lower energies. We attribute this intermediate regime to conformational changes of the polymer.

To do this, we have monitored the Raman/PL spectra of a liquid drop ($C_{WS_2} \sim 0.1$ g/L, $C_{\mathrm{PVA}} = 2$ g/L, $m_{WS_2}/(m_{WS_2} + m_{PVA}) \times 100 \sim 5\ wt\%$ during drying at room temperature, measuring at 5 min intervals. A subset of the spectra is shown in Fig. 3.11 A, B. The as-recorded, nonnormalized spectra (Fig. 3.11 A) show an increase in signal intensity as the drop dries (N.B. the shoulder at 3330 cm^{-1} is the water Raman mode). This is because the concentration of WS_2 is increased as water evaporates so that more nanomaterial is sampled in each measurement. In turn, the spectra normalized to the 2LA(M) Raman mode (352 cm^{-1}) and plotted versus energy (Fig. 3.11 B) reveal that changes in the shape of the WS_2 PL are observed as the drying proceeds. The PL decreases in intensity, broadens, and becomes increasingly asymmetric. The drying/evaporation of water is furthermore reflected in the relative decrease of the water Raman mode at ~ 3330 cm^{-1}(~ 1.9 eV when excited with 532 nm).

To further examine the spectral changes, the PL spectra (normalized to the Raman mode of WS_2) were fit to Gaussian lineshapes as shown for two spectra in Fig. 3.11 C. The full set of spectra is shown in Fig. B.2 in the Appendix B. Since nanosheets of different sizes and random orientation are sampled in each measurement, we find Gaussian fits more appropriate than Lorentzians due to inhomogeneous broadening. In all cases, the WS_2 PL can be described well by two Gaussians which we attributed to emission from excitons at ~ 2.01 eV and trions at slightly lower energy [86], [188], [189]. In addition, the water Raman peaks can be identified in the 0–15 min spectra where the drop is still wet. For simplicity, we also fit this set of water peaks to a single Gaussian.

In Fig. 3.12 we plot the energies of the exciton and trion as the water is evaporated. After 15–20 min, no signal from the water can be identified so that we conclude that the drop has mostly dried at that stage. This time is indicated by the gray vertical lines in the figures. The PL positions of both exciton (2.01 eV) and trion (1.99 eV) are relatively constant for the first 20 min but begin to redshift once the water has mostly evaporated,

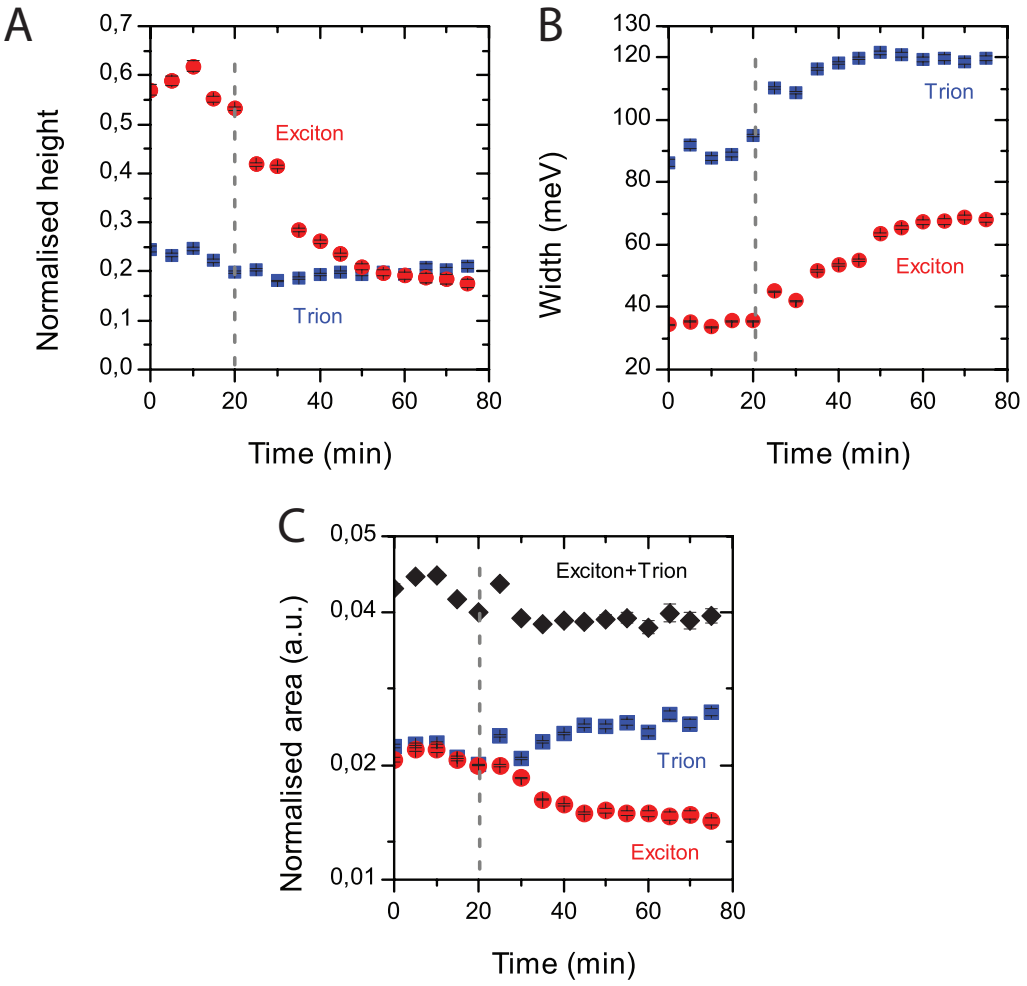


Figure 3.13: (A) Exciton and trion peak heights as a function of time. The trion intensity is widely constant, while the exciton intensity falls off. (B) Plot of exciton and trion peak widths as a function of time. Both components broaden in the dried state. (C) Plot of exciton, trion, and total PL area versus time. While the exciton area decreases, the trion area increases after evaporation of the water. Importantly, the total area stays roughly constant confirming that the monolayer properties are preserved in the composite, i.e., reaggregation is successfully prevented by the polymer.

saturating at 1.998 eV (exciton) and 1.95 eV (trion), respectively after ~ 70 min. We believe these shifts are associated with conformational changes of the polymer that occur as the water evaporates and the polymer either crystallizes or adopts an ideal chain conformation [190]. We expect such a rearrangement of the polymer on the nanosheet surface will lead to different levels of doping due to changes in the local chemical environment.

To confirm this, we also analyzed PL intensity, width and area as a function of drying time in Fig. 3.13 A, B, C. The PL intensity of the exciton (Fig. 3.13 A) dramatically decreases from 0.6 to 0.19 as the drop dries. Again, the dominant changes occur after the water Raman signal has disappeared (20 min). Interestingly, the trion height stays approximately constant over the whole time period. As shown in Fig. 3.13 B, this is accompanied by a broadening of the PL from both exciton and trion which likely reflects the changes in the dielectric constant around the nanosheets [187].

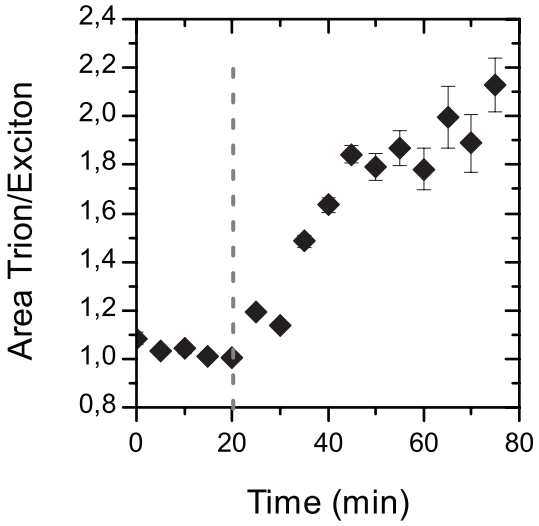


Figure 3.14: Plot of trion/exciton area showing an increase of the trion/exciton ratio by a factor of 2. This strongly suggests n-type doping from the PVA.

In Fig. 3.13 C, the PL areas of exciton and trion, as well as the summed area of both components are plotted versus time. This is of greatest relevance to understand whether reaggregation of the nanosheets is successfully prevented in the dried state due to the surrounding polymer. While the exciton area decreases, the trion area increases. Most importantly, the total PL area of both components stays broadly constant. This transfer of exciton PL to trion PL suggests an increase in the level of doping from the surrounding polymer in the dried state compared to the liquid state. This is best expressed as ratio of trion to exciton area in Fig. 3.14 showing an increase from the trion emission relative to the exciton emission by a factor of ~ 2. It is clear from this panel that the transfer of PL from exciton to trion only begins to occur once the water has mostly evaporated (20 min) and is about to saturate by the time 80 min have passed.

We rationalize these observations as follows. TMDCs are typically intrinsically n-type doped showing the characteristic trion emission [86], [187], [191], [192]. However, as shown by Peimyoo et al. [192], water can act as p-type dopant for WS_2, in particular when water molecules are allowed to adsorb in close proximity resulting in a higher exciton/trion ratio that would otherwise be observed. Despite the polymer coating, we are convinced that this can at least partially be the case for the measurement in liquid, as the polymer coating is not expected to be fully homogeneous. This gives initial trion/exciton areas of ~ 1. As the water is evaporated, the p-type doping from water is reduced. This results in broadened, redshifted PL and an increased trion/exciton ratio. While the water has mostly evaporated after 20 min, we suggest that there is a residual portion of water, perhaps interacting strongly with the PVA, which evaporates more slowly over the 20–80 min period. As this residual water evaporates, both the doping level and the polymer conformation change, resulting in the observed further changes in PL.

It was confirmed that these changes in the WS_2 PL are indeed related to the presence of H_2O–PVA and PVA rather than random restacking of the nanosheets by analyzing the PL of vapor-grown WS_2 before and after deposition of a liquid drop of PVA and after evaporation of the water. Qualitatively, the same result is obtained as summarized in Figs. B.3-B.5 and Table B.1 in the Appendix B. Interestingly, we observe an increase in the trion emission relative to the exciton emission as a drop of H_2O–PVA is placed on the

chemical vapor deposition (CVD)-grown WS_2. This is accompanied by a slight broadening of both the exciton and the trion. These spectral changes become even more prominent as the water is evaporated. This confirms that the evaporation of water changes the doping level on the WS_2 nanosheets in a similar way that we have observed by the measurement on the LPE nanosheets described in detail above. However, the trion/ exciton ratio is significantly larger on the CVD WS_2 with (dried) PVA deposited on the nanosheet compared to the same sample before being exposed to H_2O-PVA. This suggests that PVA may even act as a slight n-type dopant. However, further studies are required to confirm this.

While it is clear that the PL/Raman intensity is decreased in the dried compared to the liquid state due to the reduced exciton emission, it is very important to note that the PL area stays mostly constant. This suggests that the nanosheet–nanosheet aggregation is indeed successfully prevented by the polymer surrounding of the exfoliated nanosheets, at least at this mass fraction of ~ 5%. In addition, the drying experiment emphasizes that liquid-exfoliated TMDCs are ideal model systems to study the impact of molecules and polymers on the optical properties.

3.1.2.5 Production of luminescent WS_2–PVA composites

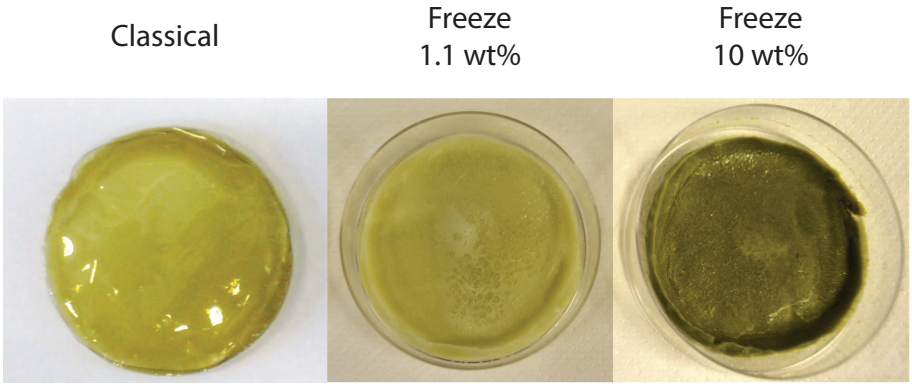


Figure 3.15: Photographs of WS_2–PVA (1.1 wt% WS_2 loading) composites obtained by means of classical composite (left) preparation (water evaporation by heat/vacuum) and by freeze drying (center). Freeze dried sample with higher WS_2 load (10wt%) was needed to acquire the Raman/PL spectra (right).

The knowledge that the WS_2 nanosheets do not catastrophically aggregate during drying of WS_2–PVA dispersions suggests that it should be possible to produce solid WS_2–PVA composite films with monolayer content which is high enough for the composite to be luminescent. To investigate this, we prepared WS_2–PVA composites in two different ways. Firstly, we applied standard solution processing techniques, casting the WS_2–PVA dispersion into a Teflon mold and drying at 328 K in a vacuum oven for 24 h (see the Experimental Section). This gave a shiny, transparent, bright yellowish–greenish colored film (Fig. 3.15 left). Alternatively, we prepared composites from the same dispersion by freeze-drying [193]. This gives soft, foam-like structures of a duller green color (Fig. 3.15 centre). In both cases, polymer and WS_2 concentrations were adjusted to C_{PVA} = 30 g/L and C_{WS_2} = 0.31 g/L to yield composites with a mass loading of 1.1 wt% of WS_2. In both cases, the composites looked quite uniform with no visual evidence of WS_2 aggregation. These as-produced polymer composites were subjected to Raman/PL measure-

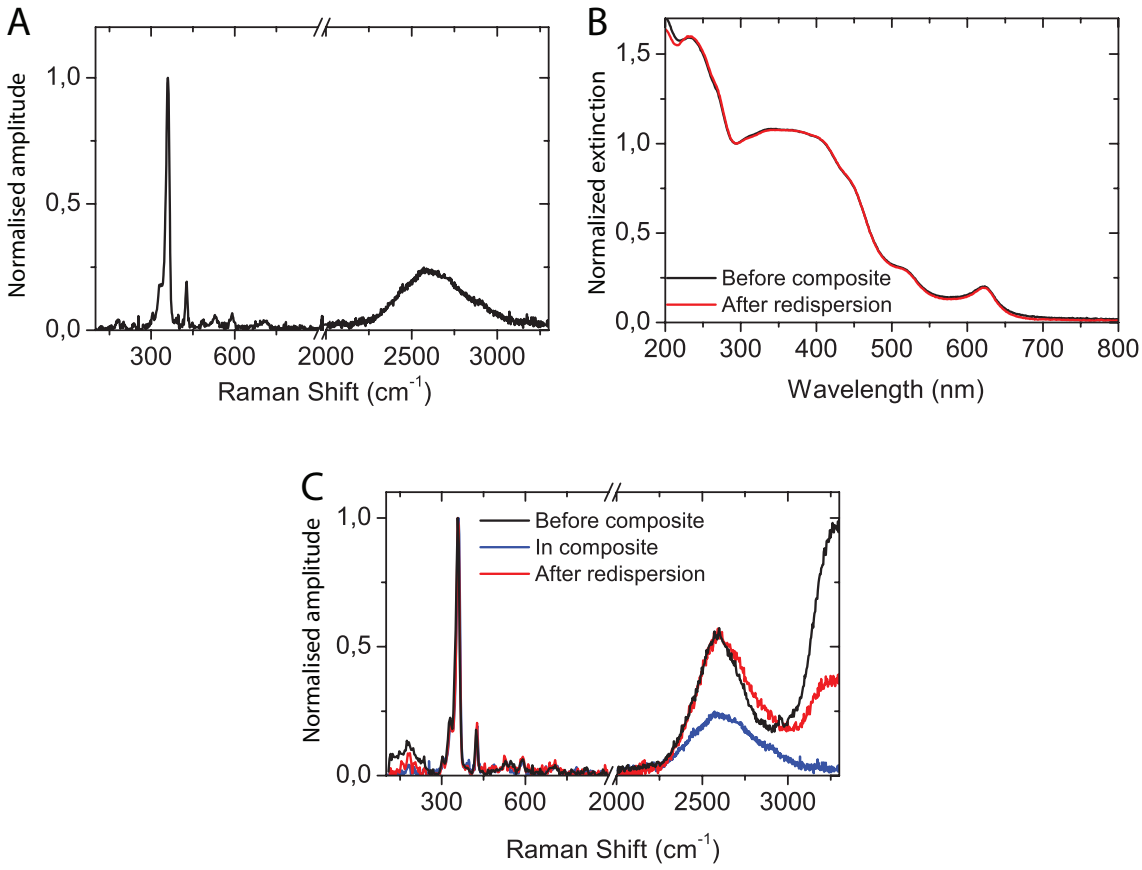


Figure 3.16: (A) Raman/PL spectrum of a freeze dried WS_2–PVA composite with 10 wt% of WS_2. (B) The freeze-dried composites can be readily redispersed in water by 5 min bath sonication. No changes in the extinction spectra before (black) composite formation and after redispersion (red) are observed. (C) Raman/PL spectra of PVA-WS_2 as exfoliated, in the freeze-dried composite and after redispersion of the composite. The PL is completely recovered. The spectral feature at higher inverse centimeters (> 3000cm^{-1}) is the Raman signal of water.

ments. Unfortunately, even though we reduced the laser power to 0.02 mW, the spectra were dominated by heating effects due to the low thermal conductivity of the PVA matrix (Fig. B.5, Appendix B).

To reliably acquire PL/Raman spectra from the polymer composite, we found it necessary to increase the WS_2 mass fraction to 10 wt% (C_{PVA} = 30 g/L and WS_2 C = 3 g/L). Under normal circumstances, such high filler loading would generally lead to aggregation during drying [181]. However, composite formation by freeze-drying should result in reduced aggregation. In freeze drying of polymers, solvent removal occurs so rapidly that the chains may not even have time to entangle [194]. By analogy, we do not expect the nanosheets to have time to aggregate but rather to remain surrounded by polymer chains. The resultant composite is shown in the Fig. 3.15 right and is a much darker color than before due to the higher WS_2 loading level. The Raman/PL spectrum of a freeze-dried WS_2–PVA composite (average of 100 spectra measured with 0.2 mW laser power) is displayed in Fig. 3.16 A. The WS_2 PL is clearly discernible with a PL/Raman

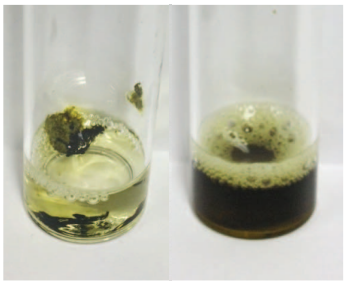


Figure 3.17: Photograph of the composite of Fig. 3.16 right. Before (left) and after (right) 5 min bath sonication.

peak intensity ratio of ~ 0.25. This indicates that considerable numbers of individual nanosheets remain unaggregated even at very high WS_2 loading levels.

A great advantage of the foam-like freeze-dried composites is that they can be readily redispersed in water by mild sonication (5 min in sonic bath). An example of a redispersed composite is shown in Fig. 3.17. On the left is a WS_2/PVA composite directly after immersing it in water and on the right after 5 min of bath sonication by which time it has completely redispersed. The extinction spectrum of the redispersed composite is shown in Fig. 3.16 B and is nearly identical to the spectrum of the starting dispersion. The bottom inset shows the A-exciton position to be virtually unchanged after redispersion, showing the mean nanosheet thickness to be the same in the redispersed and original dispersion. This is further confirmed by Raman/PL spectra in Fig. 3.16 C showing the PL spectrum of the redispersed composite to be virtually identical to that of the starting composite. This shows that whatever the aggregation state of the nanosheets in the polymer matrix, they can be very easily redispersed and returned to their original dispersed state. Consequently, any aggregation that does occur could not result in any strongly bound structures.

Finally, Fig. 3.16 C shows the PL area in the composite was 52% of the PL area of the dispersion used to prepare the composite (both normalized to the Raman peak at 352 cm^{-1}). This implies that during composite formation (drying), even for this high mass fraction (10 wt%), bulk composite, approximately half the WS_2 monolayers remain unaggregated. It is worth noting that while it is important to observe that the monolayer aggregation is not as severe as might be expected, this result does not tell us anything about the aggregation of few-layer nanosheets (because they are not luminescent). It is entirely possible that few-layers may aggregate at a significantly greater rate than monolayers. More work will be required to investigate this. In addition, we believe the low levels of monolayer aggregation may be largely due to the rapidity of composite formation during freeze drying and may not be replicable using standard composite formation techniques.

3.1.3 Conclusion

In summary, we have studied the exfoliation of WS_2 in aqueous PVA solutions where PVA is chosen as a model polymeric stabilizer. The effect of both polymer concentration and centrifugation conditions on dispersion concentration, nanosheet length, thickness, and monolayer volume fraction were studied by the aid of semiquantitative spectroscopic metrics based on extinction and Raman/PL spectra. After optimization of PVA concentration, we obtained dispersions with monolayer volume fractions of >5 % and easily

observable PL.

This allowed us to study the behavior of monolayers during film formation by slow solvent evaporation. By monitoring Raman/PL spectra of the dispersion on drying, we were able to show that compared to the liquid state, trion emission is increased at the cost of exciton emission reflecting a different chemical doping in the liquid compared to the dried state. Importantly, the PL of the monolayer is not quenched in the dried state due to efficient shielding of the randomly restacked nanosheets. The methodology described here is generally applicable to also shine light on polymer-based exfoliation and stabilization using a range of polymers in the future.

Finally, we fabricated WS_2–PVA composites by both standard composite formation and freeze drying. We showed that the PL from monolayers of the WS_2 is retained, but broadened and asymmetric in the freeze-dried composites with high WS_2 loading levels of 10 wt %. These composites are readily redispersible in water leading to a complete restoration of the spectral features. We expect these composites to be of interest for a number of studies on the optical properties of TMDCs, such as saturable absorbers [195] or second harmonic generators [23]. In addition, our results show that the ability to make monolayers-rich TMD dispersions offers exciting perspectives to study interactions with surrounding molecules and doping effects.

Chapter 4

Photoinduced Dynamics in Transition Metal Dichalcogenides

This chapter is based on the publication [196].



Figure 4.1: Link to the article *Exciton and charge carrier dynamics in few-layer WS_2* online version [196].

4.1 Ultrafast Dynamics in Non-Size-Selected WS_2

4.1.1 Introduction

Semiconducting transition metal dichalcogenides (TMDCs) have emerged as alternative active materials for applications in electronics, photovoltaics, and photonics, as has been demonstrated by the realization of nanoscale field-effect transistors (FETs) [20], integrated circuits, [197] photovoltaic elements, [198], [199], [200], [201], [202], [203] photodetectors, [72] light emitting transistors, [204] and nanoscale lasers [205]. For the design and optimization of such devices it is crucial to understand the non-equilibrium behavior of electrons. Strongly bound excitons (electron–hole pairs with binding energies up to 1 eV) are considered to be the primary photoexcited species in TMDCs, and their subsequent dissociation generates the charge carriers necessary for photodetectors and solar cells [102] . Both for applications as well as for basic photophysics, the best studied TMDC by far is MoS_2. However, other compounds may be better attuned to certain practical uses or better suited to reveal the underlying photoexcitation dynamics. In femtosecond optical spectroscopy of MoS_2, both excitons and charges show crowded

spectra with multiple photobleaching and photoinduced absorption peaks. The close proximity of the A and B exciton features (corresponding to the transition at the *K* point from the split valence band due to spin-orbit coupling, to the conduction band) leads to a strong spectral congestion and makes it difficult to untangle the contributions of the individual species. WS_2 shows similar peak widths with about twice the A–B energy separation, [206] which should enable one to resolve previously undetected relaxation processes.

The spectral signatures of excitons and charge carriers in TMDCs have been identified by absorption and fluorescence spectroscopy, where the charge concentration is varied either via the gate voltage in a FET geometry [86], via adsorption [190], [192] or substrate doping [207], or via photoexcitation [102], [208], [209]. The absorption peaks of charges are red-shifted by about 40 meV compared to the ground state absorption of the A and B excitons and have been attributed to optical transitions from a charged ground state to a charged exciton (trion). Recently, in few-layer MoS_2, photoinduced absorption peaks arising from photoexcited charges originating from exciton dissociation have been identified at the same wavelengths [102].

Here we use femtosecond (fs) optical pump-probe spectroscopy to track the dynamics of photoexcited excitons and charge carriers in few-layer WS_2 flakes obtained by LPE [56] and redispersed in poly(methyl methacrylate) (PMMA). The sample is photoexcited by a fs laser pulse (the pump) with a photon energy of 3.1 eV and a fluence of 200 $\mu J/cm^2$ and the transient transmission spectrum is recorded with a second (lower in intensity and broadband) fs laser pulse (the probe) at a well-defined delay after the pump. The measured signal is the relative change in transmission $\Delta T/T$, where a positive signal means photobleaching due to depopulation of the initial and population of the final states of an adsorptive transition, and a negative signal means photoinduced absorption, i.e. an increased absorption from populated excited states towards higher excited states. Scanning the pump-probe delay allows us to follow the evolution of the photoexcited states' population.

The advantages of using a sample containing an ensemble of flakes dispersed in an electronically inert transparent polymer compared to individual flakes are the ease of fabrication and handling [145] and the possibility to use far-field spectroscopic techniques without the need for high spatial resolution optical microscopy. A similar study on MoS_2 flakes embedded in PMMA showed [102], among others, that such samples display very similar photoexcitation dynamics to the more commonly studied individual few-layer flakes on a dielectric substrate [94], [210]. Additionally, different solvents for liquid exfoliation and different surfactant concentrations have very little influence on the photoexcitation dynamics in MoS_2 films [211]. Hence the results obtained on few-layer MoS_2 in PMMA can be safely compared with other studies and conclusions drawn from them can be extrapolated to flakes in different environments. By analogy, for WS_2, where very few time-resolved studies yet exist [109], [212], we propose the flake ensemble in PMMA as a prototype sample for few-layer WS_2.

4.1.2 Results and discussion

The extinction spectrum in Fig. 4.2 shows the characteristic A, B and C resonances at 1.97, 2.34, 2.72, and 3.05 eV, respectively. Recently, it has been shown how certain characteristics of the extinction spectrum of MoS_2 flakes dispersed in water + sodium cholate and size-selected by centrifugation can serve as a metric to determine the characteristic flake thickness and lateral size [117]. An analogous metric has subsequently been developed for WS_2 [118].

From the A exciton position and the ratio of the A exciton resonance and the ab-

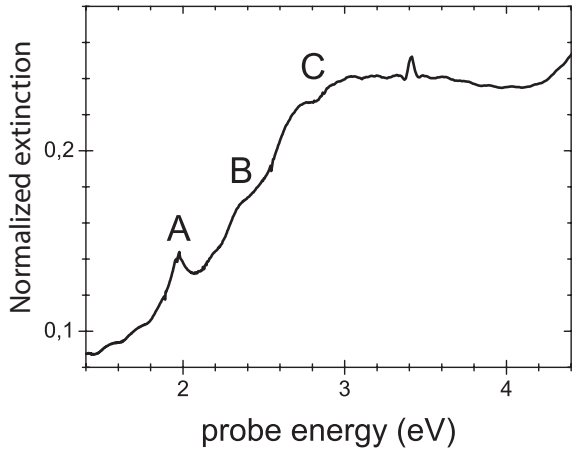


Figure 4.2: Extinction spectrum of few-layer WS_2 in PMMA. The different absorption resonances are labeled from A to C.

sorbance minimum around 4.2 eV, we obtain an average thickness of 7 layers and a characteristic lateral size of 200 nm (along the longer axis, with an average in-plane aspect ratio of 2). Please note that our samples are not as narrowly size-selected as those in Refs. [117] and [118] and hence contain a rather broad distribution of flake sizes, reaching far below 100 nm.

The femtosecond $\Delta T/T$ spectra show photobleaching (an increased transmission, Fig. 4.3 A, B) at the A, B, and C excitonic resonances superimposed on a structured photoinduced absorption that covers the whole measured spectral range (1.65-2.8 eV). During the first 10 ps the $\Delta T/T$ spectrum undergoes a characteristic change of shape: the positive signal components, which are formed within the instrumental resolution of ~ 100 fs, decay monotonically, while the main photoinduced absorption features show an initial instrument-limited rise followed by a delayed rise component and by a slower decay (see Fig. 4.4 A, B).

We now present a model that relates the evolution of the $\Delta T/T$ spectra to the photoexcitation dynamics. In section 2.2.4 we reached the expression:

$$\Delta\alpha(\omega,t) = \sum_i \Big(\sigma_i(\omega)\Delta N_i(\tau) + N_i\Delta\sigma(\omega,\tau)\Big) \tag{4.1}$$

$$T = I_0 e^{-\alpha(\omega)d} \tag{4.2}$$

with the index i denoting the ground state and the various excited state populations. The first term reflects the photoinduced changes in the populations. The second term represents changes in the absorption spectra as a consequence of photoexcitation, such as band gap renormalization [111], the Burstein–Moss effect [132], or Stark effect due to photoexcited charges [133], [213], [214]. All these effects are population dependent, so that the time dependence of $\sigma_i(\omega,t)$ also follows the time dependence of the photoexcited populations. In many cases the second term is either negligible - since it has the same time dependence as Δn- or indistinguishable from a contribution to the first term, and the data can be modeled without the second term [215]. Recently, however, the $\Delta T/T$ spectrum of monolayer MoS_2 300 fs after photoexcitation has been modeled inferring a shift of the ground state absorption as a consequence of band gap renormalization

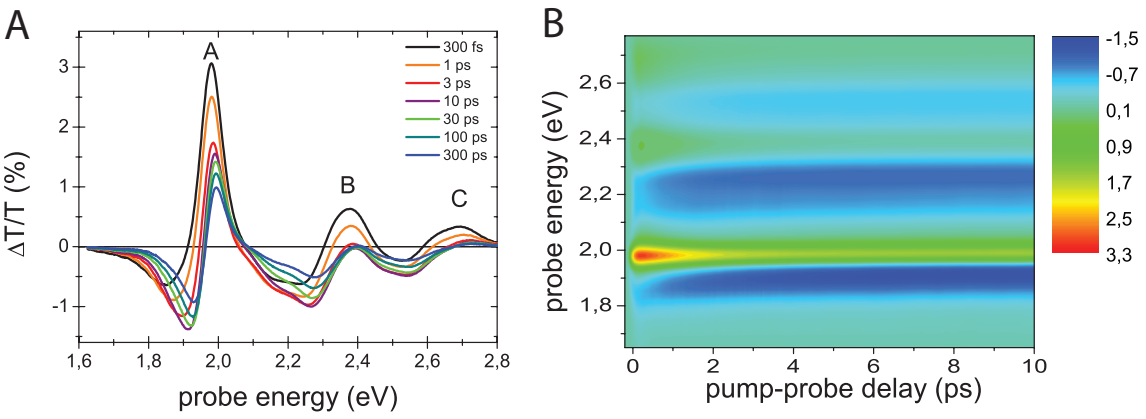


Figure 4.3: (A) $\Delta T/T$ spectra of WS_2 in PMMA at different delays. (B) Contour plot of the measured $\Delta T/T$ (in %).

as a main contribution to the signal [111]. Such a shift results in a derivative-shaped spectrum where positive and negative peaks have a common origin and should show the same time evolution.

As shown in Fig. 4.4, in our case the bleaching peaks form instantaneously, while the absorption peaks show a delayed rise, suggesting that they originate from two distinct photoexcited populations. The same behavior in few-layer MoS_2 has been modelled using only the first term of eqn 4.1, and the second term has been estimated to contribute less than 20% to the signal [102]. The photoexcitation dynamics has been modelled by assuming excitons as the primary photoexcitation species [102], which then dissociate into pairs of charges with the lifetime τ_1 (each lifetime, τ_i, can be calculated as the inverse of its correspondent time constant, $1/k_i$). In turn, the photogenerated charges recombine with a time constant τ_2:

$$\frac{dE(t)}{dt} = G(t) - k_1 E(t) \tag{4.3}$$

$$\frac{dC(t)}{dt} = k_1 E(t) - k_2 C(t) \tag{4.4}$$

With E and C being the time-dependent overall exciton (A, B, and C) and charge populations, respectively, and G(t) being the exciton generation term (pump-probe cross-correlation, approximated as a Gaussian pulse shape). The Pump pulse ($G(t)$) generates a population of excitons E. The excitons dissociate into charges (C) with a time constant k_1. Thus, few-layer MoS_2 displays a behaviour which is intermediate between conventional semiconductors, where at room temperature photoexcitation directly generates free carriers, and materials, such as organic semiconductors or carbon nanotubes, with high exciton binding energy for which the exciton dissociation is much less efficient than in few-layer MoS_2.

For WS_2, this remarkably simple model can coarsely reproduce the most salient characteristics of our result using $\tau_1 = 1.3$ ps and $\tau_2 = 100$ ps (Fig. 4.5 A and B), but is somewhat unsatisfactory in providing the details, in particular the first few ps in the range 1.8-2.2 eV. We obtain a much better agreement with the experimental data by adding two elements to the model: an intermediate state with population $I(t)$ between excitons and unbound charges, and a non-exponential recombination of the charges (Fig. 4.5 C):

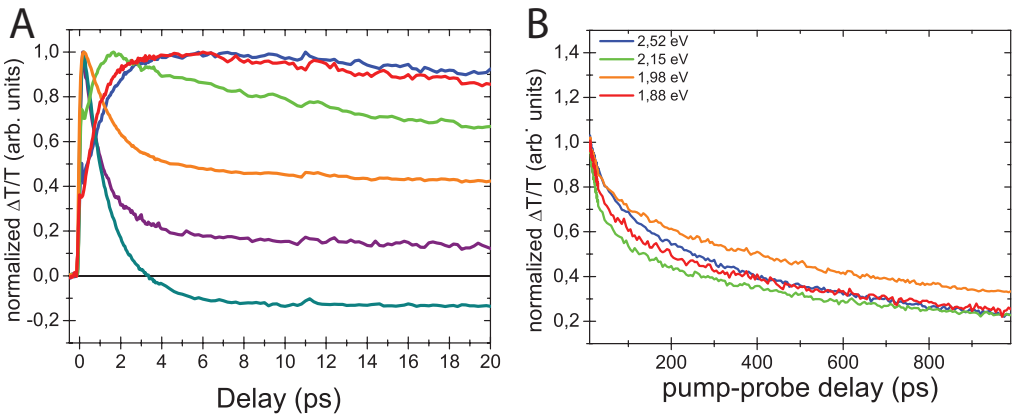


Figure 4.4: (A) and (B) Normalized time traces for different probe energies. In (A) traces are normalized to +1, in (B) traces are normalized to +1 at 10 ps.

$$\frac{dE(t)}{dt} = G(t) - k_1 E(t) \tag{4.5}$$

$$\frac{dI(t)}{dt} = k_1 E(t) - k_2 I(t) \tag{4.6}$$

$$\frac{dC(t)}{dt} = k_2 I(t) - r(t) \tag{4.7}$$

The non-exponential decay of the charge population denoted $r(t)$ could be due to non-geminate (i.e. bimolecular) recombination, in which case:

$$r(t) = \gamma C^2 \tag{4.8}$$

whith γ representing the rate constant for the recombination process or due to a distribution of relaxation times (e.g. different times for different flake thicknesses or lateral sizes). The detailed characterization of this mechanism would require measurements at different pump fluences and over a longer temporal window and is beyond the scope of this thesis. We find that excitons dissociate into the intermediate state with a time constant of $\tau_1 = 1.3$ ps, which evolves into the final charges with a time constant of $\tau_2 = 5.5$ ps. To fit the non-exponential long time charge relaxation, without any assumptions about the mechanism, we use a stretched exponential function.

$$r(t) \sim e^{-\left(\frac{\tau}{\tau_3}\right)^{\beta}} \tag{4.9}$$

with $\tau_3 = 450$ ps and $\beta = 0.3$. The spectral contributions, given as the oscillator strength in arbitrary units, include both the photoinduced absorption features of excitons and charges (shown as the negative oscillator strength in Fig. 4.6) and their contribution to the bleaching (as the positive oscillator strength). Any kind of excited state population causes a bleaching of all three exciton peaks in the measured range. Additionally, excitons and charges show several absorption peaks due to transitions towards higher excited states [27], [102], [216], [217], [218], (from excitons to higher (two-photon allowed) states and from charges to trions).

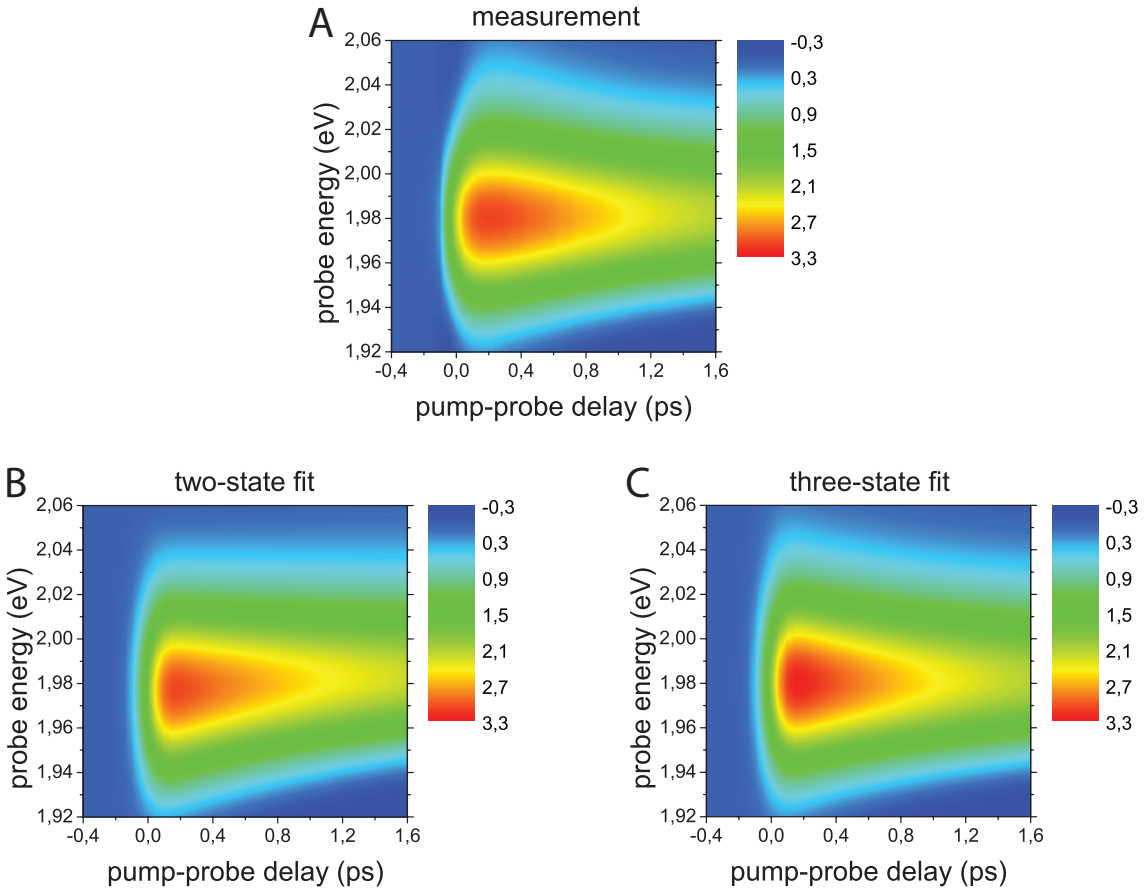


Figure 4.5: (A) Contour plot of the measured $\Delta T/T$ (in %) around A exciton. (B) Contour plot of the $\Delta T/T$ (in %) fitted with the two level model. (C) Contour plot of the $\Delta T/T$ (in %) fitted with the three level model.

The intermediate state spectrum (Fig. 4.6) deviates from the charges' spectrum only slightly, most pronouncedly in the region below 2.3 eV. This similarity suggests that the intermediate states are the charges originating from exciton dissociation, but in a different environment than the final charges. For example, upon exciton dissociation, the electrons and hole scatter away from the K points of the direct exciton and relax to their respective band minimum/maximum. However, such a relaxation typically occurs on a sub-ps time scale. [80], [219], [220] On the other hand, after exciton dissociation, the geminate electrons are still close enough to feel each other's electric field, which can cause a Stark shift and/or broadening of their spectra [133], [213], [214].

As they diffuse away from each other, this effect gradually diminishes until the field of the geminate counter-charge becomes a part of the background electric field of the whole charge population. Alternatively, initially free charges may get trapped at defects. Possibly such traps are heteroatoms, which are rather common in TMDCs of mineral origin, sulphur vacancies, islands of an additional layer, or flake edges. In both cases, τ_2 is a time scale that is associated with diffusion, either with the time that it takes for a charge to escape its counter-charge or the time to meet a trap. Assuming that charges follow a random walk after the exciton dissociation we can estimate the diffusion length l from the diffusion constant D and τ_2:

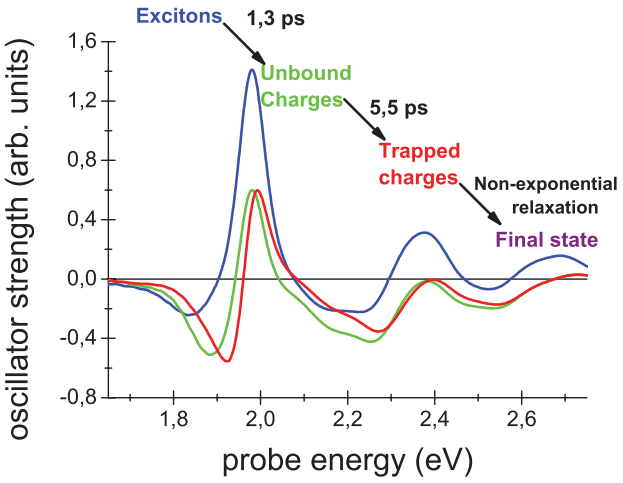


Figure 4.6: Spectral contribution of excitons (blue), free charges (green) and trapped charges (red).

$$D = \frac{\mu_e k_B T}{e} \tag{4.10}$$

$$l = \sqrt{D\tau_2} \tag{4.11}$$

Assuming a conservative estimate of $\mu_e = 10\ \mathrm{cm^2Vs^{-1}}$ for the room temperature charge mobility [221] in WS_2, we obtain $D = 0.25\mathrm{cm^2s^{-1}}$and $l = 10$ nm. However, the spatially averaged mobility from the electrical transport measurement is often dominated by defects and can be much lower than the local mobility probed by femtosecond spectroscopy. For example, in bulk MoS_2 $D = 18\mathrm{cm^2s^{-1}}$ has been measured over the first 50 ps of the charge recombination, followed by a slower regime of $D = 4\mathrm{cm^2s^{-1}}$ [97]. Similarly, in monolayer WSe2 $D = 15\mathrm{cm^2s^{-1}}$ has been obtained [104]. However, in the monolayer, exciton dissociation may be less efficient and hence the diffusion constant would be that of excitons rather than charge carriers. Since an exciton would have to scatter as a whole, its scattering cross section may be significantly lower than that of free carriers. Nevertheless, these D values, two orders of magnitude higher than in ref. [221], suggest that the diffusion length could be as high as 100 nm. Hence, with our broad distribution of flake sizes centered at 200 nm, flake edges are possible candidates for these traps. If we assume that the flake edges also trap excitons, this is consistent with the observed bright fluorescence from the edge of WS_2 monolayer triangles [185].

Eqn 4.5, 4.6 and 4.7, on which our fit is based, describe a cascade-like relaxation process, which conserves the overall population of excited states (see Fig. 4.7), except in the last step (due to the term -r(t)). However, we cannot a priori exclude additional processes besides those accounted for in our model, in particular loss mechanisms which do not conserve the excited state population, such as exciton-exciton annihilation or charge recombination. If such losses occur, then our model overestimates all subsequent populations in the cascade, which the fitting procedure compensates by proportionally underestimating the oscillator strength. Exciton dissociation into charges changes the kind of excited species, which have different spectra and oscillator strengths (the blue and green curves in Fig. 4.6). Trapping of charges, on the other hand, causes only a slight shift in the spectrum and should conserve the oscillator strength. By comparing the spectra

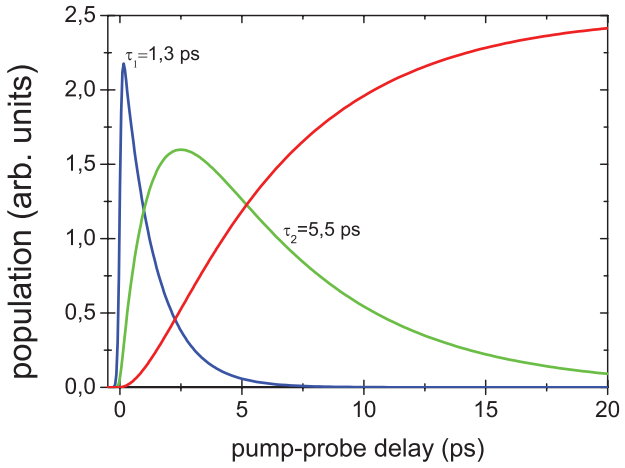


Figure 4.7: Time dependent exciton (blue), free charge (green) and trapped charge (red) population.

of free and trapped charges in Fig. 4.6, we find that our fit also conserves the oscillator strength and conclude that during the charge migration towards traps or edges no charges are lost by recombination. The final process that concludes the cascade is charge recombination. If this is the slow decay as observed in Fig. 4.4, then the last term in eqn 4.7 becomes

$$r(t) = \gamma C^2 \tag{4.12}$$

Since our temporal window is too short to reliably distinguish a quadratic term from the stretched exponential, we used it as a generic fit function. A study of this process would require intensity dependent measurements, beyond the scope of the present work.

Exciton–exciton annihilation, which has been observed [107], [109] could be relevant only while there is a significant exciton population, i.e. during the first few ps. Its presence would neither have any influence on the qualitative conclusions of this chapter nor on the quantitative estimates of the charge mobility and diffusion length.

4.1.3 Conclusions

In conclusion, we have applied femtosecond pump–probe spectroscopy to the study of the exciton and charge dynamics in few-layer WS_2. In agreement with previous observations on TMDCs, we find that the primary photoexcitation species are excitons which dissociate efficiently with a characteristic time of 1.3 ps. The better separation of the spectral features compared to MoS_2 allows us to resolve a previously undetected process: the carriers resulting from this dissociation then diffuse randomly away from their counter-charge, which results in a small but appreciable change of the $\Delta T/T$ spectrum, either due to the diminishing electric field from the countercharge or due to trapping on defects, such as flake edges. This spectral change allows one to monitor charge diffusion and trapping in the time domain. The different kinds of defects such as sulphur vacancies, dangling bonds, grain boundaries, or flake edges strongly influence the electronic and optical properties of TMDCs [222], [223]. For example, comparing samples with different flake or crystalline domain sizes can clarify under which circumstances grain boundaries and/or flake edges trap charges. For similar mobilities, shorter τ_2 is expected

for the smaller flakes/domains. Different types and densities of defects result from the many methods of synthesizing and exfoliating TMDCs. $1/l^2$ as determined from eqn 4.10 and 4.11 gives a measure of the trap density. Since different defects become active traps at different temperatures, measuring the temperature dependence of both the mobility and the photoexcitation dynamics maps the trap energy landscape and can elucidate their role in charge transport.

Chapter 5

Conclusions and Outlook

In summary, the work presented in this thesis is a modest contribution to the collective effort of the research community to the understanding of 2D materials' exfoliation and fundamental properties. A novel protocol for obtaining WS_2 flakes has been presented and applied in composite formation. The photoexcited state dynamics of few-layer WS_2 have been measured, modelled and interpreted.

PVA has been proven as an efficient stabilizer of WS_2 nanosheets. The nanosheets can be transferred to PVA or the process of exfoliation can be fully performed in the presence of PVA, avoiding surfactant residues. Centrifugation conditions and polymer concentration have been studied and optimized for maximizing the final monolayer volume fraction (V_f). Extinction, PL and Raman spectroscopy where proposed and proven as valid methods to quantify the monolayer V_f. PL was observable even in the starting stock dispersions, which allowed us to track it along all the steps of the process and ease the comparison between samples. Monolayer V_f as high as 5 % were obtained.

Water evaporation and WS_2 film formation were observed in real time. WS_2 nanosheets light emission spectrum broadens as the water evaporates but the global emission remains almost constant. This is related with the different level of doping between the sample in wet and dry state. As the PL is not quenched during drying, we can assume an efficient shielding of the flakes, which leads to a negligible reaggregation.

Composite formation was studied following two protocols, the standard and the freeze drying. The freeze dried polymer PL is retained at WS_2 loads as high as 10 wt% with an asymmetric broader spectrum. This polymer can be easily redispersed in water (sonic bath + shaking for 20–30 seconds) and the spectral features (extinction, PL and Raman) are recovered. The standard polymer is an homogeneous non scattering film suitable for future studies of SA or SHG and other nonlinear effects if the composite formation is done with a starting dispersion of higher monolayer content. The composites described might be useful for future light emitting devices such as LEDs or lasers.

Femtosecond pump-probe spectroscopy has been applied to study the photoexcited exciton and charge dynamics of few-layer WS_2. Excitons have been recognised as the primary photoexcited state. Excitons dissociate with a lifetime of 1.3 ps increasing the free carriers populations. Because of the bigger spectral distance between A and B exciton I have been able to identify some previously undetected processes (in MoS_2). Free carriers diffuse randomly escaping from their counter-charge. There is an appreciable change in the $\Delta T/T$ spectra, assigned either to diminishing of the electric field or to the trapping of charges in defects. The lifetime of this process is 5.5 ps, which may be in agreement with the edges being the main trapping mechanism. This spectral change allows one to monitor charge diffusion and trapping in the time domain. The different kinds of defects such as sulfur vacancies, dangling bonds, grain boundaries, or flake edges strongly in-

fluence the electronic and optical properties of TMDs. A deeper understanding on how defects affect diffusion of carriers will help us to understand the intrinsic limitations or advantages of these materials for optoelectronic applications.

The experimental procedures developed here are valid for following studies with different polymers. The importance of studying the drying process and the photoexcited state dynamics will be proven in the future. If devices made of nanosheets-polymer composites are fabricated, this knowledge can be crucial to optimize future devices.

Appendix A

Preliminary Work on Stabilization of WS_2 in Polymer/Solvent Dispersion

As previously mentioned, a succesful LPE depends on two phenomena, exfoliation and stabilization. Both of them can be studied as it was done in [145], but it requires a lot of work and, in the particular case of exfoliation in polymers/solvent dispersions, the results obtained for a polymer/solvent combination might not be comparable with others and results can even diverge for the same polymer/solvent combination but different polymer chain length (Eq. 2.55).

Keeping this in mind, a less exhaustive, but broader study was performed. The aim of this research was to study the stability of WS_2 flakes in different polymer/solvent combinations. As I only wanted to test stability, the sample was initially exfoliated in a known dispersion (water/SC dispersion) and afterwards transferred to the studied polymer/solvent combination.

The exfoliation procedure was as follows. A volume of 80 mL was filled with water and SC (C_{i0}= 8 g/L) and mixed with WS_2 (C_{WS_2}=30 g/L). It was sonicated with a 750 W sonic tip for 1 h in ice bath at 70% power. Dispersion was centrifuged at 2660 g. Supernatant was discarded and sedimented material was redispersed in 80 mL of water/SC dispersion (C_i= 2 g/L). This dispersion was exfoliated for 6 hours using the same sonic tip and the same conditions. Once the exfoliation finished, the dispersion was left unshaken over night. The supernatant was collected and centrifuged at 2660 g. We discarded the sediment and centrifuged the supernatant at 9740 g. The sediment was redispersed in water/SC dispersion (C_i= 2 g/L). Part of this sample was transferred to the chosen polymer/solvent combinations and part of it was kept as control sample.

Polystyrene (PS), Poly(methyl methacrylate)(PMMA) and Poly(vinyl alcohol) (PVA) were the chosen polymers for this study. PS and PMMA were dispersed in Tetrahydrofuran ($(CH_2)_4O$, commonly known as THF). The stability of exfoliated flakes was also tested in pure solvents such as NMP (N-Methyl-2-pyrrolidone), IPA, and THF, water and in water/Tx100 dispersion.

Before transferring the flakes to the new dispersion they were washed to remove surfactant and initial solvent:

1. Dispersion was centrifuged at high centrifugation speed (21700 g) for 60 minutes.

2. We have two different phases in the vial, a transparent supernatant that mainly contains water and surfactant and a black greenish/greyish mud sedimented in the bottom. The supernatant is discarded, the vial is refilled with fresh water and the material is redispersed.

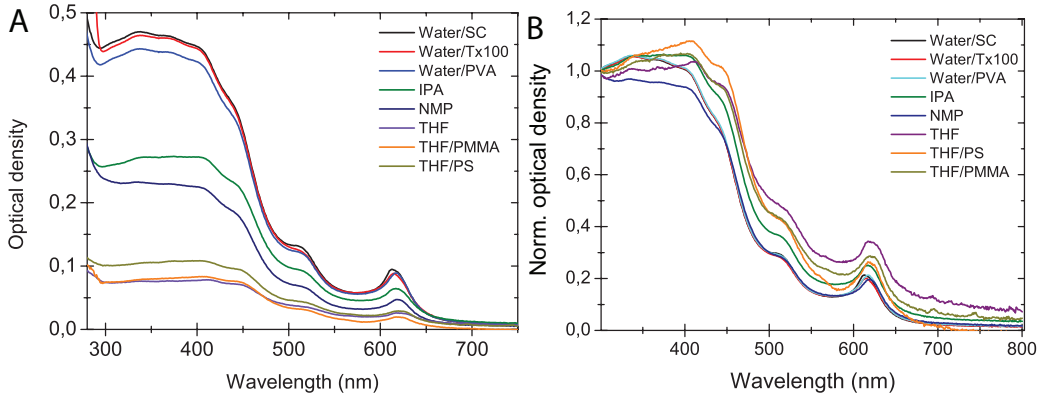


Figure A.1: (A) Extinction spectra of WS_2 flakes dispersed in different solvent and solvent/polymer dispersion. (B) Normalized extinction spectra of WS_2 flakes dispersed in different solvent and solvent/polymer dispersions (WS_2 flakes washed and redispersed in pure water were not stable and hence are not plotted).

3. The dispersion obtained in the previous step is centrifuged again at 21700 g for 60 minutes.
4. Supernatant is removed again and discarded.
5. Deposited material is now redispersed in a pure solvent which is miscible with the previous (water) and the final one, NMP, IPA, THF and water, for the first three, ethanol is chosen as intermediate solvent and for the water we keep using water as intermediate solvent.
6. Previous dispersion is centrifuged at 21700 g for 60 minutes.
7. Supernatant is discarded and the sedimented flakes are redispersed in the final solvent or solvent/polymer dispersion.

A first and fast way to characterize our material is via Extinction and PL spectroscopy. A previous report [117] links the shape of extinction spectra with the lateral size. It also stated that sample concentration doesn't modify extinction spectra shape. Then, assuming that all our samples have similar extinction shape, a direct observation of the concentration can be done by measuring extinction spectra. From photoluminescence measurements the presence of monolayers in the dispersion can be tracked.

It is clear from Fig. A.1 A that the starting dispersion is the one with higher concentration. There is a negligible reduction of the concentration in the sample transferred to water/Tx100. This small reduction might not be related with a worse stability but with some lost material during washing. Water/PVA dispersion can hold a concentration of WS_2 flakes slightly smaller than Water/SC and Water/Tx100 but still significantly larger than IPA, NMP, THF and THF/PMMA and THF/PMMA.

Among the three samples where THF is present it can be seen that PS positively modifies the solubility of WS_2 in THF, while PMMA does not seem to modify it.

If we plot the normalized extinction spectra (Fig. A.1 B), we cannot identify main changes in extinction spectra shape of the samples Water/SC, Water/Tx100, Water/PVA and NMP. This is telling us that, for these samples, there is no reaggregation in the transfer process and the histograms (in terms of lateral size and thickness) do not suffer significant changes. The changes in the spectra of the other samples do not suffer a change

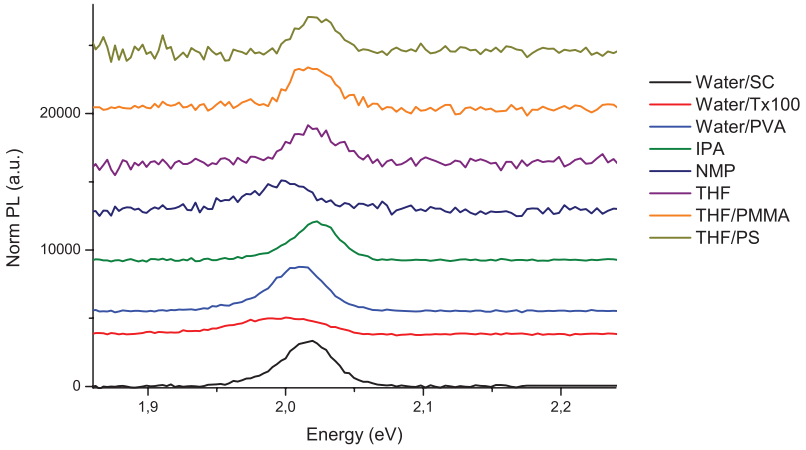


Figure A.2: Normalized PL of the different samples with respect to their absorption at the excitation wavelength (435 nm).

as strong as those present in Fig. 3.9 A between the thicker and the thinner sample but they are comparable with the changes experimented in the spectra of samples between large and small samples of Fig. 3.2, hence there is some partial reaggregation.

PL is a technique that gives more accurate information about the presence of WS_2 monolayers in the dispersions. The PL spectra have been normalized with respect to the absorption at the excitation wavelength (λ_{exc}= 435 nm) (Fig. A.2) in order to estimate the light emission efficiency and hence the monolayer content.

From the area of the PL peak the light emission efficiency can be obtained. Two species contribute to the emission, the excitons, centred at ~ 2 eV, and the trions, centred at ~ 1.96 eV. The spectra of the samples transferred to THF or THF/polymer were nicely fitted with just exciton contribution to light emission. That would indicate that the flakes are less doped in this environment. The fitting of the normalized PL spectra of flakes transferred to NMP and IPA gives comparable areas but different exciton/trion contribution. The PL of flakes dispersed in water/Tx100 is partially quenched and broader (stronger trion contribution).

The sample with a higher normalized area is the flakes dispersed in water/PVA. This same sample has mainly excitonic emission. By combining this result with its high concentration indicates that PVA dispersed in water is the most promising dispersion (among those tested) for exfoliation in liquid phase and composite formation.

Table A.1: Fitted parameters for each sample.

Sample	$E_{Exciton}$	E_{trion}	$A_{Exciton}$	A_{trion}	A_{total}
Water/SC	2.016	1.976	147.7	15.02	162.72
Water/Tx100	1.999	1.953	76.19	23.75	99.94
Water/PVA	2.010	1.966	147.5	23.4	170.9
NMP	2	1.93 6	121.4	10.60	132
IPA	2.02	1.99	71.6	52.4	124
THF	2.02		110		110
THF/PS	2.019		134		134
THF/PMMA	2.02		89.75		75

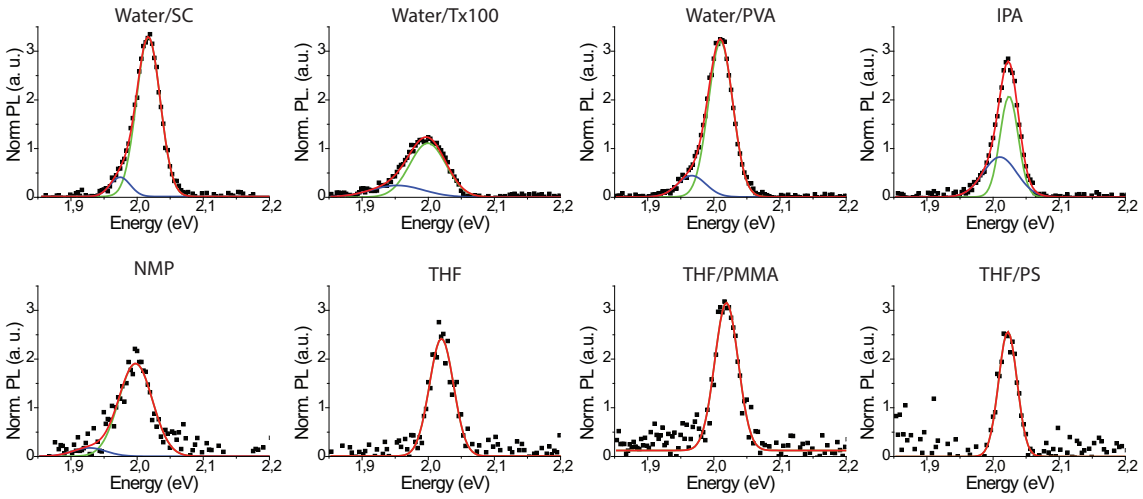


Figure A.3: Fitted PL spectra for different samples.

Appendix B

Suplementary Information for Exfoliation of WS_2 in PVA/Water Dispersion

B.1 Extinction Coefficient of WS_2

Since optical extinction spectra of liquid exfoliated TMDCs are known to change as function of size and thickness [117], it is important to determine size-dependent extinction coefficients to accurately measure the nanosheet concentration. To do this, we have prepared a number of WS_2 dispersions with varying sizes and thicknesses by changing post-exfoliation centrifugation conditions similar to the procedure described in the methods section of the main manuscript and measured optical extinction spectra. The concentration of WS_2 was then determined by filtration and weighing (alumina membranes pore size 0.02 μm). Prior to weighing, the samples were washed with 600 mL of deionised

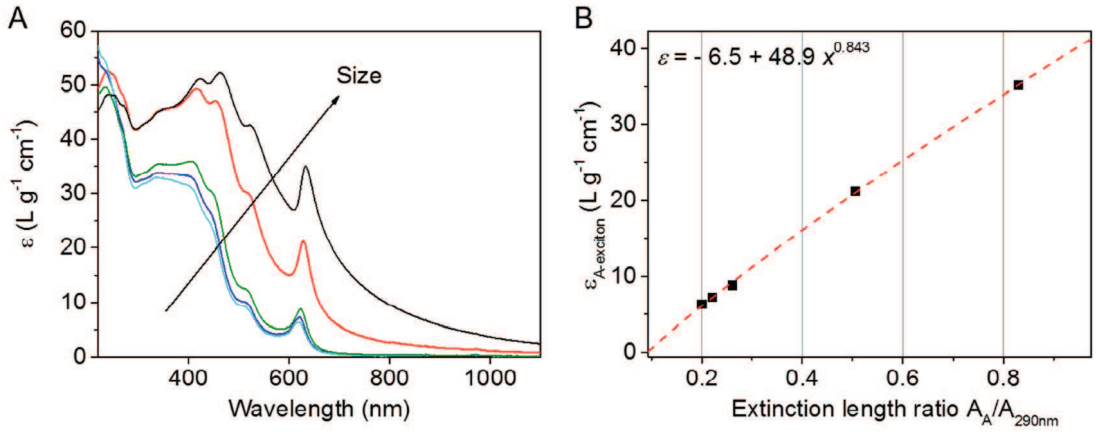


Figure B.1: (A) Extinction coefficient spectra of WS_2 exfoliated in an aqueous solution of sodium cholate for different mean nanosheet sizes and thicknesses. (B) Extinction coefficient at the A exciton as a function of extinction peak intensity ratio at the A exciton / 290 nm. The dashed line is a fit according to the equation present in the top left corner of (B).

water and dried in vacuum at 70°C. Thus determined concentration was used to convert the extinction spectra to coefficient spectra as shown in fig. B.1 A. We note that this procedure was carried out using sodium cholate as surfactant and not PVA, as the polymer is more difficult to remove and would thus result in an overestimation of the weighed mass.

The extinction coefficient spectra show pronounced changes as a function of nanosheet size. As outlined previously for MoS_2 [117] and discussed in Chapter 3, the nanosheet size and changes in extinction spectra due to size effects can be expressed as extinction intensity ratio. For WS_2 we use the intensity at the A-exciton/290 nm. In fig. B.1 B we plot the extinction coefficient at the A-exciton as a function of this peak intensity ratio. This gives the size dependent extinction coefficient at the A-exciton which can be used to determine nanosheet concentrations for samples with unknown size.

B.2 Fitted PL Spectra of LPE WS_2-PVA on Drying

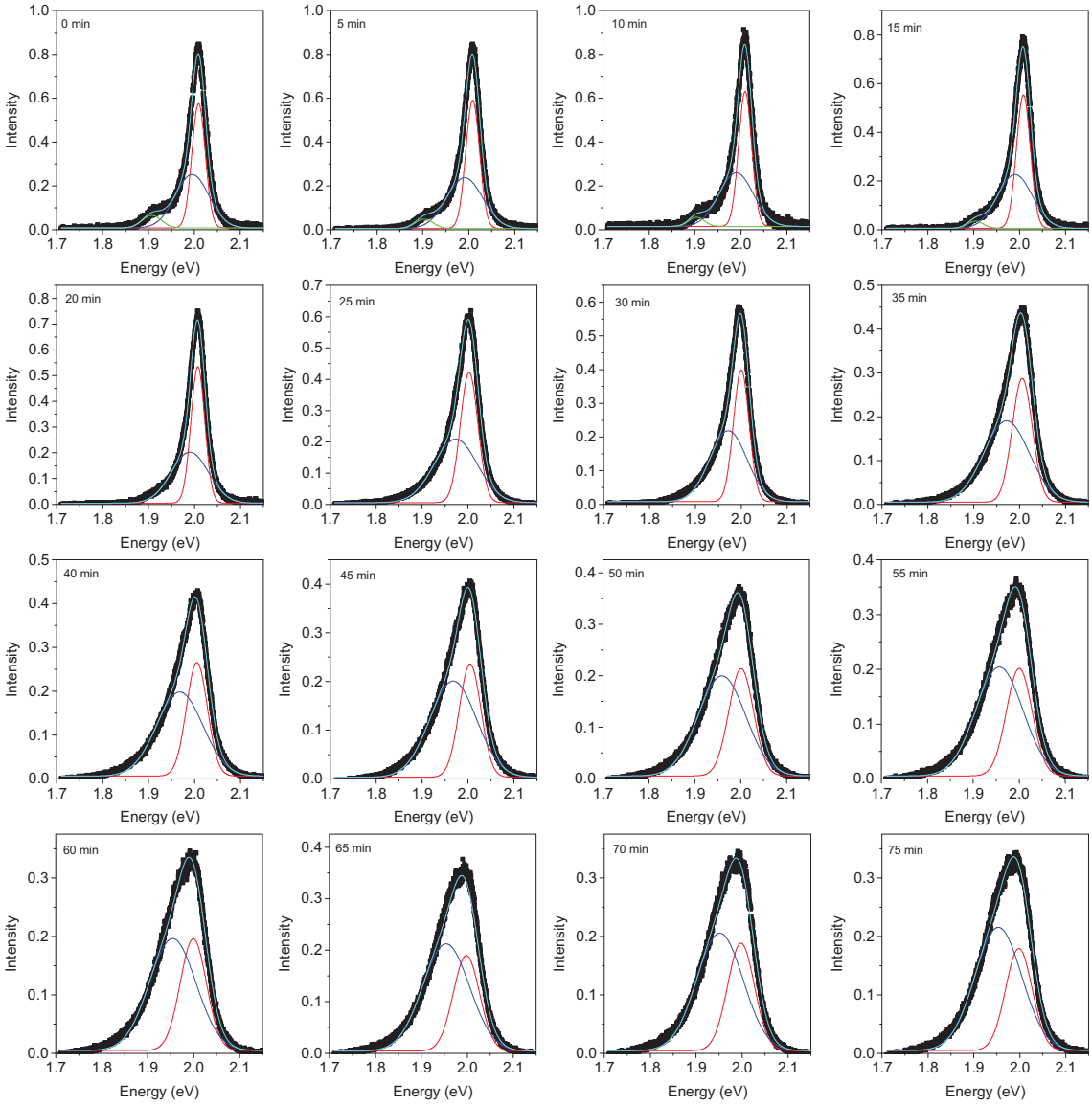


Figure B.2: PL spectra of LPE WS_2-PVA for different times of drying a liquid drop. Times are indicated as figure legend. The data was fit to Gaussian lineshapes for exciton (red), trion (blue) and water (green, only for 0, 5, 10 and 15 min) as exemplarily shown for two cases in Fig. 3.11 C of Chapter 3.

B.3 Effect of PVA on Optical Properties of CVD-WS_2

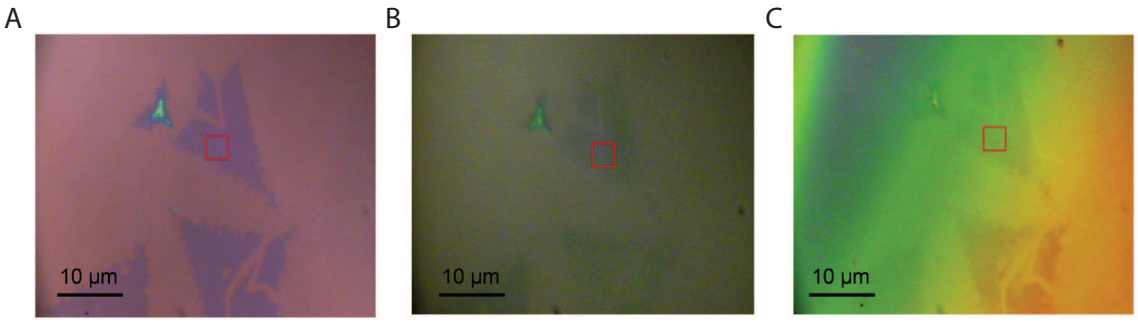


Figure B.3: A) before deposition of a drop of PVA, B) with the deposited drop and C) after drying the drop. The red square indicated the sample region the spectra were acquired from.

In order to test whether changes in the PL intensity and width observed on drying the LPE WS_2-PVA dispersion occur due to changes in the dielectric constant and potential doping, we have analysed the Raman/PL spectra of vapour-grown monolayer WS_2. To have a valid comparison, it is important to measure the same sample region prior to deposition of a liquid drop of PVA (C_{PVA}= 2 g/L), after deposition of the drop and after drying of the drop. The optical micrographs B.3 show that this was indeed the case. The red square indicates the sample region the spectra were acquired from.

The corresponding spectra normalised to the 2LA(M) Raman mode are displayed in B.4. The WS_2 PL broadens and becomes lower in intensity when a drop of PVA is de-

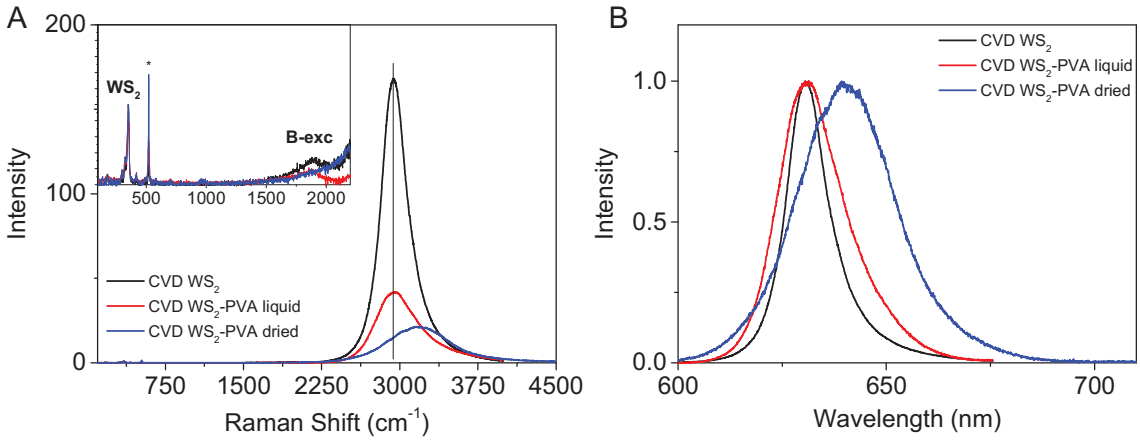


Figure B.4: Raman/PL spectra of CVD-WS_2 before and after the deposition of PVA on the surface. (A) Raman/PL spectra normalized to the 2LA(M) Raman mode showing the PL broadening and reduced intensity. Inset: Raman modes. The mode at 521 cm^{-1} marked with the asterisk is due to the Si/SiO2 substrate. (B) Normalized PL spectra to visualize broadening and red-shifting after evaporation of the water.

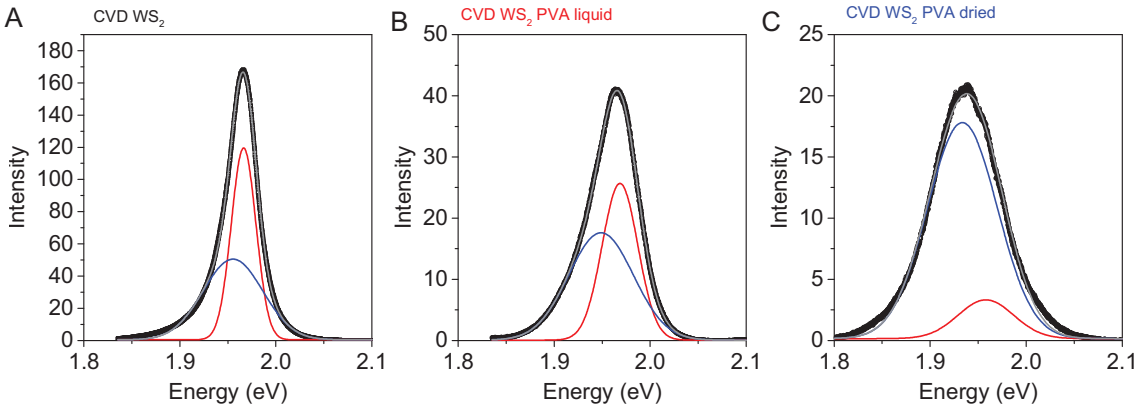


Figure B.5: Fitted PL spectra (to two Gaussians) of CVD-WS_2 in (A) air, (B) with a liquid drop of PVA (2 g/L) deposited and (C) after drying the drop. Fit parameters are summarised in table S1.

posited on the surface suggesting an increased n-type doping [190]. Similar to the LPE WS_2, this becomes more pronounced as the drop of PVA is dried presumably because the water in the vicinity of the WS_2 is p-type doping the nanosheets [192] partly compensating the n-type doping effect of the PVA in liquids.

Similar to the data shown in Chapter 3, the PL can be fit to two Gaussians attributed to exciton and trion emission. The fitted spectra are shown in fig. B.5 and fit values are summarised in table B.1. We note that we used Gaussian functions to fit the data for consistency even though a Lorentzians lineshape would probably describe the exciton more accurately in the case of an individual nanosheet (opposed to the ensemble probed in the case of the LPE WS_2). Fits to two Lorentians did not describe the data well especially after deposition of the PVA. We suspect that at least the trion has to be fit to a Gaussian lineshape due to inhomogeneous broadening from doping. Interestingly, the trion/exciton ratio increases as a drop of water/PVA is deposited suggesting an increase in n-type doping in the presence of the PVA. This is more pronounced after the drop has dried and reflected in broadening and red-shifting of both exciton and trion emission as well as an increased trion/exciton ratio. Unfortunately, only relative and no absolute peak intensities can be compared, as it is difficult to maintain the same focus on the sample area. In addition, it should be noted that the same trend is observed as in the LPE nanosheets, but absolute values of peak positions and trion/exciton ratios cannot be compared to liquid-exfoliated WS2 due to the interaction of the CVD grown WS2 with the Si/SiO2 substrate [207].

Table B.1: Tabulated data of the fit components of Fig. B.5 showing energy (E), width (w) and area (A) of the exciton and trion, respectively, as well as the trion/exciton ratios.

	$E_{exciton}$ (eV)	$w_{exciton}$ (meV)	$A_{exciton}$	E_{trion} (eV)	w_{trion} (meV)	A_{trion}	$A_{trion}/Aexciton$
Air	1.996	30	3.83	1.955	73	3.9	1.02
PVA liquid	1.968	43	1.19	1.949	79	1.48	1.24
PVA dried	1.958	68	0.23	1.933	86	1.61	7

B.4 As Recorded Raman Spectra of WS_2-PVA Composites

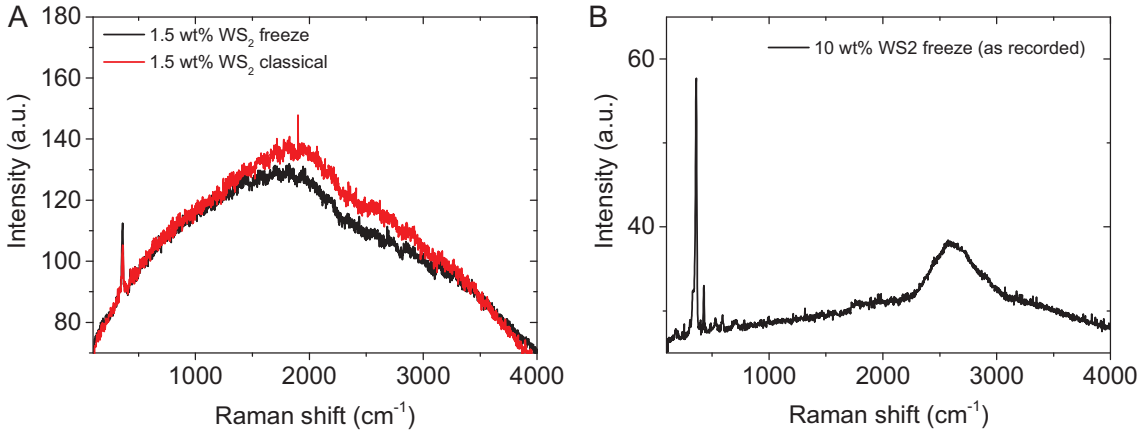


Figure B.6: As-recorded Raman spectra of the WS_2-PVA composites. (A) Freeze-dried and classical composite with 1.5 wt% of WS_2. Due to the low loading level, the spectral features of WS_2 are difficult to resolve and despite the low laser power (0.2 mW), the pronounced heating background masks any potential PL features. (B) As recorded spectrum of the freeze-dried composite with 10 wt% of WS_2 loading recorded under equal measurement parameters as in (A). Some residual heating background is still observed for the higher WS_2 loading level, but the PL can clearly be detected. The corresponding spectrum in Chapter 3 was obtained after subtracting the background.

There are certain observations that lead us to suggest heating as the effect behind the broad/strong background of Fig. B.6

1. Such a broad spectra was visible just when the flakes were embedded in polymer and in dry state. We didn't observed it neither under the presence of polymer in dispersion (liquid) nor in dryed flakes without polymer presence.

2. That background rose as the excitation laser power grew, till a hole or a burn spot was observed.

3. PVA has a really low thermal conductivity.

References

[1] K. D. Sattler, *Handbook of nanophysics: Nanoparticles and quantum dots*. London, UK: CRC Press, 2010.

[2] (2016). Damascus steel blade, [Online]. Available: https://es.wikipedia.org/wiki/Acero_de_Damasco (visited on 2016).

[3] M. Reibold, P. Paufler, A. A. Levin, W. Kochmann, N. Pätzke, and D. C. Meyer, "Carbon nanotubes in an ancient damascus sabre," *Nature*, vol. 444, no. 7117, p. 286, 2006.

[4] M. Faraday, "The bakerian lecture: Experimental relations of gold (and other metals) to light," *Phil. Trans. R. Soc. Lon*, vol. 147, pp. 145–181, 1857.

[5] (1959). Feynman speech at the american physical society meeting at caltech, [Online]. Available: http://glab.caltech.edu/doc/rf.pdf (visited on 2016).

[6] (2016). Faraday microscope glass slide., [Online]. Available: http://www.sites.hps.cam.ac.uk/whipple/explore/microscopes/faradaysslide/ (visited on 2016).

[7] R. M. Bozorth, "The crystal structure of cadmium iodide," *J. Am. Chem. Soc.*, vol. 44, no. 10, p. 2232, 1922.

[8] R. Dickinson and L. Pauling, "The crystal structure of molybdenite," *J. Am. Chem. Soc.*, vol. 45, no. 6, p. 1466, 1923.

[9] L. Pauling, "The structure of the chlorites," *Proc. N. A. S.*, vol. 16, no. 9, pp. 578–582, 1930.

[10] T. F. Bates, L. B. Sand, and J. F. Mink, "Tubular crystals of chrysotile asbestos," *Science*, vol. 111, no. 2889, pp. 512–513, 1950.

[11] M. Remskar, "Inorganic nanotubes," *Adv. Mater.*, vol. 16, no. 17, pp. 1497–1504, 2004.

[12] R. Tenne, L. Margulis, M. Genut, and G. Godes, "Polyhedral and cylindrical structuresof tungsten disulfide," *Nature*, vol. 360, no. 6403, pp. 444–446, 1992.

[13] H. W. Kroto, J. R. Heath, S. C. O'Brien, R. F. Curl, and R. E. Smalley, "C_{60}: Buckminsterfullerene," *Nature*, vol. 318, no. 6042, pp. 162–163, 1985.

[14] K. S. Novoselov, A. K. Geim1, S. V. Morozov, D. Jiang, Y. Zhang, S. V. Dubonos, I. V. Grigorieva, and A. A. Firsov, "Electric field effect in atomically thin carbon films," *Science*, vol. 306, no. 5696, pp. 666–669, 2004.

[15] Y. Ding, Y. Wang, J. Ni, L. Shi, S. Shi, and W. Tang, "First principles study of structural, vibrational and electronic properties of graphene-like mx2 (m=mo, nb,w,ta;x=s, se,te) monolayers," *Phys. B*, vol. 406, no. 11, pp. 2254–2260, 2011.

[16] A. D. Yoffe, "Electronic properties of low dimensional solids: The physics and chemistry of layered tipe transitionmetal dichalcogenides and their intercalate complexes," *Solid state ionics*, vol. 39, no. 1, pp. 1–7, 1990.

[17] Z. M. Wang, *MoS_2 materials, physics, and devices*. Springer Berlin Heidelberg New York: Springer, 2014.

[18] D. Yang, S. J. Sandoval, W. M. R. Divigalpitiya, J. C. Irwin, and R. D. Frindt, "Structure of single-molecular-layer MoS_2," *Phys. Rev. B*, vol. 43, no. 14, pp. 12 053–12 056, 1991.

[19] Q. H. Wang, K. Kalantar-Zadeh, A. Kis, J. N. Coleman, and M. S. Strano, "Electronics and optoelectronics of two-dimensional transition metal dichalcogenides," *Nature Nanotech.*, vol. 7, no. 11, pp. 699–713, 2012.

[20] B. Radisavljevic, A. Radenovic, J. Brivio, V. Giacometti, and A. Kis, "Single-layer MoS_2 transistors," *Nature Nanotech.*, vol. 6, no. 3, pp. 147–150, 2011.

[21] N. Kumar, S. Najmaei, Q. Cui, F. Ceballos, P. M. Ajayan, J. Lou, and H. Zhao, "Second harmonic microscopy of monolayer MoS_2," *Phys. Rev. B*, vol. 87, no. 16, p. 161 403, 2013.

[22] Y. Li, Y. Rao, K. F. Mak, Y. You, S. Wang, C. R. Dean, and T. F. Heinz, "Probing symmetry properties of few-layer MoS_2 and h-BN by optical second-harmonic generation," *Nano Lett.*, vol. 13, no. 7, pp. 3329–3333, 2013.

[23] C. Janisch, Y. Wang, D. Ma, N. Mehta, A. L. Elías, N. Perea-López, M. Terrones, V. Crespi, and Z. Liu, "Extraordinary second harmonic generation in tungsten disulfide monolayers," *Sci. Rep.*, vol. 4, p. 5530, 2014.

[24] R. A. Bromley, "A semi-empirical tight-binding calculation of the band structure of MoS_2," *Phys. Rev. Lett. A*, vol. 33, no. 4, pp. 242–243, 1970.

[25] D. R. Edmondson, "Electronic band structure of the layer-type crystal 2H-MoS_2," *Solid State Commun.*, vol. 10, no. 11, pp. 1085–1088, 1972.

[26] J. K. Ellis, M. J. Lucero, and G. E. Scuseria, "The indirect to direct band gap transition in multilayered MoS_2 as predicted by screened hybrid density functional theory," *Apl. Phys. Lett.*, vol. 99, no. 26, p. 261 908, 2011.

[27] T. Cheiwchanchamnangij and W. R. L. Lambrecht, "Quasiparticle band structure calculation of monolayer, bilayer, and bulk MoS_2," *Phys. Rev. B*, vol. 85, no. 20, p. 205 302, 2012.

[28] A. Splendiani, L. Sun, Y. Zhang, T. Li, J. Kim, C.-Y. Chim, G. Galli, and F. Wang, "Emerging photoluminescence in monolayer MoS_2," *Nano Lett.*, vol. 10, no. 4, pp. 1271–1275, 2010.

[29] W. Zhao, Z. Ghorannevis, L. Chu, M. Toh, C. Kloc, P.-H. Tan, and G. Eda, "Evolution of electronic structure in atomically thin sheets of WS_2 and WSe_2.," *ACS Nano*, vol. 7, no. 1, pp. 791–797, 2013.

[30] Z. Ye, T. Cao, K. O'Brien, H. Zhu, X. Yin, Y. Wang, S. G. Louie, and X. Zhang, "Probing excitonic dark states in single-layer tungsten disulphide," *Nature*, vol. 513, no. 7571, pp. 214–218, 2014.

[31] A. Chernikov, T. C. Berkelbach, H. M. Hill, A. Rigosi, Y. Li, O. B. Aslan, D. R. Reichman, M. S. Hybertsen, and T. F. Heinz, "Exciton binding energy and nonhydrogenic Rydberg series in monolayer WS_2," *Phys. Rev. Lett.*, vol. 113, no. 7, p. 076 802, 2014.

[32] H. M. Hill, A. F. Rigosi, C. Roquelet, A. Chernikov, T. C. Berkelbach, D. R. Reichman, M. S. Hybertsen, L. E. Brus, and T. F. Heinz, "Observation of excitonic Rydberg states in monolayer MoS_2 and WS_2 by photoluminescence excitation spectroscopy," *Nano Lett.*, vol. 15, no. 5, pp. 2992–2997, 2015.

[33] A. Castellanos-Gomez, L. Vicarelli, E. Prada, J. O. Island, K. L. Narasimha-Acharya, S. I. Blanter, D. J. Groenendijk, M. Buscema, G. A. Steele, and J. V. Alvarez, "Isolation and characterization of few-layer black phosphorus," *2D Mater.*, vol. 1, no. 2, p. 025 001, 2014.

[34] J. F. Sánchez-Royo, G. Muñoz-Matutano, M. Brotons-Gisbert, J. P. Martínez-Pastor, A. Segura, A. Cantarero, and R. Mata, "Electronic structure, optical properties and lattice dynamics in atomically thin indium selenide flakes," *Nano Res.*, vol. 7, no. 10, pp. 1556–1568, 2014.

[35] C. Lee, X. Wei, J. W. Kysar, and J. Hone, "Measurement of the elastic properties and intrinsic strength of monolayer graphene," *Science*, vol. 321, no. 5887, pp. 385–388, 2008.

[36] A. Castellanos-Gomez, M. Poot, G. A. Steele, H. S. J. van der Zant, N. Agrait, and G. Rubio-Bollinger, "Elastic properties of freely suspended MoS_2 nanosheets," *Adv. Mater.*, vol. 24, no. 6, pp. 772–775, 2012.

[37] S. Bertolazzi, J. Brivio, and A. Kis, "Stretching and breaking of ultrathin MoS_2," *ACS Nano.*, vol. 5, no. 12, pp. 9703–9709, 2011.

[38] Y. Zhao, X. Luo, H. Li, J. Zhang, P. T. Araujo, C. K. Gan, J. Wu, H. Zhang, S. Y. Quek, M. S. Dresselhaus, and Q. Xiong, "Interlayer breathing and shear modes in few-trilayer MoS_2 and WSe_2," *Nano Lett.*, vol. 13, no. 3, pp. 1007–1015, 2013.

[39] C. Lee, H. Yan, L. E. Brus, T. F. Heinz, J. Hone, and S. Ryu, "Anomalous lattice vibrations of single and few-layer MoS_2," *ACS Nano.*, vol. 4, no. 5, pp. 2695–2700, 2010.

[40] H. Li, Q. Zhang, C. C. R. Yap, B. K. Tay, T. H. T. Edwin, A. Olivier, and D. Baillargeat, "From bulk to monolayer MoS_2: Evolution of Raman scattering," *Adv. Funct. Mater.*, vol. 22, no. 7, pp. 1385–1390, 2012.

[41] A. Berkdemir, H. R. Gutiérrez, A. R. Botello-Mendez, N. Perea-Lopez, A. L. Elias, C.-I. Chia, B. Wang, V. H. Crespi, F. Lopez-Urias, J.-C. Charlier, H. Terrones, and M. Terrones, "Identification of individual and few layers of WS_2 using Raman spectroscopy," *Sci. Rep.*, vol. 3, p. 1755, 2013.

[42] X. Zhang, X.-F. Qiao, W. Shi, J.-B. Wu, D.-S. Jiang, and P.-H. Tan, "Phonon and Raman scattering of two-dimensional transition metal dichalcogenides from monolayer, multilayer to bulk material," *Chem. Soc. Rev.*, vol. 44, no. 9, pp. 2757–2785, 2015.

[43] A. Nipane, D. Karmakar, N. Kaushik, S. Karande, and S. Lodha, "Few layer MoS_2 p-type devices enabled by selective doping using low energy phosphorus implantation," *ACS Nano*, vol. 10, no. 2, pp. 2128–2137, 2016.

[44] M. Thripuranthaka and D. J. Late, "Temperature dependent phonon shifts in single-layer WS_2," *ACS Appl. Mater. Interfaces*, vol. 6, no. 2, pp. 1158–1163, 2014.

[45] C. Rice, R. J. Young, R. Zan, and U. Bangert, "Raman-scattering measurements and first-principles calculations of strain-induced phonon shifts in monolayer MoS_2," *Phys. Rev. B*, vol. 87, no. 8, p. 081 307, 2013.

[46] A. Castellanos-Gomez, M. Barkelid, A. M. Goossens, V. E. Calado, H. S. J. van der Zant, and G. A. Steele, "Laser-thinning of MoS_2: On demand generation of a single-layer semiconductor," *Nano Lett.*, vol. 12, no. 6, pp. 3187–3192, 2012.

[47] X. Lu, M. I. Utama, J. Zhang, Y. Zhao, and Q. Xiong, "Layer-by-layer thinning of MoS_2 by thermal annealing," *Nanoscale*, vol. 5, no. 19, pp. 8904–8908, 2013.

[48] V. Nicolosi, M. Chhowalla, M. G. Kanatzidis, M. S. Strano, and J. N. Coleman, "Liquid exfoliation of layered materials," *Science*, vol. 340, no. 6139, p. 1 226 419, 2013.

[49] L. Dong, S. Lin, L. Yang, J. Zhang, C. Yang, D. Yanga, and H. Lu, "Spontaneous exfoliation and tailoring of MoS_2 in mixed solvents," *Chem. Commun.*, vol. 50, no. 100, pp. 15 936–15 939, 2014.

[50] C.-J. Shih, A. Vijayaraghavan, R. Krishnan, R. Sharma, J.-H. Han, M.-H. Ham, Z. Jin, S. Lin, G. L. P. and Nigel Forest Reuel, Q. H. Wang, and D. B. and Michael S. Strano, "Bi- and trilayer graphene solutions," *Nature Nanotech.*, vol. 6, no. 7, pp. 439–445, 2011.

[51] X. Fan, P. Xu, D. Zhou, Y. Sun, Y. C. Li, M. A. T. Nguyen, M. Terrones, and T. E. Mallouk, "Fast and efficient preparation of exfoliated 2H MoS_2 nanosheets by sonication-assisted lithium intercalation and infrared laser-induced 1T to 2H phase reversion," *Nano lett.*, vol. 15, no. 9, pp. 5956–5960, 2015.

[52] Y. Hernandez, V. Nicolosi, M. Lotya, F. M. Blighe, Z. Sun, S. De, I. T. McGovern, B. Holland, M. Byrne, Y. K. Gun'Ko, J. J. Boland, P. Niraj, G. Duesberg, S. Krishnamurthy, R. Goodhue, J. Hutchison, V. Scardaci, A. C. Ferrari, and J. N. Coleman, "High-yield production of graphene by liquid-phase exfoliation of graphite," *Nature Nanotech.*, vol. 3, no. 9, pp. 563–568, 2008.

[53] M. M. Alsaif, S. Balendhrana, M. R. Fieldb, K. Lathamb, W. Wlodarskia, J. Z. Oua, and K. Kalantar-zadeh, "Two dimensional α-MoO_3 nanoflakes obtained using solvent-assisted grinding and sonication method: Application for H_2 gas sensing," *Sens. Actuator B: Chem.*, vol. 192, pp. 196–204, 2014.

[54] D. Hanlon, C. Backes, T. M. Higgins, M. Hughes, A. O'Neill, P. King, N. McEvoy, G. S. Duesberg, B. M. Sanchez, H. Pettersson, V. Nicolosi, and J. N. Coleman, "Production of molybdenum trioxide nanosheets by liquid exfoliation and their application in high-performance supercapacitors," *Chem. Mater*, vol. 26, no. 4, pp. 1751–1763, 2014.

[55] E. Varrla, C. Backes, K. R. Paton, A. Harvey, Z. Gholamvand, J. McCauley, and J. N. Coleman, "Large-scale production of size-controlled MoS_2 nanosheets by shear exfoliation," *Chem. Mater.*, vol. 27, no. 3, pp. 1129–1139, 2015.

[56] J. N. Coleman, M. Lotya, A. O'Neill, S. D. Bergin, P. J. King, U. Khan, K. Young, A. Gaucher, S. De, R. J. Smith, I. V. Shvets, Suni, K. Arora, G. Stanton, H.-Y. Kim, K. Lee, G. T. Kim, G. S. Duesberg, T. Hallam, J. J. Boland, J. J. Wang, J. F. Donegan, J. C. Grunlan, G. Moriarty, A. Shmeliov, R. J. Nicholls, J. M. Perkins, E. M. Grieveson, K. Theuwissen, D. W. McComb, P. D. Nellist, and V. Nicolosi, "Two-dimensional nanosheets produced by liquid exfoliation of layered materials," *Science*, vol. 331, no. 6017, pp. 568–571, 2011.

[57] K. G. Zhou, N. N. Mao, H. X. Wang, Y. Peng, and H. L. Zhang, "A mixed-solvent strategy for efficient exfoliation of inorganic graphene analogues.," *Angew.Ch.Int.*, vol. 50, no. 46, pp. 10 839–10 842, 2011.

[58] G. S. Bang, K. W. Nam, J. Y. Kim, J. Shin, J. W. Choi, and S.-Y. Choi, "Effective liquid-phase exfoliation and sodium ion battery application of MoS_2 nanosheets," *ACS Appl. Mater. Interfaces*, vol. 6, no. 10, pp. 7084–7089, 2014.

[59] M. M. Bernal, L. Alvarez, E. Giovanelli, A. Arnaiz, L. Ruiz-Gonzalez, S. Casado, D. Granados, A. M. Pizarro, A. Castellanos-Gomez, and E. M. Perez, "Luminescent transition metal dichalcogenide nanosheets through one-step liquid phase exfoliation," *2D Mater.*, vol. 3, no. 3, p. 035 014, 2016.

[60] C. Y. Zhi, Y. Bando, C. C. Tang, H. Kuwahara, and D. Golberg, "Large-scale fabrication of boron nitride nanosheets and their utilization in polymeric composites with improved thermal and mechanical properties," *Adv. Mater.*, vol. 21, no. 28, pp. 2889–2893, 2009.

[61] D. Hanlon, C. Backes, E. Doherty, C. S. Cucinotta, N. C. Berner, C. Boland, K. Lee, P. Lynch, Z. Gholamvand, A. Harvey, S. Zhang, K. Wang, G. Moynihan, A. Pokle, Q. M. Ramasse, N. McEvoy, W. J. Blau, J. Wang, G. Abellan, F. Hauke, A. Hirsch, S. Sanvito, D. D. O'Regan, G. S. Duesberg, V. Nicolosi, and J. N. Coleman, "Liquid exfoliation of solvent-stabilized few-layer black phosphorus for applications beyond electronics," *Nat. Commun.*, vol. 6, p. 8563, 2015.

[62] G. E. Moore, "Cramming more components onto integrated circuits," *Electronics*, vol. 38, no. 8, pp. 114–117, 1965.

[63] ——, "Progress in digital integrated electronics," *Proceedings of the international electron devices meeting*, vol. 21, pp. 11–13, 1975.

[64] D. Lembke, S. Bertolazzi, and A. Kis, "Single-layer MoS_2 electronics," *Acc. Chem. Res.*, vol. 48, no. 1, pp. 100–110, 2015.

[65] A. K. Geim and K. S. Novoselov, "The rise of graphene," *Nature Mater.*, vol. 6, no. 3, pp. 183–191, 2007.

[66] A. K. Geim, "Graphene: Status and prospects," *Science*, vol. 324, no. 5934, pp. 1530–1534, 2009.

[67] L. Banszerus, M. Schmitz, S. Engels, J. Dauber, M. Oellers, F. Haupt, K. Watanabe, T. Taniguchi, B. Beschoten, and C. Stampfer, "Ultrahigh-mobility graphene devices from chemical vapor deposition on reusable copper," *Sci. adv.*, vol. 1, no. 6, e1500222, 2015.

[68] F. Schwierz, "Graphene transistors," *Nature Nanotechnol.*, vol. 5, no. 7, pp. 487–496, 2010.

[69] V. Podzorov, M. E. Gershenson, C. Kloc, R. Zeis, and E. Bucher, "High-mobility field-effect transistor based on transition metal dichalcogenides," *Appl. Phys. lett.*, vol. 84, no. 17, pp. 3301–3303, 2004.

[70] S. Bertolazzi, D. Krasnozhon, and A. Kis, "Non volatie memoriy cells based on MoS_2/graphene heterostructures.," *ACS Nano*, vol. 7, pp. 3246–3252, 2013.

[71] B. Radisavljeevic, M. B. Whitwick, and A. Kis, "Small-signal amplifier based on single-layer MoS_2," *Appl. Phys. Lett.*, vol. 101, no. 4, p. 043 103, 2012.

[72] O. Lopez-Sanchez, D. Lembke, M. Kayci, A. Radenovic, and A. Kis, "Ultrasensitive photodetectors based on monolayer MoS_2," *Nat. Nanotechnol.*, vol. 8, no. 7, pp. 497–501, 2013.

[73] K. F. Mak, K. He, J. Shan, and T. F. Heinz, "Control of valley polarization in monolayer MoS_2 by optical helicity," *Nat. Nanotechnol.*, vol. 7, no. 8, pp. 494–498, 2012.

[74] M. S. Nevius, M. Conrad, F. Wang, A. Celis, M. N. Nair, A. Taleb-Ibrahimi, A. Tejeda, and E. H. Conrad, "Perspectives for spintronics in 2d materials," *Apl. Mater.*, vol. 4, no. 3, p. 032 401, 2016.

[75] N. Tombros, C. Jozsa, M. Popinciuc, H. T. Jonkman, and B. J. van Wees, "Electronic spin transport and spin precession in single graphene layers at room temperature," *Nature*, vol. 448, no. 7153, pp. 571–574, 2007.

[76] B. Dlubak, M.-B. Martin, C. Deranlot, B. Servet, S. Xavier, R. Mattana, M. Sprinkle, C. Berger, W. A. D. Heer, F. Petroff, A. Anane, P. Seneor, and A. Fert, "Highly efficient spin transport in epitaxial graphene on SiC," *Nature Phys.*, vol. 8, no. 7, pp. 557–561, 2012.

[77] Z. Y. Zhu, Y. C. Cheng, and U. Schwingenschlögl, "Giant spin-orbit-induced spin splitting in two-dimensional transition-metal dichalcogenide semiconductors," *Phys. Rev. B*, vol. 84, no. 15, p. 153 402, 2011.

[78] H. Zeng, J. Dai, W. Yao, and D. X. and Xiaodong Cui, "Valley polarization in MoS_2 monolayers by optical pumping," *Nature Nanotech.*, vol. 7, no. 8, pp. 490–493, 2012.

[79] D. Xiao, G.-B. Liu, W. Feng, X. Xu, and W. Yao, "Coupled spin and valley physics in monolayers of MoS_2 and other group-VI dichalcogenides," *Phys. Rev. Lett.*, vol. 108, no. 19, p. 196 802, 2012.

[80] D. Kozawa, R. Kumar, A. Carvalho, K. K. Amara, W. Zhao, S. Wang, M. Toh, R. M. Ribeiro, A. C. Neto, K. Matsuda, and G. Eda, "Photocarrier relaxation pathway in two-dimensional semiconducting transition metal dichalcogenides," *Nature Commun.*, vol. 5, p. 4543, 2014.

[81] M. Amani, D.-H. Lien, D. Kiriya, J. Xiao, A. Azcat, J. Noh, S. R. Madhvapathy, R. Addou, S. KC, M. Dubey, K. Cho, R. M. Wallace, S.-C. Lee, J.-H. He, J. W. A. III, X. Zhang, E. Yablonovitch, and A. Javey, "Near-unity photoluminescence quantum yield in MoS_2," *Science*, vol. 350, no. 6264, pp. 1065–1068, 2015.

[82] P. Tonndorf, R. Schmidt, R. Schneider, J. Kern, M. Buscema, G. A. Steele, A. Castellanos-Gomez, H. S. J. V. der Zant, S. M. de Vasconcellos, and R. Bratschitsch, "Single-photon emission from localized excitons in an atomically thin semiconductor," *Optica*, vol. 2, no. 4, pp. 347–352, 2015.

[83] L. Klopotowski, C. Backes, A. Mitioglu, V. Vega-Mayoral, D. Hanlon, J. Coleman, V. Ivanov, D. Maude, and P. Plochocka, "Revealing the nature of excitons in liquid exfoliated monolayer tungsten disulphide," *Nanotechnology*, vol. 27, no. 42, p. 425 701, 2016.

[84] A. Chernikov, A. M. van der Zande, H. M. Hill, A. F. Rigosi, A. Velauthapillai, J. Hone, and T. F. Heinz, "Electrical tuning of exciton binding energies in monolayer WS_2," *Phys. Rev. Lett.*, vol. 115, no. 12, p. 126 802, 2015.

[85] X.-X. Zhang, Y. You, S. Y. F. Zhao, and T. F. Heinz, "Experimental evidence for dark excitons in monolayer WSe_2," *Phys. Rev. Lett.*, vol. 115, no. 25, p. 257 403, 2015.

[86] K. F. Mak, K. He, C. Lee, G. H. Lee, J. Hone, T. F. Heinz, and J. Shan, "Tightly bound trions in monolayer MoS_2," *Nature Materials*, vol. 12, no. 3, pp. 207–211, 2013.

[87] A. M. Jones, H. Yu, N. J. Ghimire, S. Wu, G. Aivazian, J. S. Ross, B. Zhao, J. Yan, D. G. Mandrus, D. Xiao, W. Yao, and X. Xu, "Optical generation of excitonic valley coherence in monolayer WSe_2," *Nature Nanotech.*, vol. 8, no. 9, pp. 634–638, 2013.

[88] X. Zheng, Y. Zhang, R. Chen, X. Cheng, Z. Xu, and T. Jiang, "Z-scan measurement of the nonlinear refractive index of monolayer WS_2," *Opt. Express*, vol. 23, no. 12, pp. 15 616–15 623, 2015.

[89] H. Ahmad, M. A. Ismail, M. Suthaskumar, Z. C. Tiu, S. W. Harun, M. Z. Zulkifli, S. Samikannu, and S. Sivaraj, "S-band Q-switched fiber laser using molybdenum disulfide (MoS_2) saturable absorber," *Laser Phys. Lett.*, vol. 13, no. 3, p. 035 103, 2016.

[90] J. Du, Q. Wang, G. Jiang, C. Xu, C. Zhao, Y. Xiang, Y. Chen, S. Wen, and H. Zhang, "Ytterbium-doped fiber laser passively mode locked by few-layer molybdenum disulfide (MoS_2) saturable absorber functioned with evanescent field interaction," *Sci. Rep.*, vol. 4, p. 6346, 2014.

[91] K. Wang, J. Wang, J. Fan, M. Lotya, A. O'Neill, D. Fox, Y. Feng, X. Zhang, B. Jiang, Q. Zhao, H. Zhang, J. N. Coleman, L. Zhang, and W. J. Blau, "Ultrafast saturable absorption of two-dimensional MoS_2 nanosheets," *ACS Nano.*, vol. 7, no. 10, pp. 9260–9267, 2013.

[92] K.-G. Zhou, M. Zhao, M.-J. Chang, Q. Wang, X.-Z. Wu, Y. Song, and H.-L. Zhang, "Attosecond molecular dynamics: Fact or fiction?" *Small*, vol. 11, no. 6, p. 634, 2014.

[93] C. Janisch, N. Mehta, D. Ma, A. L. Elías, N. Perea-López, M. Terrones, and Z. Liu, "Ultrashort optical pulse characterization using WS_2 monolayers," *Opt. Lett.*, vol. 39, no. 2, pp. 383–385, 2014.

[94] H. Shi, R. Yan, S. Bertolazzi, J. Brivio, B. Gao, A. Kis, D. Jena, H. G. Xing, and L. Huang, "Exciton dynamics in suspended monolayer and few-layer MoS_2 2d crystals," *ACS Nano*, vol. 7, no. 2, pp. 1072–1080, 2013.

[95] Z. Nie, R. Long, L. Sun, C.-C. Huang, J. Zhang, Q. Xiong, D. W. Hewak, Z. Shen, O. V. Prezhdo, and Z.-H. Loh, "Ultrafast carrier thermalization and cooling dynamics in few-layer MoS_2," *ACS Nano*, vol. 8, no. 10, pp. 10 931–10 940, 2014.

[96] A. Steinhoff, M. Florian, M. Rosner, M. Lorke, T. O. Wehling, C. Gies, and F. Jahnke, "Nonequilibrium carrier dynamics in transition metal dichalcogenide semiconductors," *2D Mater.*, vol. 3, no. 3, p. 031 006, 2016.

[97] N. Kumar, J. He, D. He, Y. Wang, and H. Zhao, "Charge carrier dynamics in bulk MoS_2 crystal studied by transient absorption microscopy," *J. Appl. Phys.*, vol. 113, no. 13, p. 133 702, 2013.

[98] H. Wang, C. Zhang, and F. Rana, "Ultrafas dynamics of defect assisted electron-hole recombination in monolayer MoS_2," *Nano Lett.*, vol. 15, no. 1, pp. 339–345, 2015.

[99] ——, "Surface recombination limited lifetimes of photoexcited carriers in few-layer transition metal dichalcogenide MoS_2," *Nano Lett.*, vol. 15, no. 12, pp. 8204–8201, 2015.

[100] S. Sim, J. Park, J.-G. Song, C. In, Y.-S. Lee, H. Kim, and H. Choi, "Exciton dynamics in atomically thin MoS_2: Interexcitonic interaction and broadening kinetics," *Phys. Rev. B*, vol. 88, no. 7, p. 075 434, 2013.

[101] P. D. Cunningham, K. M. McCreary, A. T. Hanbicki, M. Currie, B. T. Jonker, and L. M. Hayden, "Charge trapping and exciton dynamics in large -area cvd grown MoS_2," *J. Phy. Chem. C*, vol. 120, no. 10, pp. 5819–5826, 2016.

[102] T. Borzda, C. Gadermaier, N. Vujicic, P. Topolovsek, M. Borovsak, T. Mertelj, D. Viola, C. Manzoni, E. A. A. Pogna, D. Brida, M. R. Antognazza, F. Scotognella, G. Lanzani, G. Cerullo, and D. Mihailovic, "Charge photogeneration in few-layer MoS_2," *Adv. Mater.*, vol. 25, no. 22, pp. 3351–3358, 2015.

[103] R. Wang, B. A. Ruzicka, N. Kumar, M. Z. Bellus, H.-Y. Chiu, and H. Zhao, "Ultrafast and spatially resolved studies of charge carriers in atomically thin molybdenum disulfide," *Phys. Rev. B*, vol. 86, no. 4, p. 045 406, 2012.

[104] Q. Cui, F. Ceballos, N. Kumar, and H. Zhao, "Transient absorption microscopy of monolayer and bulk WSe_2," *ACS Nano*, vol. 8, no. 3, pp. 2970–2976, 2014.

[105] A. Chernikov, C. Ruppert, H. M. Hill, A. F. Rigosi, and T. F. Heinz, "Population inversion and giant bandgap renormalization in atomically thin WS_2 layers," *Nature Photon.*, vol. 9, no. 7, pp. 466–470, 2015.

[106] N. Kumar, Q. Cui, F. Ceballos, D. He, Y. Wang, and H. Zhao, "Exciton-exciton annihilation in $MoSe_2$ monolayers," *Phys. Rev. B*, vol. 89, no. 12, p. 125 427, 2014.

[107] D. Sun, Y. Rao, G. A. Reider, G. Chen, Y. You, L. Breezin, A. R. Harutyunyan, and T. F. Heinz, "Observation of rapid exciton-exciton annihilation in monolayer molybdenum disulfide," *Nano Lett.*, vol. 14, no. 10, pp. 5625–5629, 2014.

[108] S. Mouri, Y. Miyauchi, M. Toh, W. Zhao, G. Eda, and K. Matsuda, "Nonlinear photoluminescence in atomically thin layered WSe_2 arising from diffusion-assisted exciton-exciton annihilation," *Phys. Rev. B*, vol. 90, no. 15, p. 155 449, 2014.

[109] L. Yuan and L. Huang, "Exciton dynamics and annihilation in WS_2 2d semiconductors," *Nanoscale*, vol. 7, no. 16, pp. 7402–7408, 2015.

[110] A. Steinhoff, M. Rossner, F. Jahnke, T.O.Wehling, and C. Gies, "Influence of excited carriers on the optical and electronic properties of MoS_2," *Nano Lett.*, vol. 14, no. 7, pp. 3743–3748, 2014.

[111] E. A. A. Pogna, M. Marsili, D. de Fazio, S. D. Conte, C. Manzoni, D. Sangalli, D. Yoon, A. Lombardo, A. C. Ferrari, A. Marini, G. Cerullo, and D. Prezzi, "Photo-induced bandgap renormalization governs the ultrafast response of single-layer MoS_2," *ACS Nano*, vol. 10, no. 1, pp. 1182–1188, 2016.

[112] G. R. Kirchhoff and R. W. Bunsen, "Chemische Analyse durch Spektralbeobachtung, I," *Ann. Physik*, vol. 110, no. 6, pp. 161–189, 1860.

[113] ——, "Chemische Analyse durch Spektralbeobachtung, II," *Ann. Physik.*, vol. 113, pp. 338–381, 1861.

[114] P. Bouguer, *Essai d'optique sur la gradation de la lumière*. Paris, France: Approved by the king, 1729.

[115] J. H. Lambert, *Photometria sive de mensura et gradibus luminis, colorum et umbrae*. Augsburg, Germany: Augusta Vindelicorum, 1760.

[116] A. Beer, "Bestimmung der Absorption des rothen Lichts in farbigen Flüssigkeiten," *Annalen der Physik und Chemie*, vol. 86, no. 5, pp. 78–88, 1852.

[117] C. Backes, R. J. Smith, N. McEvoy, N. C. Berner, D. McCloskey, H. C. Nerl, A. O'Neill, P. J. King, T. Higgins, D. Hanlon, N. Scheuschner, J. Maultzsch, L. Houben, G. S. Duesberg, J. F. Donegan, V. Nicolosi, and J. N. Coleman, "Edge and confinement effects allow in situ measurement of size and thickness of liquid-exfoliated nanosheets," *Nat. Commun.*, vol. 5, p. 4576, 2014.

[118] C. Backes, B. M. Szydlowska, A. Harvey, S. Yuan, V. Vega-Mayoral, B. R. Davies, P.-l. Zhao, D. Hanlon, E. J. G. Santos, M. I. Katsnelson, W. J. Blau, C. Gadermaier, and J. N. Coleman, "Production of highly monolayer enriched dispersions of liquid-exfoliated nanosheets by liquid cascade centrifugation," *ACS Nano*, vol. 10, no. 1, pp. 1589–1601, 2016.

[119] N. Monardes, *Historia medicinal de las cosas que se traen de nuestras indias orientales*. –: –, 1565.

[120] M. N. Berderan-Santos, *Fluorescence of supermolecules, polymers, and nanosystems*. Springer Berlin Heidelberg New York: Springer, 2008.

[121] R. Eisberg and R. Resnick, *Quantum physics of atoms, molecules, solids, nuclei, and particles*. New York: John Wiley & sons, 1985.

[122] C. V. Raman, "A new radiation," *Indian J. Phys.*, vol. 2, pp. 387–398, 1928.

[123] A. C. Ferrari, J. C. Meyer, V. Scardadi, C. Casiraghi, M. Lazzeri, F. Mauri, S. Piscanec, D. Jiang, K. S. Novoselov, S. Roth, and A. K. Geim, "Raman spectrum of graphene and graphene layers," *Phys. Rev. Lett.*, vol. 97, no. 18, p. 187 401, 2006.

[124] F. Lepine, M. Y. Ivanov, and M. J. J. Vrakking, "Size-dependent nonlinear optical properties of atomically thin transition metal dichalcogenide nanosheets," *Nature Photon*, vol. 8, no. 3, pp. 195–204, 2014.

[125] Y.-H. Liau, A. N. Unterreiner, D. C. Arnett, and N. F. Scherer, "Femtosecond-pulse cavity-dumped solid-state oscillator design and application to ultrafast microscopy," *Appl. Opt.*, vol. 38, no. 36, pp. 7386–7392, 1999.

[126] F. J. McClung and R. W. Hellwarth, "Giant optical pulsations from ruby," *Journal of Applied Physics*, vol. 1, no. S1, pp. 103–105, 1962.

[127] D. Strickland and G. Mourou, "Compression of amplified chirped optical pulses," *Opt. Commun.*, vol. 56, no. 3, pp. 219–221, 1985.

[128] R. W. Boyd, *Nonlinear optics*. New York: Elsevier, 2008.

[129] R. Trebino, "Nonlinear optics course," Master's thesis, Georgia Institute of Technology, Georgia, USA.

[130] R. R. Alfano and S. L. Shapiro, "Emission in the region 4000 to 7000 A via four-photon coupling in glass," *Phys. Rev. Let.*, vol. 24, no. 11, pp. 584–587, 1970.

[131] N. Dong, Y. Li, S. Zhang, N. McEvoy, X. Zhang, Y. Cui, L. Zhang, G. S. Duesberg, and J. Wang, "Dispersion of nonlinear refractive index in layered WS_2 and WSe_2 semiconductor films induced by two-photon absorption," *Opt. Lett.*, vol. 41, no. 17, pp. 3936–3939, 2016.

[132] Q. C. Sun, L. Yadgarov, R. Rosentsveig, S. G, R. Tenne, and J. L. Musfeldt, "Observation of a burstein-moss shift in rhenium-doped MoS_2 nanoparticles.," *ACS Nano*, vol. 7, no. 4, pp. 3506–3511, 2013.

[133] V. I. Klimov, S. A. Ivanov, J. Nanda, M. Achermann, I. Bezel, J. A. McGuire, and A. Piryatinski, "Single-exciton optical gain in semiconductor nanocrystals," *Nature*, vol. 447, no. 7143, pp. 441–446, 2007.

[134] C. M. Hansen, *Hansen solubility parameters: A user's handbook, second edition*. New York: CRC press, 2007.

[135] J. N. Coleman, "Liquid-phase exfoliation of nanotubes and graphene," *Adv. Funct. Mater.*, vol. 19, no. 23, pp. 3680–3695, 2009.

[136] S. D. Bergin, Z. Sun, D. Rickards, P. V. Streich, J. P. Hamilton, and J. N. Coleman, "Multicomponent solubility parameters for single walled carbon nanotube-solvent mixtures," *ACS Nano*, vol. 3, no. 8, pp. 2340–2350, 2009.

[137] G. Cunningham, M. Lotya, C. S. Cucinotta, S. Sanvito, S. D. Bergin, R. Menzel, M. S. P. Shaffer, and J. N. Coleman, "Solvent exfoliation of transition metal dichalcogenides: Dispersibility of exfoliated nanosheets varies only weakly between compounds," *ACS Nano*, vol. 6, no. 4, pp. 3468–3480, 2012.

[138] J. M. Hughes, D. Aherne, and J. N. Coleman, "Generalizing solubility parameter theory to apply to one- and two-dimensional solutes and to incorporate dipolar interactions," *Adv. Funct. Mater.*, vol. 127, no. 6, pp. 4483–4491, 2013.

[139] J. D. Fuhr and J. O. Sofo, "Adsorption of Pd on MoS_2 (1000): Ab initio electronic-structure calculations," *Phys. Rev. B*, vol. 60, no. 11, pp. 8343–8347, 1999.

[140] P. Joensen, R. Frindt, and S. R. Morrison, "Single-layer MoS_2," *Mat. Res. Bull.*, vol. 21, no. 4, pp. 457–461, 1986.

[141] R. J. Hunter, *Foundations of colloid science*. Oxford, United Kingdom: Oxford university press, 2001.

[142] M. J. Rosen, *Surfactants and interfacial phenomena*. Springer Berlin Heidelberg New York: Wiley-Interscience, 2004.

[143] V. Nicolosi, D. Vrbanic, A. Mrzel, J. McCauley, S. O'Flaherty, C. McGuinness, G. Compagnini, D. Mihailovic, W. J. Blau, and J. N. Coleman, "Solubility of $Mo_6S_{4.5}I_{4.5}$ nanowires in common solvents: A sedimentation study," *J. Phys. Chem. B*, vol. 109, no. 15, pp. 7124–7133, 2005.

[144] P. Atkins and J. de Paula, *Physical chemistry*. New York: W H Freeman & Co, 2009.

[145] V. Vega-Mayoral, C. Backes, D. Hanlon, U. Khan, Z. Gholamvand, M. O'Brien, G. S. Duesberg, C. Gadermaier, and J. N. Coleman, "Photoluminescence from liquid-exfoliated WS_2 monomers in poly(vinyl alcohol) polymer composites," *Adv. Funct. Mater.*, vol. 26, no. 7, pp. 1028–1039, 2016.

[146] M. Chhowalla, H. S. Shin, G. Eda, L.-J. Li, K. P. Loh, and H. Zhang, "The chemistry of two-dimensional layered transition metal dichalcogenide nanosheets," *Nat Chem.*, vol. 5, no. 4, pp. 263–285, 2013.

[147] A. K. Geim and I. V. Grigorieva, "Van der waals heterostructures," *Nature*, vol. 499, no. 7459, pp. 419–425, 2013.

[148] K. S. Novoselov, V. I. Fal'ko, L. Colombo, P. R. Gellert, M. G. Schwab, and K. Kim, "A roadmap for graphene,"

[149] Y. Kojima, A. Usuki, M. Kawasumi, A. Okada, Y. Fukushima, T. Kurauchi, and O. Kamigaito, "Synthesis of nylon 6-clay hybrid," *J. Mater. Res.*, vol. 8, no. 5, p. 1185, 1993.

[150] X. Huang, X. Qi, F. Boey, and H. Zhang, "Graphene-based composites," *Chem. Soc. Rev.*, vol. 41, no. 2, pp. 666–686, 2012.

[151] H. Kim, A. A. Abdala, and C. W. Macosko, "Graphene/polymer nanocomposites," *Macromolecules*, vol. 43, no. 16, pp. 6515–6530, 2010.

[152] R. J. Young, I. A. Kinloch, L. Gong, and K. S. Novoselov, "The mechanics of graphene nanocomposites: A review," *Comp. Sci. Techn.*, vol. 72, no. 12, pp. 1459–1476, 2012.

[153] T. Hasan, Z. Sun, F. Wang, F. Bonaccorso, P. H. Tan, A. G. Rozhin, and A. C. Ferrari, "Nanotube–polymer composites for ultrafast photonics," *Adv. Mater.*, vol. 21, no. 38–39, pp. 3874–3899, 2009.

[154] Z. Sun, F. T. T. Hasan, D. Popa, G. Privitera, F. Wang, F. Bonaccorso, D. M. Basko, and A. C. Ferrari, "Graphene mode-locked ultrafast laser," *ACS Nano*, vol. 4, no. 2, pp. 803–810, 2010.

[155] M. Zhang, E. J. R. Kelleher, F. Torrisi, Z. Sun, T. Hasan, D. Popa, F. Wang, A. C. Ferrari, S. V. Popov, and J. R. Taylor, "Tm-doped fiber laser mode-locked by graphene-polymer composite," *Opt. Express*, vol. 20, no. 22, pp. 25 077–25 084, 2012.

[156] O. Eksik, J. Gao, S. A. Shojaee, A. Thomas, P. Chow, S. F. Bartolucci, D. A. Lucca, and N. Koratkar, "Epoxy nanocomposites with two-dimensional transition metal dichalcogenide additives," *ACS Nano.*, vol. 8, no. 5, pp. 5282–5289, 2014.

[157] A. Sorrentino, C. Altavilla, M. Merola, A. Senatore, P. Ciambelli, and S. Iannace, "Nanosheets of MoS_2-oleylamine as hybrid filler for self-lubricating polymer composites: Thermal, tribological, and mechanical properties," *Pol. Comp.*, vol. 36, no. 6, pp. 1124–1134, 2015.

[158] K. Zhou, S. Jiang, C. Bao, L. Song, B. Wang, G. Tang, Y. Hu, and Z. Gui, "Preparation of poly(vinyl alcohol) nanocomposites with molybdenum disulfide (MoS_2): Structural characteristics and markedly enhanced properties," *RSC Adv.*, vol. 2, no. 31, pp. 11 695–11 703, 2012.

[159] F. Xiaoming, K. Farhad, R. Vahid, S. Mariyappan, L. Masoud, J. Jacek, W. C. Robert, T. Eugene, and P. Balaji, "MoS_2 actuators: Reversible mechanical responses of MoS_2-polymer nanocomposites to photons," *Nanotechnology*, vol. 26, no. 26, p. 261 001, 2015.

[160] Y. Huang, Z. Luo, Y. Li, M. Zhong, B. Xu, K. Che, H. Xu, Z. Cai, J. Peng, and J. Weng, "Widely-tunable, passively Q-switched erbium-doped fiber laser with few-layer MoS_2 saturable absorber," *Opt. Express*, vol. 22, no. 21, pp. 25 258–25 266, 2014.

[161] Z. Luo, Y. Huang, M. Zhong, Y. Li, J. Wu, B. Xu, H. Xu, Z. Cai, J. Peng, and J. Weng, "1-, 1.5-, and 2- micrometer fiber lasers Q-switched by a broadband few-layer MoS_2 saturable absorver," *J. lightwave Technol.*, vol. 32, no. 24, pp. 4077–4084, 2014.

[162] R. I. Woodward, E. J. R. Kelleher, R. C. T. Howe, G. Hu, F. Torrisi, T. Hasan, S. V. Popov, and J. R. Taylor, "Tunable Q-switched fiber laser based on saturable edge-state absorption in few-layer molybdenum disulfide (MoS_2)," *Opt. Express*, vol. 22, no. 25, pp. 31 113–31 122, 2014.

[163] M. Zhang, R. T. Howe, R. Woodward, E. R. Kelleher, F. Torrisi, G. Hu, S. Popov, J. R. Taylor, and T. Hasan, "Solution processed MoS_2-PVA composite for sub-bandgap mode-locking of a wideband tunable ultrafast er:fiber laser," *Nano Res.*, vol. 8, no. 5, pp. 1522–1534, 2015.

[164] Z. Q. Luo, Y. Y. Li, M. Zhong, Y. Z. Huang, X. J. Wan, J. Peng, and J. Weng, "Nonlinear optical absorption of few-layer molybdenum diselenide ($MoSe_2$) for passively mode-locked soliton fiber laser," *Photonics Res.*, vol. 3, no. 3, A79–A86, 2015.

[165] K. R. Paton, E. Varrla, C. Backes, R. J. Smith, U. Khan, A. O'Neill, C. Boland, M. Lotya, O. M. Istrate, P. King, T. Higgins, S. Barwich, P. May, P. Puczkarski, I. Ahmed, M. Moebius, H. Pettersson, E. Long, J. Coelho, S. E. O'Brien, E. K. McGuire, B. M. Sanchez, G. S. Duesberg, N. McEvoy, T. J. Pennycook, C. Downing, A. Crossley, V. Nicolosi, and J. N. Coleman, "Scalable production of large quantities of defect-free few-layer graphene by shear exfoliation in liquids," *Nat. Mater.*, vol. 13, no. 6, pp. 624–630, 2014.

[166] T. J. Nacken, C. Damm, J. Walter, A. Ruger, and W. Peukert, "Delamination of graphite in a high pressure homogenizer," *RSC Adv.*, vol. 5, no. 71, pp. 57 328–57 338, 2015.

[167] M. Lotya, Y. Hernandez, P. J. King, R. J. Smith, V. Nicolosi, L. S. Karlsson, F. M. Blighe, S. De, Z. Wang, I. T. McGovern, G. S. Duesberg, and J. N. Coleman, "Liquid phase production of graphene by exfoliation of graphite in surfactant/water solutions," *J. Am. Chem. Soc.*, vol. 131, no. 10, p. 3611, 2009.

[168] Y. T. Liang and M. C. Hersam, "Highly concentrated graphene solutions via polymer enhanced solvent exfoliation and iterative solvent exchange," *J. Am. Chem. Soc*, vol. 132, no. 50, pp. 17 661–17 663, 2010.

[169] A. B. Bourlinos, V. Georgakilas, R. Zboril, T. A. Steriotis, A. K. Stubos, and C. Trapalis, "Aqueous-phase exfoliation of graphite in the presence of polyvinylpyrrolidone for the production of water-soluble graphenes," *Solid State Commun.*, vol. 149, no. 47–48, p. 2172, 2009.

[170] P. Yasaei, B. Kumar, T. Foroozan, C. Wang, M. Asadi, D. Tuschel, J. E. Indacochea, R. F. Klie, and A. Salehi-Khojin, "High-quality black phosphorus atomic layers by liquid-phase exfoliation," *Adv. Mater.*, vol. 27, no. 11, pp. 1887–1892, 2015.

[171] V. Sresht, A. A. H. Padua, and D. Blankschtein, "Liquid-phase exfoliation of phosphorene: Design rules from molecular dynamics simulations," *ACS Nano*, vol. 9, no. 8, pp. 8255–8268, 2015.

[172] J. Kang, J. D. Wood, S. A. Wells, J.-H. Lee, X. Liu, K.-S. Chen, and M. C. Hersam, "Solvent exfoliation of electronic-grade, two-dimensional black phosphorus," *ACS Nano*, vol. 9, no. 4, pp. 3596–3604, 2015.

[173] J. R. Brent, N. Savjani, E. A. Lewis, S. J. Haigh, D. J. Lewis, and P. O'Brien, "Production of few-layer phosphorene by liquid exfoliation of black phosphorus," *Chem. Commun.*, vol. 50, no. 87, pp. 13 338–13 341, 2014.

[174] M. Naguib, O. Mashtalir, J. Carle, V. Presser, J. Lu, L. Hultman, Y. Gogotsi, and M. W. Barsou, "Two-dimensional transition metal carbides," *ACS Nano*, vol. 6, no. 2, pp. 1322–1331, 2012.

[175] A. Harvey, C. Backes, Z. Gholamvand, D. Hanlon, D. McAteer, H. C. Nerl, E. McGuire, A. Seral-Ascaso, Q. M. Ramasse, N. McEvoy, S. Winters, N. C. Berner, D. McCloskey, J. Donegan, G. Duesberg, V. Nicolosi, and J. N. Coleman, "Preparation of gallium sulfide nanosheets by liquid exfoliation and their application as hydrogen evolution catalysts," *Chem. Mater.*, vol. 27, no. 9, pp. 3483–3493, 2015.

[176] T. M. Higgins, D. McAteer, J. C. M. Coelho, B. M. Sanchez, Z. Gholamvand, G. Moriarty, N. McEvoy, N. C. Berner, G. S. Duesberg, V. Nicolosi, and J. N. Coleman, "Effect of percolation on the capacitance of supercapacitor electrodes prepared from composites of manganese dioxide nanoplatelets and carbon nanotubes," *ACS Nano*, vol. 8, no. 9, pp. 9567–9579, 2014.

[177] U. Khan, P. May, A. O'Neill, A. P. Bell, E. Boussac, A. Martin, J. Semple, and J. N. Coleman, "Polymer reinforcement using liquid-exfoliated boron nitride nanosheets," *Nanoscale*, vol. 5, no. 2, pp. 581–587, 2013.

[178] P. May, U. Khan, A. O'Neill, and J. N. Coleman, "Approaching the theoretical limit for reinforcing polymers with graphene," *J. Mater. Chem*, vol. 22, no. 4, pp. 1278–1282, 2012.

[179] P. May, U. Khan, J. M. Hughes, and J. N. Coleman, "Role of solubility parameters in understanding the steric stabilization of exfoliated two-dimensional nanosheets by adsorbed polymers," *J. Phys. Chem. C*, vol. 116, no. 20, pp. 11 393–11 400, 2012.

[180] J. N. Israelachvili, *Intermolecular and surface forces*. San Diego, CA, USA: Academic Press, 1991.

[181] S. Xie, O. M. Istrate, P. May, S. Barwich, A. P. Bell, U. Khan, and J. N. Coleman, "Boron nitride nanosheets as barrier enhancing fillers in melt processed composites," *Nanoscale*, vol. 7, no. 10, pp. 4443–4450, 2015.

[182] O. M. Istrate, K. R. Paton, U. Khan, A. O'Neill, A. P. Bell, and J. N. Coleman, "Reinforcement in melt-processed polymer-graphene composites at extremely low graphene loading level," *Carbon*, vol. 78, pp. 243–249, 2014.

[183] U. Khan, A. O'Neill, H. Porwal, P. May, K. Nawaz, and J. N. Coleman, "Size selection of dispersed, exfoliated graphene flakes by controlled centrifugation," *Carbon*, vol. 50, no. 2, pp. 470–475, 2012.

[184] H. Terrones, E. D. Corro, S. Feng, J. M. Poumirol, D. Rhodes, D. Smirnov, N. R. Pradhan, Z. Lin, M. A. T. Nguyen, A. L. Elias, T. E. Mallouk, L. Balicas, M. A. Pimenta, and M. Terrones, "New first order Raman-active modes in few layered transition metal dichalcogenides," *Sci. Rep.*, vol. 4, p. 4215, 2014.

[185] H. R. Gutiérrez, N. Perea-López, A. L. Elías, A. Berkdemir, B. Wang, R. Lv, F. López-Urías, V. H. Crespi, H. Terrones, and M. Terrones, "Extraordinary room-temperature photoluminescence in triangular WS_2 monolayers," *Nano Lett.*, vol. 13, no. 8, pp. 3447–3454, 2013.

[186] M. Buzaglo, M. Shtein, S. Kober, R. Lovrincic, A. Vilan, and O. Regev, "Critical parameters in exfoliating graphite into graphene," *Phys. Chem. Chem. Phys.*, vol. 15, no. 12, pp. 4428–4435, 2013.

[187] X. L. Y. Lin, S. H. L. Yu, A. L. Hsu, Y.-H. Lee, J. Kong, M. S. Dresselhaus, and T. Palacios, "Dielectric screening of excitons and trions in single-layer MoS_2," *Nano Lett.*, vol. 14, no. 10, pp. 5569–5576, 2014.

[188] K. F. Mak, C. Lee, J. Hone, J. Shan, and T. F. Heinz, "Atomically thin MoS_2: A new direct-gap semiconductor," *Phys. Rev. Lett.*, vol. 105, no. 13, p. 136 805, 2010.

[189] J. S. Ross, S. Wu, H. Yu, N. J. Ghimire, A. M. Jones, G. Aivazian, J. Yan, D. G. Mandrus, D. Xiao, W. Yao, and X. Xu, "Electrical control of neutral and charged excitons in a monolayer semiconductor," *Nat. Commun.*, vol. 4, no. 2498, p. 1474, 2013.

[190] S. Mouri, Y. Miyauchi, and K. Matsuda, "Tunable photoluminescence of monolayer MoS_2 via chemical doping," *Nano Lett.*, vol. 13, no. 12, pp. 5944–5948, 2013.

[191] M. Rubinstein and R. H. Colby, *Polymer physics*. Oxford: Oxford University Press, 2003.

[192] N. Peimyoo, W. Yang, J. Shang, X. Shen, Y. Wang, and T. Yu, "Chemically driven tunable light emission of charged and neutral excitons in monolayer WS_2," *ACS Nano*, vol. 8, no. 11, pp. 11 320–11 329, 2014.

[193] H. Qiu, T. Xu, Z. Wang, W. Ren, H. Nan, Z. Ni, Q. Chen, S. Yuan, F. Miao, F. Song, G. Long, Y. Shi, L. Sun, J. Wang, and X. Wang, "Hopping transport through defect-induced localized states in molybdenum disulphide," *Nat. Commun.*, vol. 4, no. 3642, p. 2642, 2013.

[194] Z. Xiaomin, Z. Li, H. Xueying, and W. Juntao, "Fabrication and application of new polymer-based materials by freeze-drying," *Prog. Chem*, vol. 26, no. 11, pp. 1832–1839, 2014.

[195] C. Teng, Y. Gao, X. Wang, W. Jiang, C. Zhang, R. Wang, D. Zhou, and G. Xue, "Reentanglement kinetics of freeze-dried polymers above the glass transition temperature," *Macromolecules*, vol. 45, no. 16, pp. 6648–6651, 2012.

[196] V. Vega-Mayoral, D. Vella, T. Borzda, M. Prijatelj, Z. G. Tempra, E. A. A. Pogna, S. D. Conte, P. Topolovsek, N. Vujicic, G. Cerullo, D. Mihailovic, and C. Gadermaier, "Exciton and charge carrier dynamics in few-layer WS_2," *Nanoscale*, vol. 8, no. 10, pp. 5428–5434, 2016.

[197] B. Radisavljevic, M. B. Whitwick, and A. Kis, "Integrated circuits and logic operations based on single-layer MoS_2," *ACS Nano*, vol. 5, no. 12, pp. 9934–9938, 2011.

[198] M. Fontana, T. Deppe, A. K. Boyd, M. Rinzan, A. Y. Liu, M. Paranjape, and P. Barbara, "Electron-hole transport and photovoltaic effect in gated MoS_2 Schottky junctions," *Sci. Rep.*, vol. 3, p. 1634, 2013.

[199] A. Pospischil, M. M. Furchi, and T. Mueller, "Solar-energy conversion and light emission in an atomic monolayer p–n diode," *Nat. Nanotechnol.*, vol. 9, no. 4, pp. 257–261, 2014.

[200] B. W. H. Bauger, H. O. H. Churchill, Y. F. Yang, and P. Jarillo-Herrero, "Optoelectronic devices based on electrically tunable p–n diodes in a monolayer dichalcogenide," *Nat. Nanotechnol.*, vol. 9, no. 4, pp. 262–267, 2014.

[201] L. Britnel, R. M. Ribeiro, A. Eckmann, R. Jalil, B. D. Belle, A. Mishchenkom, Y.-J. Kim, R. V. Gorbachev, T. Georgiou, S. V. Morozov, A. N. Grigorenko, A. K. Geim, C. Casiraghi, A. H. C. Neto, and K. S. Novoselov, "Strong light-matter interactions in heterostructures of atomically thin films," *Science*, vol. 340, no. 6138, pp. 1311–1314, 2013.

[202] C.-H. Lee, G.-H. Lee, A. M. van der Zande, W. Chen, Y. Li, M. Han, X. Cui, G. Arefe, C. Nuckolls, T. F. Heinz, J. Guo, and J. H. and Philip Kim, "Atomically thin p–n junctions with van der waals heterointerfaces," *Nat. Nanotechnol.*, vol. 9, no. 9, pp. 676–681, 2014.

[203] X. Hong, J. Kim, S.-F. Shi, Y. Zhang, C. Jin, Y. Sun, S. Tongay, J. Wu, Y. Zhang, and F. Wang, "Ultrafast charge transfer in atomically thin MoS_2/WS_2 heterostructures," *Nat. Nanotechnol.*, vol. 9, no. 9, pp. 682–686, 2014.

[204] R. S. Sundaram, M. Engel, A. Lombardo, R. Krupke, A. C. Ferrari, P. Avouris, and M. Steiner, "Electroluminescence in single layer MoS_2," *Nano Lett.*, vol. 13, no. 4, pp. 1416–1421, 2013.

[205] S. Wu, S. Buckley, J. R. Schaibley, L. Feng, J. Yan, D. G. Mandrus, F. Hatami, W. Yao, J. Vuckovic, A. Majumdar, and X. Xu, "Monolayer semiconductor nanocavity lasers with ultralow thresholds," *Nature*, vol. 520, no. 7545, pp. 69–72, 2015.

[206] W. Zhao, Z. Ghorannevis, L. Chu, M. Toh, C. Kloc, P.-H. Tan, and G. Eda, "Evolution of electronic structure in atomically thin sheets of WS_2 and WSe_2," *ACS Nano*, vol. 7, no. 1, pp. 791–797, 2013.

[207] N. Scheuschner, O. Ochedowski, A. M. Kaulitz, R. Gillen, M. Schleberger, and J. Maultzsch, "Photoluminescence of freestanding single- and few-layer MoS_2," *Phys. Rev. B*, vol. 89, no. 12, p. 125 406, 2014.

[208] A. A. Mitioglu, P. Plochocka, J. N. Jadczak, W. Escoffier, G. L. J. A. Rikken, L. Kulyuk, and D. K. Maude, "Optical manipulation of the exciton charge state in single-layer tungsten disulfide," *Phys. Rev. B*, vol. 88, no. 24, p. 245 403, 2013.

[209] M. Currie, A. T. Hanbicki, G. Kioseoglou, and B. T. Jonker, "Optical control of charged exciton states in tungsten disulfide," *Appl. Phys. Lett.*, vol. 106, no. 20, p. 201 907, 2015.

[210] C. Mai, A. Barrette, Y. Yu, Y. G. Semenov, K. W. Kim, L. Cao, and K. Gundogdu, "Many-body effects in valleytronics: Direct measurement of valley lifetimes in single-layer MoS_2," *Nano Lett.*, vol. 14, no. 1, pp. 202–206, 2014.

[211] D. Vella, V. Vega-Mayoral, C. Gadermaier, N. Vujicic, T. Borzda, P. Topolovsek, M. Prijatelj, I. Tempra, E. A. A. Pogna, and G. Cerullo, "Femtosecond spectroscopy on MoS_2 flakes from liquid exfoliation: Surfactant independent exciton dynamics," *J. Nanophoton.*, vol. 10, no. 1, p. 012 508, 2015.

[212] C. Mai, Y. G. Semenov, A. Barrette, Y. Yu, Z. Jin, L. Cao, K. W. Kim, and K. Gundogdu, "Exciton valley relaxation in a single layer of WS_2 measured by ultrafast spectroscopy," *Phys. Rev. B*, vol. 90, no. 4, p. 041 414, 2014.

[213] J. Cabanillas-Gonzalez, T. Virgili, A. Gambetta, G. Lanzani, T. D. Anthopoulos, and D. M. de Leeuw, "Photoinduced transient stark spectroscopy in organic semiconductors: A method for charge mobility determination in the picosecond regime," *Phys. Rev. Lett.*, vol. 96, no. 10, p. 106 601, 2006.

[214] C. Gadermaier, E. Menna, M. Meneghetti, W. J. Kennedy, Z. V. Vardeny, and G. Lanzani, "Long-lived charged states in single-walled carbon nanotubes," *Nano Lett.*, vol. 6, no. 2, pp. 301–305, 2006.

[215] J. Cabanillas-Gonzalez, G. Grancini, and G. Lanzani, "Pump-probe spectroscopy in organic semiconductors: Monitoring fundamental processes of relevance in optoelectronics," *Adv. Mater.*, vol. 23, no. 46, pp. 5468–5485, 2011.

[216] A. Ramasubramaniam, "Large excitonic effects in monolayers of molybdenum and tungsten dichalcogenides," *Phys. Rev. B*, vol. 86, no. 11, p. 115 409, 2012.

[217] M. Yan, L. J. Rothberg, E. W. Kwock, and T. M. Miller, "Interchain excitations in conjugated polymers," *Phys Rev. Lett.*, vol. 75, no. 10, p. 1992, 1995.

[218] C. Manzoni, A. Gambetta, E. Menna, M. Meneghetti, G. Lanzani, and G. Cerullo, "Intersubband exciton relaxation dynamics in single-walled carbon nanotubes," *Phys. Rev. Lett.*, vol. 94, no. 20, p. 207 401, 2005.

[219] A. Leitenstorfer, C. Furst, A. Laubereau, W. Kaiser, G. Trankle, and G. Weimann, "Femtosecond carrier dynamics in GaAs far from equilibrium," *Phys Rev. Lett.*, vol. 76, no. 9, p. 1545, 1996.

[220] T. Ichibayashi, S. Tanaka, J. Kanasaki, K. Tanimura, and T. Fauster, "Ultrafast relaxation of highly excited hot electrons in Si: Roles of the L-X intervalley scattering," *Phys. Rev. B*, vol. 84, no. 23, p. 235 210, 2011.

[221] B. Radisavljevic and A. Kis, "Mobility engineering and a metal–insulator transition in monolayer MoS_2," *Nat. Mater.*, vol. 12, no. 9, pp. 815–820, 2013.

[222] W. Bao, N. J. Borys, C. Ko, J. Suh, W. Fan, A. Thron, Y. Zhang, A. Buyanin, J. Zhang, S. Cabrini, P. D. Ashby, A. Weber-Bargioni, S. Tongay, S. Aloni, D. F. Ogletree, J. Wu, M. B. Salmeron, and P. J. Schuck, "Visualizing nanoscale excitonic relaxation properties of disordered edges and grain boundaries in monolayer molybdenum disulfide," *Nat. Common.*, vol. 6, p. 7993, 2015.

[223] A. M. van der Zande, P. Y. Huang, D. A. Chenet, T. C. Berkelbach, Y. M. You, G.-H. Lee, T. F. Heinz, D. R. Reichman, D. A. Muller, and J. C. Hone, "Grains and grain boundaries in highly crystalline monolayer molybdenum disulphide," *Nat Mater.*, vol. 12, no. 6, pp. 554–561, 2013.

Bibliography

Publications related to the thesis

All publications related to the thesis are referenced in the text.

Journal articles

V. Vega-Mayoral, C. Backes, D. Hanlon, U. Khan, Z. Gholamvand, M. O'Brien, G. S. Duesberg, C. Gadermaier, and J. N. Coleman, "Photoluminescence from liquid-exfoliated WS_2 monomers in poly(vinyl alcohol) polymer composites," *Adv. Funct. Mater.*, vol. 26, no. 7, pp. 1028–1039, 2016.

V. Vega-Mayoral, D. Vella, T. Borzda, M. Prijatelj, Z. G. Tempra, E. A. A. Pogna, S. D. Conte, P. Topolovsek, N. Vujicic, G. Cerullo, D. Mihailovic, and C. Gadermaier, "Exciton and charge carrier dynamics in few-layer WS_2," *Nanoscale*, vol. 8, no. 10, pp. 5428–5434, 2016.

C. Backes, B. M. Szydlowska, A. Harvey, S. Yuan, V. Vega-Mayoral, B. R. Davies, P.-l. Zhao, D. Hanlon, E. J. G. Santos, M. I. Katsnelson, W. J. Blau, C. Gadermaier, and J. N. Coleman, "Production of highly monolayer enriched dispersions of liquid-exfoliated nanosheets by liquid cascade centrifugation," *ACS Nano*, vol. 10, no. 1, pp. 1589–1601, 2016.

D. Vella, V. Vega-Mayoral, C. Gadermaier, N. Vujicic, T. Borzda, P. Topolovsek, M. Prijatelj, I. Tempra, E. A. A. Pogna, and G. Cerullo, "Femtosecond spectroscopy on MoS_2 flakes from liquid exfoliation: Surfactant independent exciton dynamics," *J. Nanophoton.*, vol. 10, no. 1, p. 012 508, 2015.

L. Klopotowski, C. Backes, A. Mitioglu, V. Vega-Mayoral, D. Hanlon, J. Coleman, V. Ivanov, D. Maude, and P. Plochocka, "Revealing the nature of excitons in liquid exfoliated monolayer tungsten disulphide," *Nanotechnology*, vol. 27, no. 42, p. 425 701, 2016.

Conference contributions

V. Vega-Mayoral, D. Vella, T. Borzda, N. Vujicic, P. Topolovsek, M. Prijatelj, C. Gadermaier, I. Tempra, G. Cerullo, and D. Mihailovic, "Pump-probe WS_2 fundamental properties.," in *V: Flatlands : Beyond graphene*, Dublin, Ireland: poster, 9-11 June 2014.

V. V. Mayoral, D.Vella, T. Borzda, N. Vujicic, P. Topolovsek, M. Prijatelj, C. Gadermaier, and D. Mihailovic, "Pump-probe WS_2 fundamental properties," in *Fourth international workshop o nanocarbon photonics and optoelectronics*, Polviarvi, Finland: poster, 8 July - 1 August 2014.

V. Vega-Mayoral, D. Vella, T. Borzda, M. Prijatelj, I. Tempra, E. A. A. Pogna, S. dal Conte, P. Topolovsek, N. Vujicic, C. B. andJonathan N Coleman, G. Cerullo, D. Mihailovic, and C. Gadermaier, "Relaxation processes of photogenerated charges in MoS_2 and WS_2," in *Flatlands beyond graphene 2016*, Bled, Slovenia: oral contribution, 5-8 July 2015.

E. Vaquedano-Peralvarez, V. Vega-Mayoral, D. Vella, P. A. Postigo, and C. Gadermaier, "Pattering photonic structures by soft lithography in WS_2 PMMA composite," in *Flatlands beyond graphene 2016*, Bled, Slovenia: poster, 5-8 July 2015.

V. Vega-Mayoral, C. Backes, D. Vella, P. Topolovsek, T. Borzda, D. Hanlon, J. N. Coleman, C. Gadermaier, and D. Mihailovic, "Photophysics and applications of transition metal dichalchogenide monolayers fabricated via liquid phase exfoliation," in *Xi. reunión nacional de optica*, Salamanca, Spain, 1-3 September 2015.

V. Vega-Mayoral, C. Backes, D. Hanlon, U. Khan, Z. Gholamvand, M. O'Brien, G. S. Duesberg, C. Gadermaier, and J. N. Coleman, "Photoluminescence from liquid-exfoliated WS_2 monomers in poly(vinyl) alcohol polymer composites," in *XXXth international winterschool euroconference on electronic properties of novel materials (iwepnm)*, Kirchberg in Tirol, Austria: poster, 13-20 February 2016.

V. Vega-Mayoral, D. Vella, T. Borzda, M. Prijatelj, P. Topolovsek, N. Vujicic, D. Mihailovic, and C. Gadermaier, "Exciton and charge carrier dynamics in few-layer WS_2 and dynamics thickness dependence in MoS_2 few-layer selection," in *Nonequilibrium phenomena in complex matter : New observations and new theories.*, Krvavec, Slovenia: oral contribution, 13-16 December 2015.

V. Vega-Mayoral, J. S. R. A. de Lara, and I. J. S. Larran, "Spatially resolved transillumination by optical fiber.," in *Slonano 2013*, Ljubljana, Slovenia: poster, 23-25 October 2013.

Conference contributions not presented by me

T. Borzda, N. Vujicic, C. Gadermaier, P. topolovsek, T. Mertelj, D. Vella, V. Vega-Mayoral, and D. Mihailovic, "Femtosecond charge transfer from MoS_2 to organic acceptor.," in *V: Flatlands : Beyond graphene*, Dublin, Ireland: poster, 9-11 June 2014.

D. Vella, V. Vega-Mayoral, T. Borzda, N. Vujicic, P. topolovsek, M. Prijatelj, C. Gadermaier, I. Tempra, G. Cerullo, and D. Mihailovic, "Femtosecond spectroscopy on MoS_2 films : Effects of synthesis on the electron dynamics," in *V: Flatlands : Beyond graphene*, Dublin, Ireland: poster, 9-11 June 2014.

T. Borzda, N. Vujicic, C. Gadermaier, P. Topolovsek, T. Mertelj, D. Vella, V. Vega-Mayoral, and D. Mihailovic, "Femtosecond charge transfer from MoS_2 to organic acceptor. v," in *Fourth international workshop o nanocarbon photonics and optoelectronics*, Polvijarvi, Finland: poster, 8 July - 1 August 2014.

D. Vella, V. Vega-Mayoral, T. Borzda, N. Vujicic, P. Topolovsek, M. Prijatelj, C. Gadermaier, and D. Mihailovic, "Femtosecond spectroscopy on MoS_2 films: Effects of synthesis on the electron dynamics," in *Fourth international workshop o nanocarbon photonics and optoelectronics*, Polvijarvi, Finland: poster, 8 July - 1 August 2014.

T. Borzda, C. Gadermaier, N. Vujicic, P. Topolovsek, M. Borovsak, T. Mertelj, D. Viola, C. Manzoni, E. A. A. Pogna, D. Brida, M. R. Antognazza, F. Scotognela, G. Lanzani, G. Cerullo, and D. Mihailovic, "Mechanism of charge carriers generation in MoS_2," in *Flatlands beyond graphene 2016*, Bled, Slovenia: oral contribution, 5-8 July 2015.

B. Visic, L. Yadgarov, V. Vega-Mayoral, D. Vella, E. A. A. Pogna, S. dal Conte, G. Cerullo, C. Gadermaier, and R. Tenne, "Optical properties of WS_2 nanotubes," in *Flatlands beyond graphene 2016*, Bled, Slovenia: oral contribution, 5-8 July 2015.

P. Topolovsek, V. Vega-Mayoral, F. Lamberti, C. Gadermaier, and A. Petrozza, "Exfoliated MoS_2 and WS_2 as charge selective layer in perovskite solar cell," in *Flatlands beyond graphene 2016*, Bled, Slovenia: poster, 5-8 July 2015.

L. Klopotowski, C. Backes, A. Mitioglu, V. Vega-Mayoral, J. N. C. andV. Y. Ivanov, D. K. Maude, and P. Plochocka, "Long-lived circular polarization of defect photoluminescenceof liquid exfoliated tungsten disulfide," in *Flatlands beyond graphene 2016*, Bled, Slovenia: poster, 5-8 July 2015.

M. Prijatelj, V. Vega-Mayoral, D. Vella, T. Borzda, C. Gadermaier, and D. Mihailovic, "Ambient intercalation and rapid expansion of MoS_2 crystals," in *Flatlands beyond graphene 2016*, Bled, Slovenia: oral contribution, 5-8 July 2015.

D. Vella, D. Ovchinnikov, N. Martino, V. Vega-Mayoral, D. Dumcenco, Y.-C. Kung, M.-R. antognazza, A. Kis, G. Lanzani, D. Mihailovic, and C. Gadermaier, "Giant unconventional electroabsorption in monolayer MoS_2," in *Flatlands beyond graphene 2016*, Bled, Slovenia: oral contribution, 5-8 July 2015.

T. Borzda, N. Vujicic, C. Gadermaier, P. Topolovsek, T. Mertelj, D. Vella, V. Vega-Mayoral, and D. Mihailovic, "Femtosecond charge transfer from MoS_2 to organic acceptor.," in *5th international conference on photoinduced phase transitions and cooperative phenomena*, Bled, Slovenia: oral contribution, 8-13 June 2014.

D. Vella, V. Vega-Mayoral, T. Borzda, D. Mihailovic, and C. Gadermaier, "Field induced dissociation of excitons in MoS_2 monolayer," in *XXXth international winterschool euroconference on electronic properties of novel materials (iwepnm)*, Kirchberg in Tirol, Austria: poster, 13-20 February 2016.

D. Vella, V. Vega-Mayoral, T. Borzda, D. Mihailovic, and C. Gadermaier, "Field induced dissociation of excitons in MoS_2 monolayer," in *Nonequilibrium phenomena in complex matter : New observations and new theories.*, Krvavec, Slovenia: oral contribution, 13-16 December 2015.

T. Borzda, V. Vega-Mayoral, D. Vella, P. Topolovsek, N. Vujicic, G. Cerullo, D. Mihailovic, and C. Gadermaier, "Photoinduced charge transfer between MoS_2 and organic semiconductors," in *Nonequilibrium phenomena in complex matter : New observations and new theories.*, Krvavec, Slovenia: oral contribution, 13-16 December 2015.

Prizes and awards

Awarded as "best poster contribution" in the 30^{th} edition of *International Winterschool on Electronic properties of Novel Materials* in Kirchberg in Tirol.

Biography

I graduated in July 2012 at *Universidad de Salamanca*, in Salamanca (Spain), with a Bachelor in Science (Physics). During my bachelor studies I obtained a *Fray Luis de León*[1] fellowship to study for one year in *Universidad de Zaragoza*, in Zaragoza (Spain).

Immediately after finishing my bachelor studies I enrolled in the *Master Physics and Technology of Lasers* in *Universidad de Salamanca* and *Universidad de Valladolid*. This same year I obtained a *Beca de colaboración*[2] (collaboration fellowship) from the Spanish government. During my master thesis, carried out under the supervision of Prof. Julio San Roman and Prof. Iñigo Juán Sola Larrañaga, I focused on light-matter interaction processes. That same year I enrolled in the OSA student chapter of Universidad de Salamanca (OSAL)[3]. The main activity of OSAL is "the optics adventure".

I obtained a PhD position in MoWSeS Marie Courie Initial Training Network. I have developed my PhD in the Complex Matter Department of the Jožef Stefan Institute. This thesis has been supervised by Prof. Christoph Gadermaier. During my PhD I have had two secondments, one in Prof. Coleman Group in Trinity College Dublin and a second one in Aixtron in Germany. I will hopefully obtain my PhD inn nanoscience and nanotechnologies in the Jozef Stefan international Postgraduated school.

[1] http://www.educa.jcyl.es/es/resumenbocyl/edu-700-2009-25-3-convocan-subvenciones-dirigidas-universid

[2] http://www.mecd.gob.es/mecd/servicios-al-ciudadano-mecd/catalogo/general/educacion/998142/ficha.html

[3] http://optica.usal.es/osal/osal